From the holdings of the Department of Special Collections , Princeton University Library, Princeton, NJ

These documents are either in the public domain, or can only be used for educational and research purposes (Fair use) as per U.S. Copyright law (text below). By accessing this file, all users agree that their use falls in the public domain or within fair use as defined by the copyrightlaw. We do not charge any permission or usage fees for the publication of images of material inour collections, including those provided by Princeton University Library, via our website, catalog, or directly from staff.For more information regarding copyright, credit, and citation please review the information onthe Copyright, Credit and Citation Guidelines page of our website.
https://library.princeton.edu/special-collections/policies/copyright-credit-and-citation-guidelines. If you have any questions, including how to order higher-quality images from the collection, contact Special Collections Public Services via our Ask Us! Form. https://library.princeton.edu/special-collections/ask-us

---

Doctoral Dissertations, 2011-2026 Atmospheric and Oceanic Sciences

2014

Superrotation and tropical waves in idealized atmospheric models

Potter, Samuel

Princeton, NJ : Princeton University

---

http://arks.princeton.edu/ark:/88435/dsp01ks65hf43h

U.S. Copyright law: The copyright law of the United States (Title 17, §108, United States Code) governs the making of photocopies or other reproductions of copyrighted material. Under certain conditions specified in the law, libraries and archives are authorized to furnish a photocopy or other reproduction. One of these specified conditions is that the photocopy or reproduction is not to be used for any purpose other than private study, scholarship, or research. If a user makes a request for, or later uses, a photocopy or reproduction for purposes in excess of fair use that user may be liable for copyright infringement. This institution reserves the right to refuse to accept a copying order if, in its judgment, fulfillment of the order would involve a violation of copyright law. https://www.copyright.gov/title17/title17.pdf

Superrotation and tropical waves in idealized atmospheric models

Samuel Friedman Potter

A Dissertation
Presented to the Faculty
of Princeton University
in Candidacy for the Degree
of Doctor of Philosophy

Recommended for Acceptance
by the Program in
Atmospheric and Oceanic Sciences
Advisor: Geoffrey K. Vallis

September 2014

© Copyright by Samuel Friedman Potter, 2014.

All rights reserved.

Abstract

This thesis investigates tropical variability in idealized atmospheric general circulation models. We start by exploring the parameter space of a Held-Suarez forced dynamical core to find superrotating atmospheric states. Superrotation, a state of the atmosphere where equatorial winds are westerly, is dependent on eddy momentum fluxes. We vary four fundamental model parameters and find that the thermal Rossby number ($R_o = R\Delta_h/(2\Omega a)^2$) is the primary control of superrotation. At large R_o the atmosphere's tropics become dominated by Kelvin waves that flux momentum equatorward.

Next we study the meridional propagation of extratropical Rossby waves using the linearized barotropic vorticity equation. We find that the WKB approximation is good at approximating Rossby wave propagation but fails to account for significant tunneling of wave energy in evanescent regions. We show that while climatological boreal winter and spring East Pacific winds are mostly transparent to stationary waves, even minor changes in the zonal winds can produce significant reflection.

Using the insight that Rossby waves retain significant wave energy while tunneling through evanescent regions we lay out three necessary conditions for the excitation of equatorial Kelvin waves by extratropical Rossby waves: the matching of wavenumbers and frequencies and a minimizing of evanescence between the storm track and tropical waveguide. We argue that the large R_o atmosphere superrotates because wavenumber one variability is preferred and Rossby wave evanescence is minimized.

We next look at tropical variability in a seasonally varying dynamical core, where strong easterlies, rather than westerlies, dominate the tropics. We show that with sufficient seasonality the tropical easterlies are barotropically unstable and tropical eddies are generated. The eddies are a strong function of time-of-year: Kelvin waves are prevalent near equinoxes but equatorial Rossby and easterly waves dominate near solstices.

Lastly we investigate extreme global warming integrations of a full-physics atmospheric model and find that MJO-like tropical variability and superrotation become preferred at hotter temperatures, along with extreme changes in the model's cloud parameterizations. When the atmosphere strongly superrotates the convective scheme shuts off and the stratiform scheme becomes dominant, which suggests that atmospheric models may not be capable of re-creating hothouse climates.

Acknowledgements

I have a host of people I would like to thank. First I would like to thank my advisor Geoff Vallis for both keeping me on track and providing me with the freedom to pursue questions I found interesting. I would like to thank my committee member Steve Garner for putting up with a sporadic meeting schedule and for helping Thomas Spengler and I with the analytic results in chapter 3. I would also like to thank my committee member, Isaac Held, for always asking tough questions.

There are several organizations I would like to acknowledge. During my work I was supported by award NA08OAR4320752 from the National Oceanic and Atmospheric Administration, U.S. Department of Commerce, the National Science Foundation under Grant AGS-1144302, and the American Meteorological Society Graduate Fellowship sponsored by Raytheon Company.

There are many collaborators, postdoctoral researchers, and students who have been generous with their time. Collaborating with Thomas Spengler on the barotropic reflection work will be one of my favorite memories of graduate school. Working with Jonathan Mitchell has been a fantastic opportunity. The dry atmosphere superrotation chapter would not have happened without many helpful discussions and comments on drafts from Jonathan. Tim Merlis very kindly taught me how to use the suite of moist models that he ported to Gaea, without which Chapter 6 would not have been possible. Amanda O'Rourke has been a great officemate and friend since I started at Princeton, and her willingness to help me understand cospectra has been a huge help. I would like to thank Lucas Harris for helping with the cubed sphere model. Discussions with Tom Flannaghan about equatorial waves and Spencer Hill about clouds were also very helpful.

I would like to thank all the AOS graduate students for the opportunity to spend time with such smart, motivated, and friendly people. I would particularly like to thank my fellow incoming class: He, Claire, and Joe. The administrators, ops staff, and help desk at GFDL

have always been quick to help. The AOS administrative staff has always been friendly and happy to help figure out the latest emergency. In particular I would like to thank Laura Rossi for always making the financial side of things easy to navigate and Anna Valerio, without whom the AOS grad student world would stop spinning.

Lastly I would like to thank my mom, dad, sister, and Caitlin. I would not have made it this far without your unconditional support.

Contents

Abstract iii

Acknowledgements v

List of Tables xi

List of Figures xii

1 Introduction **1**

2 Spontaneous superrotation and the role of Kelvin waves in an idealized dry GCM **8**

2.1 Introduction 8

2.2 Methods 11

2.2.1 Model description 11

2.2.2 Spectral analyses 14

2.3 Description of parameter end members 14

2.3.1 Control atmosphere 16

2.3.2 Large thermal Rossby number 16

2.3.3 Small thermal Rossby number 17

2.3.4 Nondimensional radiative timescale 18

2.3.5 Ekman number 20

2.3.6 Nondimensional vertical temperature gradient 21

2.4 Superrotation parameter regime 23

2.5 Spectral characteristics of the intermediate thermal Rossby number modes . 27
2.5.1 Wavenumber-frequency filtering 34
2.6 Meridional Kelvin wave momentum transport in other contexts 37
2.6.1 Kelvin waves in Williams (2003) 37
2.6.2 Momentum flux divergence on Earth 37
2.7 Sensitivity of the superrotating state to horizontal resolution, vertical resolution, and an upper atmosphere sponge 39
2.8 Discussion and Conclusions 41

3 Reflection of barotropic Rossby waves in sheared flow and validity of the WKB approximation 45
3.1 Introduction 45
3.2 Meridional Wave Propagation 46
3.3 Methods 49
3.4 The tanh profile 51
3.5 The squared hyperbolic secant profile 57
3.6 An application to the East Pacific window region 59
3.7 Conclusions 63

4 Some sufficient conditions for dynamically active equatorial modes 66
4.1 Tropical and extratropical variability in spectral space 66
4.2 Spectral characteristics of the dynamical core 69
4.3 An approximate dispersion relation for the extratropical Rossby wave signal 70
4.3.1 Nondimensional equation 75
4.3.2 Frequency matching 75
4.4 Equatorial waves in the superrotating a = 9e5 m and Williams 2003 atmospheres 78
4.5 A wave evanescence argument 81

4.5.1 Equatorial deformation radius 83
4.5.2 Determination of critical latitude 83
4.5.3 A crude description of evanescence between the Rossby wave breaking latitude and the tropical waveguide 84
4.5.4 Why the small radius and Williams 2003 atmospheres are prone to superrotation. 85
4.6 Conclusion 86

5 The momentum balance and equatorial waves of a seasonally varying dry dynamical core 88

5.1 Introduction 88
5.2 Methods 90
5.2.1 Model forcing 90
5.3 Results 91
5.3.1 Climatologies 91
5.3.2 Momentum budgets 92
5.3.3 Time dependency of acceleration terms 94
5.3.4 Solstitial atmosphere 96
5.4 Spectral diagnostics of seasonal atmospheres 98
5.5 The equatorial temperature minimum and equatorial waves 101
5.6 Seasonal instability 107
5.7 Conclusions 109

6 Superrotation and tropical variability in a full-physics AGCM 110

6.1 Introduction 110
6.2 Model description 111
6.3 Control run 112

6.3.1 Spectral diagnostics 113
6.4 Seasonal atmospheres 114
6.5 Small radius superrotation in a moist atmosphere 118
6.6 The transition to a hot, superrotating atmosphere 122
6.6.1 Hothouse tropical variability 126
6.6.2 Changes in model physics 129
6.7 Discussion and conclusions 133

7 Conclusion **136**

Bibliography **141**

List of Tables

2.1 Key dimensional and nondimensional parameters of the standard Held–Suarez forced dynamical core. 13

2.2 List of parameter values for all experiments. Each paired set of rows first displays the nondimensional parameter that was changed with the corresponding dimensional parameter value below. 15

List of Figures

2.1 Control atmosphere climatology 17

2.2 $R_o = 10$ (small radius) atmosphere climatology 18

2.3 $R_o = 0.001$ (large radius) atmosphere climatology 19

2.4 $\tau = 0.063$ (strong Newtonian cooling) atmosphere climatology 20

2.5 $\tau = 12600$ (weak Newtonian cooling) atmosphere climatology 21

2.6 $E = 7.9$ (strong friction) atmosphere climatology 22

2.7 $E = 4.0e - 4$ (weak friction) atmosphere climatology 23

2.8 $\mu = 0.0017$ (weak stratification) atmosphere climatology 24

2.9 $\mu = 1.7$ (strong stratification) atmosphere climatology 25

2.10 Equatorial zonal winds as function of nondimensional parameters 26

2.11 $R_o = 1$ atmosphere climatology 28

2.12 Control atmosphere spectral diagnostics 29

2.13 CLAUS dataset and NCEP II Reanalysis spectral diagnostics 31

2.14 $R_o = 1$ atmosphere spectral diagnostics 32

2.15 $R_o = 1$ atmosphere phase speed eddy cospectra 34

2.16 $R_o = 0.1$ and $R_o = 0.55$ spectral diagnostics 35

2.17 $R_o = 1$ atmosphere wavenumber-frequency filtered variability 36

2.18 Williams 2003 zonal winds and spectral diagnostics 38

2.19 $R_o = 1$ T85 climatology 39

2.20 $R_o = 1$ 60 level climatology 40

2.21 $R_o = 1$ sponge climatology 41
2.22 Eddy diagnostics for higher resolution and sponge atmospheres 42

3.1 Schematic for the 'no reflection' proof of the WKB approximation 50
3.2 Reflection coefficients for the tanh profile 53
3.3 Reflection in the jump profile 55
3.4 Base ten logarithm of the profile maximum of ϕ in the tanh profile with $c = -0.9$ 56
3.5 Percent relative error for the WKB approximated transmission coefficient in the tanh profile with $c = -0.9$ 56
3.6 Absolute error for the single scatter approximated reflection coefficient in the tanh profile with $c = -0.9$ 57
3.7 Contours of $|R|$ solved for numerically with the sech^2 profile 58
3.8 Absolute error for the WKB approximated transmission coefficient in the tanh profile with $c = -0.9$ 59
3.9 Base ten logarithm of the profile maximum of ϕ in the sech^2 profile with $c = -0.9$ 60
3.10 Percent relative error for the WKB approximated transmission coefficient in the sech^2 profile with $c = -0.9$ 60
3.11 MAM dimensional and non-dimensional $\bar{u}_{\text{EPW}}$ and MAM 300 mb ERA-interim $\bar{u}$ 62
3.12 $|R|$ in the idealized EPW as a function of minimum nondimensional westerlies 63

4.1 Spectral power of the geopotential height field for the control atmosphere . . 70
4.2 Base ten logarithm of the spectral power of the geopotential height field for the $a = 9e5$ m atmosphere 73
4.3 Base ten logarithm of the spectral power of the geopotential height field for the $a = 1.2e7$ m atmosphere 74
4.4 $\mathcal{S}$ in $\omega - k^*$ space for the control atmosphere 75
4.5 Matching wavenumber and frequency as functions of R_o and Fr 77
4.6 Matching wavenumber and frequency as functions of R_o and ϕ 78

4.7 Climatological fields for the $\cos^{32}\phi$ atmosphere 79
4.8 Base ten logarithm of the spectral power of the geopotential height field for the $\cos^{32}\phi$ atmosphere 80
4.9 $\mathcal{S}$ in $\omega - k$ space at the equator for the $a = 9e5$ m and $\cos^{32}\phi$ atmospheres . 81
4.10 Outline of the evanescence argument 82

5.1 Time mean fields for the 0° $\phi_{\max}$ control atmosphere 92
5.2 Time mean fields for the 23.5° $\phi_{\max}$ atmosphere 93
5.3 Zonal momentum budget for 0° $\phi_{\max}$ control atmosphere 94
5.4 Zonal momentum budget for 23.5° $\phi_{\max}$ atmosphere 95
5.5 Seasonal cycle of vertically averaged $\mathcal{S}$ in the 23.5° $\phi_{\max}$ atmosphere 96
5.6 Seasonal cycle of maximum $\mathcal{S}$ in the 23.5° $\phi_{\max}$ atmosphere 97
5.7 Seasonal cycle of momentum budget terms in the 23.5° $\phi_{\max}$ atmosphere . . 98
5.8 Time mean fields for the 23.5° $\phi_{\max}$ atmosphere fixed at Northern Hemisphere solstice forcing 99
5.9 Zonal momentum budget for 23.5° $\phi_{\max}$ atmosphere fixed at Northern Hemisphere solstice forcing 100
5.10 $\mathcal{S}$ in $\omega - k$ space at the equator and 260 mb in the control permanent equinox atmosphere 101
5.11 $\mathcal{S}$ in $\omega - k$ space at the equator for the 23.5° $\phi_{\max}$ atmosphere both seasonally varying and fixed at days 25, 60, and 90 102
5.12 Equatorial zonal wind at the equator for the 23.5° $\phi_{\max}$ atmosphere both seasonally varying and fixed at days 25, 60, and 90 103
5.13 Difference in climatological temperatures between the 23.5° $\phi_{\max}$ and the control equinox atmospheres 104
5.14 $\overline{\omega}\left(\partial\overline{T}/\partial p - \kappa\overline{T}/p\right)$ for the permanent equinox control and 23.5° $\phi_{\max}$ atmospheres. 104

5.15 $(a\cos\phi)^{-1}\partial/\partial\phi(\overline{v'T'}\cos\phi)$ in the permanent solstice atmosphere 105
5.16 Meridional eddy temperature flux divergence decomposed into wavenumber-frequency space at -1.3° for the 23.5° $\phi_{\max}$ atmosphere both seasonally varying and fixed at days 25, 60, and 90 106
5.17 Annual mean gradient of quasi-geostrophic potential vorticity in the permanent equinox control and the 23.5° $\phi_{\max}$ atmospheres 107
5.18 Seasonality of zonal mean zonal wind and gradient of quasi-geostrophic potential vorticity in the 23.5° $\phi_{\max}$ atmosphere 108

6.1 Time mean fields for the control $S_0 = 1400$ W/m^2 aquaplanet atmosphere . . 113
6.2 Spectral diagnostics in the control $S_0 = 1400$ atmosphere 115
6.3 Time mean fields for the 18° obliquity atmosphere 116
6.4 Seasonal cycle of momentum budget terms in the 18° obliquity atmosphere . 117
6.5 $\mathcal{S}$ in $\omega - k$ space for atmospheres with varying obliquities 118
6.6 Time mean fields for the $a = 9e5$ m atmosphere 119
6.7 $\mathcal{S}$ for the $a = 9e5$ m atmosphere 120
6.8 $\mathcal{S}$ cospectra for the $a = 9e5$ m atmosphere 121
6.9 Wavenumber-1 filtered equatorial 141 mb zonal wind variability regressed onto global fields at 141 mb. 122
6.10 Temperature, zonal wind, and eddy fields in the parameter sweep of varying solar constant 123
6.11 Total, convective, and stratiform precipitation in the deep tropics as a function of solar constant 124
6.12 Time mean fields for the $S_0 = 1550$ W/m^2 aquaplanet atmosphere 125
6.13 Time mean fields for the $S_0 = 1600$ W/m^2 aquaplanet atmosphere 126
6.14 Relative humidity in the $S_0 = 1400$ W/m^2 and $S_0 = 1600$ W/m^2 atmospheres. 127

6.15 Equatorial wavenumber-1 variability regressed onto global fields for the $S_0 =$ 1600 W/m^2 atmosphere at 44 mb 128
6.16 $\mathcal{S}$ for several hot atmospheres 129
6.17 Vertical profiles of equatorial convective mass flux 130
6.18 Vertical profiles of equatorial heating by the the model cloud schemes 132
6.19 Vertical profiles of equatorial moistening by the model cloud schemes 132

Chapter 1

Introduction

In a pair of idealized modeling studies Suarez and Duffy (1992) and Saravanan (1993) (from here on SD92 and S93, respectively) showed that Earth-like dynamical cores, when forced by a sufficiently strong tropical stationary wave heating, had a tendency to superrotate. Superrotation is a state of the atmosphere where zonal mean time mean westerlies lie over the equator. Hide's theorem states that superrotation must be maintained by upgradient eddy momentum fluxes (which are created by the stationary wave forcing in SD92 and S93) and that the mean flow cannot create superrotation. The Earth-like superrotation results were interesting because Earth has zonal mean easterlies overlying the equator throughout the year and superrotation is only seen in planetary atmospheres such as Jupiter, Saturn, Venus, and Titan (Saturn's largest satellite). SD92 and S93's results suggested that Earth's atmosphere may have superrotated during the Eocene or Cretaceous when Earth was much warmer, or that it could superrotate in the future when anthropogenic global warming is sufficiently strong.

There were two clues in SD92 and S93 that hinted at an understanding of superrotation in Earth-like atmospheres. First, SD92 showed that a wavenumber-2 tropical heating of magnitude $Q_0 = 1, 2, 3$ K/day had equatorial zonal winds (weak easterlies) indistinguishable from the unforced model. For $Q_0 \geq 4$ the atmosphere changed entirely and strong wester-

lies on the order of 30 m/s lay above the equator. Second, S93 showed that the strongly superrotating atmosphere would *continue* to superrotate for $\sim$ 2000 days after the stationary wave forcing was turned off. Both of these results suggested that superrotation is an alternative steady state of Earth's atmospheric general circulation: perhaps the only thing that separates an atmosphere with equatorial easterlies from a superrotating atmosphere is a sufficient equatorial momentum push.

Building off of their results, Held (1999) (here on H99) offered an explanation of SD92 and S93's results. H99's explanation revolved around extratropical Rossby waves' contributions to the atmosphere's zonal momentum budget. The life cycle of a baroclinic Rossby wave in the latitude-pressure plane starts at the midlatitude surface where strong meridional temperature gradients lead to baroclinic instability which creates Rossby waves (e.g. Edmon et al., 1980). Moving from the surface the wave propagates upwards until, in the upper troposphere, it turns equatorward (Held, 2000, provides a summary of the importance of Rossby waves to the upper troposphere's momentum balance). Note that a Rossby wave in the midlatitudes can propagate either polewards or equatorwards, but equatorward propagation is preferred since the refractive index (mainly governed by the meridional gradient of the Coriolis force, β) is larger nearer the equator (e.g. Hoskins and Ambrizzi, 1993). The Rossby wave propagates equatorward until it reaches its critical latitude, the latitude where the zonal mean zonal wind $\bar{u}$ is equal to the wave's phase speed and nonlinear processes dominate. At their critical latitudes Rossby waves break and deposit pseudomomentum which decelerates (provides an westward tendency to) the mean flow. Conversely, on exiting a region Rossby waves accelerate (provide an eastward tendency to) the mean flow. The upper atmosphere impact of the Rossby wave is to (1) accelerate the midlatitude jets and (2) decelerate the subtropics, where Rossby waves meet their critical latitudes.

H99 speculated that Rossby wave breaking is crucial to not only the subtropical momentum balance but the maintenance of deep tropical winds. If some Rossby waves have

their critical latitude in the deep tropics or even the equator their subsequent breaking and westward acceleration may explain the tendency for Earth's atmosphere to not superrotate. Therefore if a wavelike heating is applied to the deep tropics that gives the atmosphere a push towards tropical westerlies the subtropical critical latitudes may disappear entirely. Tropical Rossby wave breaking will no longer occur since extratropical Rossby waves are able to propagate across the equator.

The later studies of Kraucunas and Hartmann (2005) (here on KH05) and Lee (1999) (here on L99) made a reinterpretation of SD92 and S93 necessary. Both SD92 and S93 used 2-layer primitive equation models with idealized physics. KH05 attempted, and failed, to replicate SD92 and S93's results in a 20 layer primitive equation model. KH05 found that the model with better vertical resolution did not suddenly jump to a superrotating state when the stationary wave forcing magnitude Q_0 was increased past a critical threshold, but found that equatorial winds slowly became more westerly as Q_0 was increased. KH05 also found that there was no hysteresis — the superrotation disappeared only days after the stationary wave forcing was removed. One of the primary takeaways of KH05 was that the dramatic results of SD92 and S93 were almost entirely the result of the truncated vertical resolution and that while a tropical stationary wave forcing did lead to superrotation, it did so in a gradual fashion.

By decomposing the tropical momentum balance term-by-term, L99 was able to show that the seasonally varying Hadley cell — not breaking Rossby waves — is primarily responsible for Earth's equatorial easterlies. L99 showed that the deceleration by Rossby waves gets within 15-20° degrees of the equator, but has no large impact on the deep tropics. Instead, the author showed that near the equator the primary momentum balance was between deceleration caused by the cross-equatorial flow of the seasonally varying Hadley cell and acceleration due to stationary waves and transient waves (mainly the Madden-Julian oscillation). In a second part of their paper KH05 affirmed L99's results by using their model

to show that a permanent solstice atmosphere did not superrotate even when forced with a stationary wave that causes superrotation in the permanent equinox model.

The primary conclusions of the five studies discussed above are that (1) superrotation is a result of tropical wave momentum fluxes near the equator, not a direct result of eddy behavior in the extratropics and (2) Earth does not superrotate because the seasonal Hadley cell decelerates zonal winds in the deep tropics, not because extratropical Rossby waves break there. In models with forced tropical stationary wave forcing the cause of the superrotation is the forced wave itself. Showman and Polvani (2011) argued that the tropical stationary wave momentum fluxes are the result of a particular phasing between the stationary Kelvin and equatorial Rossby waves of the Gill response. Alternatively, Liu and Schneider (2011) argued that the upper atmosphere divergence caused by convective heating (or in an idealized dry model, added diabatic heating) in turn generates Rossby waves that propagate away from the equator and consequently accelerate equatorial zonal winds, very similar to the discussion of midlatitude Rossby waves above. It is clear, however, from the results of KH05, that a sufficiently strong tropical stationary wave will induce superrotation in the absence of a strong seasonal Hadley cell.

A more complex question is: how does an atmospheric model *spontaneously* superrotate? We define spontaneous superrotation as superrotation that exists without explicit zonally asymmetric forcing (like the wavenumber-2 heating in SD92 and S93). Williams (2003) showed that a non-superrotating dry dynamical core with idealized physics can be made to spontaneously superrotate if its Newtonian cooling profile is made to vary as $\cos^n \phi$ rather than $\cos^2 \phi$ as it does in the Earth-like control. When n is made sufficiently large the storm tracks collapse equatorwards and the atmosphere beings to superrotate. The author argued that the superrotation was driven by a barotropic instability on the equatorward side of the hemisphere jets. As n was increased the jets moved closer to the equator and the zonal

wind profile sharpened to the point where, Williams (2003) argued, the zonal wind became barotropically unstable and created eddies that fluxed momentum equatorwards.

A second example of dry dynamical superrotation is found in Mitchell and Vallis (2010). The authors induced superrotation in a dry dynamical core by modifying the thermal Rossby number $R_o = R\Delta_h/(2\Omega a)^2$. Here R is the ideal gas constant, Δ_h is the equator-to-pole temperature gradient in the Newtonian cooling profile, Ω is the planetary rotation rate and a is the planetary radius. Mitchell and Vallis (2010) showed that as the model's R_o was made to be larger (the radius made to be smaller) the atmosphere tended towards strong superrotation. The authors showed that the superrotation was the result of a global wavenumber-1 mode that dominated the bulk of the atmospheric variability. It was argued that the global mode was the result of a barotropic instability that existed mainly during the atmosphere's spinup and that when the global mode had fluxed sufficient momentum to the equator to induce strong superrotation it effectively shut itself off. After spinup the mode returned sporadically only when the superrotating winds weakened sufficiently.

In this thesis we will take a different approach to understanding dry dynamical core superrotation by attempting to better understand the tropical eddy dynamics of superrotating atmospheres. Our argument is different than that of H99, where it was argued that extratropical eddy dynamics are the key to superrotation. Instead we note that, following from Hide's theorem, a spontaneously superrotating atmosphere *must* have eddies fluxing momentum to the equator, and understanding these tropical eddies is the key component to understanding superrotation.

Some of the tools of tropical dynamics are applicable to dry atmosphere models. Wheeler and Kiladis (1999) used Fourier transforms of outgoing longwave radiation (OLR) to show that much of Earth's tropical intraseasonal variability neatly fits into the dispersion relations first written down by Matsuno (1966) for waves on the shallow water equatorial β-plane. The use of a cloud or convection field is not necessary and, e.g., Hendon and Wheeler (2008)

showed that dynamical fields like zonal wind and geopotential height can also be used to identify tropical waves.

While convection is an integral part of intraseasonal tropical variability, there are hints that dry atmospheric models have the right ingredients for significant tropical eddy dynamics. Using reanalysis and satellite derived OLR, Liebmann and Hartmann (1984) showed that on intraseasonal timescales tropical variability was strongly correlated with extratropical variability that occurred several days before. Using reanalysis Straub and Kiladis (2003a) showed that Pacific Kelvin wave activity in boreal summer was directly triggered by extratropical Rossby wave trains propagating into the deep tropics. Lastly, Lin et al. (2000) used a model where baroclinic instability could effectively be turned off to show that intraseasonal tropical variability essentially vanishes in an atmosphereric model with no extratropical variability. We highlight these studies because they suggest that a key trigger of intraseasonal tropical variability is extratropical variability, not convection. While dry dynamical cores do not include moist convection they do have robust extratropical variability and, consequently, the potential for significant tropical variability.

In this thesis we attempt to better understand superrotation, tropical variability, and tropical-extratropical interaction in simplified models. By studying superrotation we are, through Hide's theorem, studying tropical eddies and waves, and a major focus of this thesis is understanding how and why a non-superrotating atmosphere can be made to be superrotating. We additionally investigate atmospheres that have significant tropical variability and strong equatorial easterlies and use a highly idealized model to study how Rossby waves retain their wave energy as they propagation meridionally into the tropics. The remainder of the thesis is organized as follows.

In Chapter 2 we explore the parameter space of a Held-Suarez forced dry dynamical core to find superrotating atmospheric states by varying four fundamental parameters of the dynamical core, the thermal Rossby number ($R_o = R\Delta_h/(2\Omega a)^2$), the Ekman number

($E = r/(2\Omega)$), the nondimensional radiative timescale ($\tau = 2\Omega\tau_r$), and the nondimensional vertical temperature gradient ($\mu = \Delta_v/\Delta_h$). We then identify the tropical waves that play a key role in generating dry dynamical core superrotation.

In Chapter 3 we study the meridional propagation of extratropical Rossby waves using the linearized barotropic vorticity equation and investigate the accuracy of the WKB approximation in a variety of idealized wind profiles. We use our model to explore reflection and transmission of extratropical Rossby waves through the East Pacific window to investigate the likelihood of barotropic Rossby waves passing through the window region.

In Chapter 4 we attempt to explain the large R_o superrotation explored in Chapter 2 by laying out three necessary conditions for the excitation of equatorial Kelvin waves by extratropical Rossby waves: the matching of wavenumbers, the matching of frequencies, and a minimizing of evanescence between the region of Rossby wave generation and the tropical waveguide.

Chapter 5 looks at tropical variability in a seasonally varying version of the dry dynamical core. We show that while extremely seasonal atmospheres do not superrotate, they do have significant tropical variability. The equatorial waves generated by the extreme seasonality play a key role in the general circulation by transporting heat and momentum equatorwards.

Lastly, in Chapter 6 we turn away from simplified dry models and investigate tropical variability in extreme global warming integrations of a full-physics aquaplanet atmospheric general circulation model. Similar to previous studies we find that very hot atmospheres have a tendency to superrotate, but unlike previous studies we show that this superrotation may be an artifact of model physics.

Chapter 2

Spontaneous superrotation and the role of Kelvin waves in an idealized dry GCM

This chapter is a reproduction of Potter et al. (2014).

2.1 Introduction

An atmosphere is superrotating if at some location the winds have greater angular momentum than that of the planet at the equator, Ωa^2, where Ω is the rotation rate and a is the planetary radius. This condition becomes harder to satisfy farther poleward as the lower bound for superrotating winds, $u_s = \Omega a \sin^2 \phi / \cos \phi$ where ϕ is latitude, increases rapidly with latitude. Furthermore, if an atmosphere is superrotating in mid-latitudes, but not at the equator, then it will normally be inertially or centrifugally unstable. Thus, superrotation usually implies equatorial superrotation. Although the Earth's troposphere is not, on average, superrotating, at times it may be, and there has long been interest in understanding superrotation in Earth-like atmospheric models (e.g., Suarez and Duffy, 1992; Saravanan, 1993). Titan, the sixth

moon of Saturn, has a terrestrial atmosphere (i.e., an atmosphere with a distinct, often rocky lower boundary) that superrotates, as does Venus and the the gas giants Jupiter and Saturn. Superrotation has also been seen in exoplanet modeling studies for both terrestrial exoplanets (e.g. Joshi et al., 1997; Merlis and Schneider, 2010) and gas giant exoplanets (e.g. Showman et al., 2009; Heng et al., 2011; Rauscher and Menou, 2012).

By Hide's theorem (Hide, 1969) — essentially an application of the general result that there can be no internal extremum of a Lagrangian-conserved quantity if that quantity is diffused (Vallis, 2006) — superrotation in the time mean must be maintained by eddy momentum fluxes. Explicit wave forcing at the equator may give rise to superrotation, as in the primitive-equation experiments of Suarez and Duffy (1992), Saravanan (1993), and Kraucunas and Hartmann (2005), in which the waves were generated by a zonally asymmetric tropical heating. Arnold et al. (2012) also found superrotation in a dynamical core forced with a moving tropical diabatic heating, and identified an equatorial Rossby wave resonance as being responsible for eddy momentum flux convergence at the equator. Wave forcing also gave rise to superrotation in the one-and-a-half-layer shallow water model of (Showman and Polvani, 2010).

In the studies cited above the cause of the superrotation — wave forcing at the equator — is made explicit. There have been fewer studies of the mechanism of *spontaneous* superrotation in Earth-like models, in which equatorial westerlies exist in the time mean in the absence of zonally asymmetric forcing. If there were a source of Rossby waves at the equator then a superrotating state might be expected to emerge, since if the Rossby waves were able to propagate away momentum would converge on the source of the Rossby waves and, if strong enough, generate an eastward flow. In mid-latitudes baroclinic instability is such a source and at the equator convective activity is a potential source, but the circumstances under which convection can generate sufficiently strong Rossby waves, and whether such Rossby waves can propagate sufficiently far from the equator before breaking, are not well

known. Saravanan (1993) did find that superrotation persists even after the tropical forcing was turned off as a consequence of a westerly torque produced by eddying activity at the equator, although the nature and robustness of the eddies giving rise to the superrotation was not explicitly identified — indeed Kraucunas and Hartmann (2005) suggested that the mechanism suggested by Saravanan does not apply in multi-level models. More recent works suggest that thinking of an equatorial westerly jet in the same way as a midlatitude Rossby wave driven jet may be incorrect. Showman and Polvani (2011) showed that momentum fluxes arising from a stationary equatorial forcing are the result of equatorial shallow water waves, not meridionally propagating Rossby waves. Specifically, the equatorial Rossby wave-Kelvin wave structure of the Gill response to a heating generates equatorward momentum fluxes that are likely the cause of superrotation seen in models with stationary wave-like equatorial heating, e.g. Suarez and Duffy (1992), Saravanan (1993), and Kraucunas and Hartmann (2005). Other studies have found that equatorial Rossby waves (e.g. Liu and Schneider, 2011; Arnold et al., 2012) or Kelvin waves (e.g. Iga and Matsuda, 2005) play a crucial role in the generation of superrotation. In this study we aim partly to demonstrate the need for thinking of equatorial westerly jet dynamics as distinct from the dynamics of eddy driven midlatitude jets.

Williams (2003) induced spontaneous superrotation in a dynamical core by changing both the functional form of the radiative cooling profile and the planetary rotation rate. The author increased the exponent of the latitudinal dependence of the thermal forcing from $\cos^2$ to $\cos^n$, $n = 4, 8, 16, 32, 64$ and found that superrotation was the preferred state in the lower rotation, higher n parameter regime. It was hypothesized that the superrotation was the result of barotropic instability on the equatorward side of the subtropical jets.

Mitchell and Vallis (2010) (henceforth MV10) found that superrotation robustly exists in models of terrestrial atmospheres with large thermal Rossby number. In their study the thermal Rossby number was varied via the planetary radius and it was found that a planet

with a smaller radius is more likely to superrotate. They found that the circulation of the large thermal Rossby number atmosphere was dominated by a global wavenumber-1 mode that drove the superrotation, but they were unable to reach a definitive conclusion as to what drove the superrotation. Although barotropic instability seemed to play a role it is unlikely that this is the entire story since barotropic Rossby waves converge momentum into their source region and draw momentum out of the region where they break.

While studying hothouse climates with a full-physics AGCM coupled to a slab ocean, Caballero and Huber (2010) found that as CO_2 was increased in their model the eddy flux of momentum into the tropics grew until the atmosphere began to superrotate. The presence of a hydrological cycle and convection scheme were key in their results, and the mode driving superrotation strongly resembled the Madden–Julian Oscillation. The importance of the MJO to the momentum balance of the tropics was also shown by Lee (1999), who demonstrated that all that was required to make an AGCM superrotate was to turn off the seasonal cycle. In permanent equinox the model weakly superrotated and eddy fluxes into the tropics were dominated by the MJO.

With all of the above studies in mind, our paper has two goals. The first is to extend the results of MV10 to explore further the nondimensional parameter space of a dry dynamical core with the goal of finding what parameters are most important for the momentum balance of the equatorial troposphere. The second is an attempt to identify the modes of variability that drive superrotation in a dry model. We begin with a brief overview of the model in Section 2.2, describe the simulations in Sections 2.3 and 2.4, analyze the results in Section 2.5, briefly discuss similar spectral results in other contexts in Section 2.6, investigate the dependence of our results on model configuration in Section 2.7, and conclude in Section 2.8.

2.2 Methods

2.2.1 Model description

We use the spectral dynamical core from the Geophysical Fluid Dynamics Laboratory Flexible Modeling System (FMS). The FMS dry dynamical core is forced with 'Held–Suarez' idealized physics (Held and Suarez, 1994). All of the runs use T42 spectral resolution with 20 equally spaced sigma levels and a fourth order hyperdiffusion. We begin by nondimensionalizing the primitive equations to find the dynamical core's controlling parameters. The primitive equation nondimensional parameters are found in the zonal momentum and thermodynamic equations:

$$\frac{\partial u}{\partial t} + (\mathbf{v}\cdot\nabla)u + \omega\frac{\partial u}{\partial p} = fv + \frac{uv\tan\phi}{a} - \frac{1}{a\cos\phi}\frac{\partial\Phi}{\partial\lambda} - ru \tag{2.1}$$

$$\frac{\partial \theta}{\partial t} + (\mathbf{v}\cdot\nabla)\theta + \omega\frac{\partial \theta}{\partial p} = -\frac{\theta-\theta^*}{\tau_r} \tag{2.2}$$

In the above equations $(\mathbf{v}\cdot\nabla) = (u/a\cos\phi)\partial/\partial\lambda + (v/a)\partial/\partial\phi$ is the horizontal advective component of the total derivative where a is the planetary radius, p is pressure, λ is longitude and ϕ is latitude. The final term in the zonal momentum equation is Rayleigh drag, with timescale $1/r$. Likewise the final term in the thermodynamic equation is a Newtonian cooling with the permanent equinox Held–Suarez relaxation profile, θ^*, in potential temperature, θ, with cooling timescale, τ_r:

$$\theta^*(\phi,p) = \max[200\,(p_o/p)^{\kappa}\,, (\theta_0 - \Delta_h\sin^2\phi - \Delta_v\log\left(\frac{p}{p_0}\right)\cos^2\phi)] \tag{2.3}$$

where p_0 is the surface pressure, $\kappa = g/c_p$, Δ_h is the equator-to-pole temperature forcing gradient and Δ_v is surface to top of atmosphere temperature forcing gradient. The hydrostatic and continuity equations and the ideal gas equation of state complete the set.

The equations are nondimensionalized by scaling length with a, time by $1/(2\Omega)$, and geopotential height by $\Omega a U$. All potential temperatures except the one appearing in the vertical advection term are scaled by Δ_h. The potential temperature that appears in the $\omega\partial\theta/\partial p$ term in (2.2) is scaled with Δ_v to reflect the difference in vertical and horizontal temperature scales. The horizontal wind scale $U \sim R\Delta_h/(2\Omega a)$ is derived from thermal wind balance, where R is the dry specific gas constant and the pressure velocity ω is scaled using mass continuity, giving $\omega \sim U\delta p/a$. While thermal wind is not a good approximation for large Rossby numbers it is still useful as a control parameter. δp is a scale height in pressure coordinates.

With these scales equations (2.1) and (2.2) become

$$\frac{\partial u}{\partial t} + R_o\left[(\mathbf{v}\cdot\nabla)u + \omega\frac{\partial u}{\partial p}\right] = \hat{f}v + R_o uv\tan\phi - 1/(2\cos\phi)\partial\Phi/\partial\lambda - Eu \tag{2.4}$$

$$\frac{\partial \theta}{\partial t} + R_o\left[(\mathbf{v}\cdot\nabla)\theta + \mu\omega\frac{\partial \theta}{\partial p}\right] = -(\theta - \theta^*)/\tau \tag{2.5}$$

All terms are now nondimensional, with $\hat{f} = \sin\phi$ a nondimensional Coriolis parameter. $R_o = (R\Delta_h)/(2\Omega a)^2$ is the thermal Rossby number, $E = r/(2\Omega)$ is the Ekman number, $\tau = 2\Omega\tau_r$ is a nondimensional radiative timescale, and $\mu = \Delta_v/\Delta_h$ is the ratio of vertical to horizontal temperature forcing gradients in the Held–Suarez forcing profile. Note that the $200 - K$ definition of the Held–Suarez stratosphere means that changing Δ_v will change both the stratification and the tropopause height. The value of the relevant constants and nondimensional parameters for the Earth-control Held–Suarez forced dynamical core can be found in Table 2.1.

In this paper we discuss model integrations where each nondimensional parameter has been varied separately (for example in the thermal Rossby number runs the thermal Rossby number R_o is changed while E, τ, and μ are held fixed). As the code itself has dimensional parameters, the Rossby number is changed through the planetary radius, the Ekman number

$\mathbf{a}$	$\mathbf{\Omega}$	$\mathbf{R}$	$\mathbf{\Delta_h}$	$\mathbf{\Delta_v}$	$\mathbf{r}$
6.371×10^6 m	$7.292 \times 10^{-5} s^{-1}$	287 J K^{-1} kg^{-1}	60 K	10 K	1 days^{-1}
$\tau_\mathbf{r}$	$\mathbf{R_o}$	$\mathbf{E}$	τ	μ	
40 days^{-1}	0.02	0.079	504	0.17	

Table 2.1: Key dimensional and nondimensional parameters of the standard Held–Suarez forced dynamical core.

is changed through the drag timescale, the nondimensional radiative timescale is changed via the radiative timescale, and the ratio of vertical to horizontal temperature gradients is changed through the vertical temperature gradient. A list of experiments is shown in Table 2.2.

2.2.2 Spectral analyses

We use two different spectral methods to analyze tropical variability in our model results. First, we decompose the tropical geopotential height field in spectral space following closely Wheeler and Kiladis (1999). 128-day instantaneous slices of geopotential height equatorward of 15 degrees along a single latitude band and a specific pressure level are Fourier transformed in space and time. The absolute magnitude of the spectral components are calculated for resolved zonal wavenumber and frequencies. These spectral data are smoothed ten times with a 1-2-1 filter and the raw spectral data are divided by the smoothed data to highlight spectral peaks that denote wave-like activity.

Second, we follow Hayashi (1982) and Randel and Held (1991) to compute $\mathcal{S} = -1/(a\cos^2\phi)\partial/\partial\phi\left([\overline{u'v'}]\cos^2\phi\right)$, the acceleration of the mean zonal winds by meridional transient eddy momentum flux divergence, as a function of frequency and zonal wavenumber. Primes denote a deviation from the zonal mean, overbar a time mean and brackets a zonal mean. A direct comparison of the decomposed $\mathcal{S}$ and the Wheeler-Kiladis diagrams highlights the tropical modes that play an important role in the equatorial momentum balance.

Parameter	units						control				
$\mathbf{R_o}$					0.001	0.005	0.020	0.56	0.10	1.0	10.3
a	m				2.5e7	1.3e7	6.371e6	1.2e6	2.8e6	9.0e5	2.8e5

$\mathbf{E}$				4.0e-4	1.6e-3	7.9e-3	0.079	0.79	1.6	7.9	
r	days^{-1}			0.005	0.02	0.1	1	10	20	100	

τ		0.063	0.126	0.63	1.26	12.6	101	504	2520	12600	
$\tau_\mathbf{r}$	days	0.005	0.01	0.05	0.1	1	8	40	200	1000	

μ						0.0017	0.017	0.17	0.83	1.7	
$\mathbf{\Delta_v}$	K					0.1	1	10	50	100	

Table 2.2: List of parameter values for all experiments. Each paired set of rows first displays the nondimensional parameter that was changed with the corresponding dimensional parameter value below.

We also translate the wavenumber-frequency information to phase speed of the disturbances for direct comparison with the zonal-mean zonal wind, an analysis that facilitates inspection for wave mean-flow interaction.

2.3 Description of parameter end members

To gain insight into how the nondimensional parameters change the atmospheric circulation we look at the climatological values of zonal mean zonal winds, mass streamfunction, $[\overline{u'v'}]\cos\phi$, and zonal mean temperature for the end members of the parameter space. The results are averaged over the last 2200 days of 3000 day integrations. Since our experiments only change one nondimensional variable at a time we label each figure by the nondimensional parameter that has been changed. For example the $R_o = 10$ figure refers to the experiment where R_o has been changed and all other nondimensional parameters are held fixed at the control Earth-like value. Table 2.2 serves as a reference for all experiments.

2.3.1 Control atmosphere

The Earth-like control atmosphere is shown in Fig. 2.1. The control values of the nondimensional and dimensional parameters can be found in Table 2.2. The control atmosphere, like Earth's atmosphere, does not superrotate. There is a single jet in each hemisphere and easterlies at all equatorial pressure levels. The Hadley cells extend to 30° and a depth of 200 mb. Eddy activity is concentrated in midlatitudes and the tropics are decelerated by eddies in the mean: that is, $\mathcal{S} < 0$ at the equator.

2.3.2 Large thermal Rossby number

The situation changes dramatically at large thermal Rossby number ($R_o = 10$, small radius $a = 2.8e5$ m; Fig. 2.2). The bulk of the atmosphere is taken up by westerlies, with weak

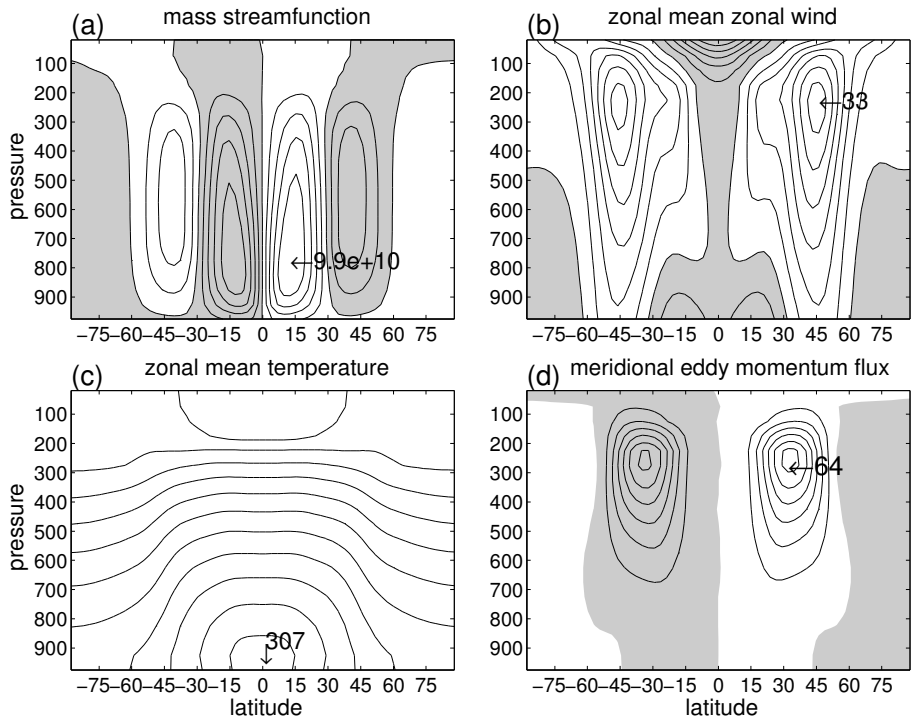


Figure 2.1: Time mean fields for the control atmosphere. (a) Mass streamfunction, contour interval $2x10^{10}$ kg/s. (b) Zonal mean zonal winds, contour interval 5 m/s. (c) Zonal mean temperature, contour interval 10 K. (d) $[\overline{u'v'}]\cos\phi$, contour interval 10 m^2/s^2. Shaded areas negative valued. Largest values highlighted.

jets seen at 60°. The Hadley cell extends farther poleward, as expected from simple scaling arguments (Held and Hou, 1980). The Hadley cell is also significantly shallower and weaker than that of the control atmosphere. The eddy activity has shifted equatorward, weakened and moved to the lower troposphere. The eddies now accelerate the equatorial zonal winds, driving the superrotation. The temperature field is significantly flatter than the control since the 'tropics,' where the Rossby number is large, now extends to the poles (e.g. Sobel et al., 2001).

2.3.3 Small thermal Rossby number

At small thermal Rossby number ($R_o = 0.001$, large radius $a = 2.5e7$ m; Fig. 2.3) the circulation is tightly confined to the tropics, as expected from Held and Hou (1980) scaling.

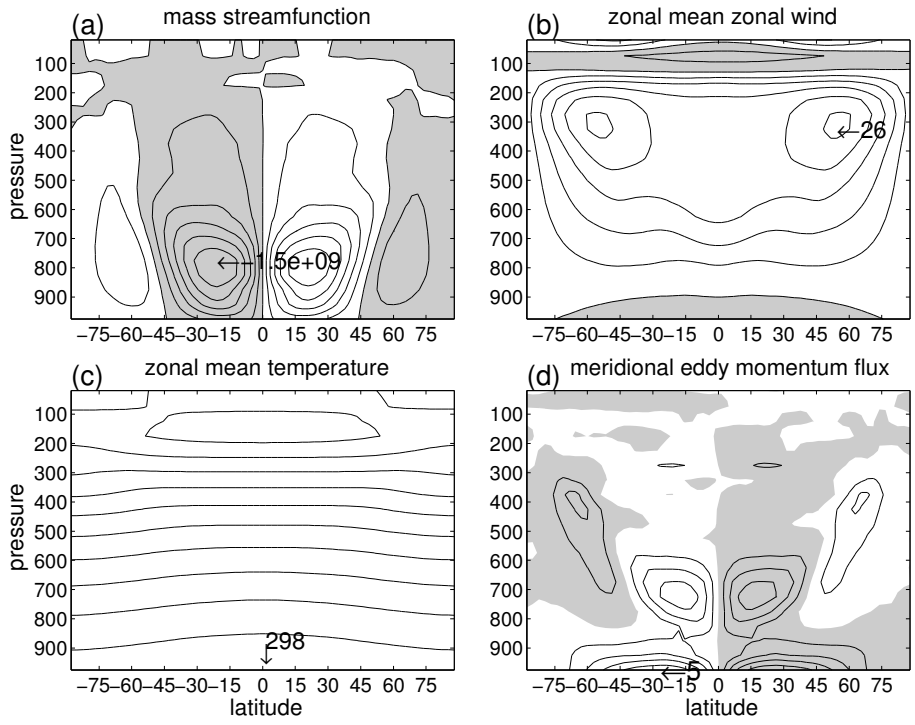


Figure 2.2: Time mean fields for the $R_o = 10$ (small radius) atmosphere. (a) Mass streamfunction, contour interval $2.5x10^8$ kg/s. (b) Zonal mean zonal winds, contour interval 5 m/s. (c) Zonal mean temperature, contour interval 10 K. Shaded areas negative valued. (d) $[\overline{u'v'}] \cos\phi$, contour interval 1 m^2/s^2. Largest values highlighted.

The jets are much higher and weaker than in the control atmosphere. The eddy activity is somewhat higher, narrower (in latitude), and weaker. The equatorial surface temperature is warmer while the poles are colder than the control. One interesting similarity between the small thermal Rossby number atmosphere and the large thermal Rossby number atmosphere (Fig. 2.2) is the relatively weak eddy activity, relative to the control atmosphere. In the small thermal Rossby number atmosphere, the meridional gradient of temperature is decreased because the scale of the planet is greatly increased (in $(1/a)\partial T/\partial\phi$, the radius is larger). In the large thermal Rossby number atmosphere, the meridional temperature gradient is also decreased, but in this case it is due to an extremely efficient Hadley cell transporting tropical heat polewards.

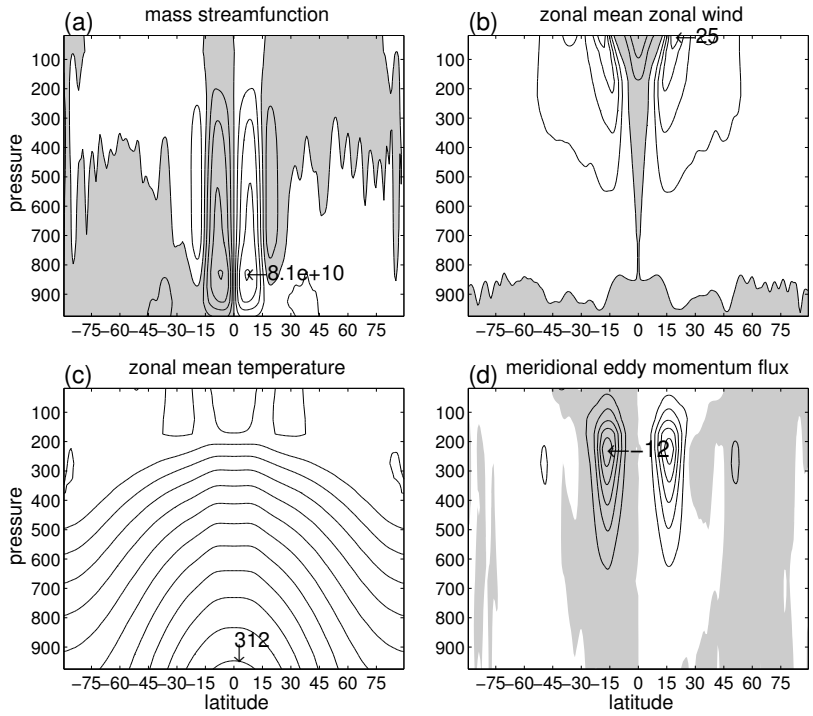


Figure 2.3: Time mean fields for the $R_o = 0.001$ (large radius) atmosphere. (a) Mass streamfunction, contour interval $2e10$ kg/s. (b) Zonal mean zonal winds, contour interval 5 m/s. (c) Zonal mean temperature, contour interval 10 K. Shaded areas negative valued. (d) $[\overline{u'v'}]\cos\phi$, contour interval 2 $\mathrm{m}^2/\mathrm{s}^2$. Largest values highlighted.

2.3.4 Nondimensional radiative timescale

With a small nondimensional radiative timescale ($\tau = 0.063$, strong Newtonian cooling $\tau_r = 0.005$ days; Fig. 2.4), the Newtonian cooling term strongly restores temperatures to the forcing profile. As the forcing profile has its baroclinic zone much closer to the equator than the control climate (compare to Fig. 2.1c) the jets and Hadley cell are collapsed equatorward. The strict relaxation back to the forcing profile may also explain why the jet cores shift upwards: in this strongly damped climate the meridional temperature gradient no longer changes sign moving from the surface to the upper troposphere. Because radiative cooling balances heating by subsidence in the Hadley cell's descending branch (Held and Hou, 1980), strong diabatic cooling allows the Hadley cell to strengthen. Strong easterlies lie over the entirety of the tropics.

At large radiative timescale ($\tau = 12600$, weak Newtonian cooling $\tau_r = 1000$ days; Fig. 2.5) the Newtonian cooling term is much weaker. A meridionally confined Hadley circulation allows for a second thermally direct circulation at higher latitudes. A second (weak) jet and region of surface westerlies can be seen at higher latitudes. The eddy activity shrinks equatorward and becomes much weaker relative to the control.

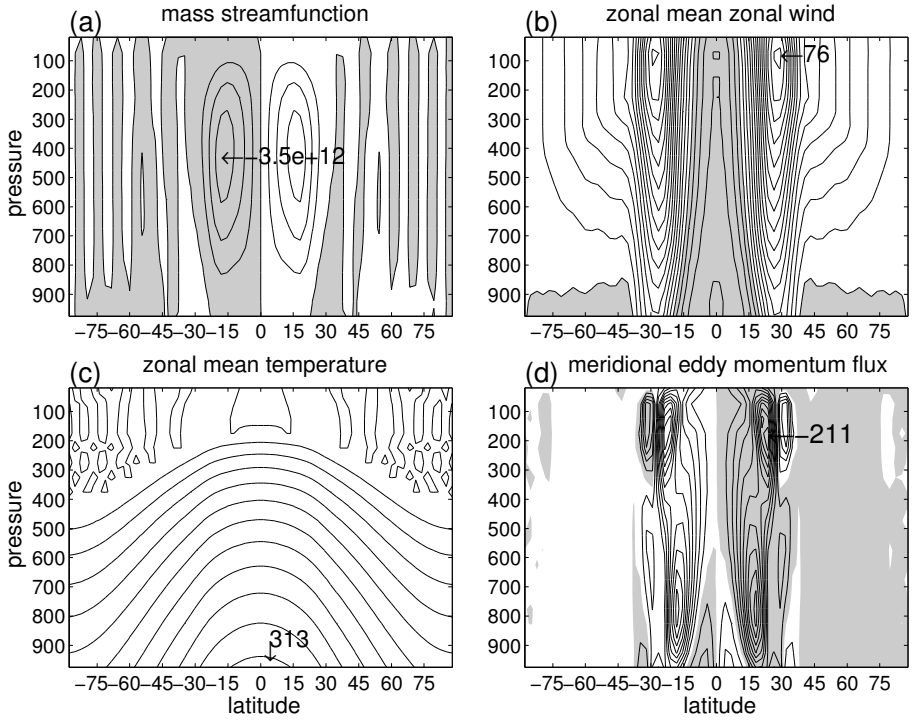


Figure 2.4: Time mean fields for the $\tau = 0.063$ (strong Newtonian cooling) atmosphere. (a) Mass streamfunction, contour interval $1x10^{12}$ kg/s. (b) Zonal mean zonal winds, contour interval 5 m/s. (c) Zonal mean temperature, contour interval 10 K. (d) $[\overline{u'v'}]\cos\phi$, contour interval 20 m^2/s^2. Shaded areas negative valued. Largest values highlighted.

2.3.5 Ekman number

At large Ekman number ($E = 7.9$, strong friction $r = 100$ days^{-1}; Fig. 2.6) weak westerlies lie over the equator from the middle to high troposphere, and eddy activity has been damped by the strong friction. The Held–Suarez frictional layer extending from 1000 mb to 700 mb exerts an enormous influence on the structure of the Hadley cell, which now expands to fill the

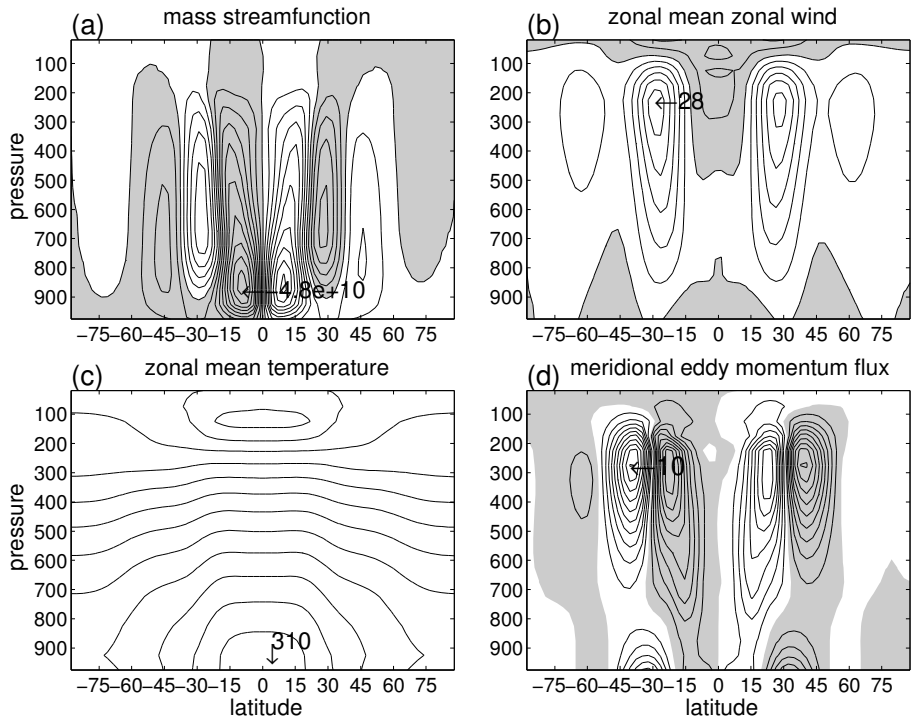


Figure 2.5: Time mean fields for the $\tau = 12600$ (weak Newtonian cooling) atmosphere. (a) Mass streamfunction, contour interval $5x10^9$ kg/s. (b) Zonal mean zonal winds, contour interval 5 m/s.(c) Zonal mean temperature, contour interval 10 K. Shaded areas negative valued. (d) $[\overline{u'v'}]\cos\phi$, contour interval 1 $\mathrm{m}^2/\mathrm{s}^2$. Largest values highlighted.

entire domain. The frictional layer can also be seen in the zonal mean zonal winds with the 'surface westerlies' appearing up to 800 and 700 mb. Above the boundary layer, however, the Hadley cell resembles the control case with a slightly weaker mass flux. The strong friction damps the effectiveness of eddy heat transport and the zonal mean temperature is not far removed from the Newtonian cooling profile.

At small Ekman number ($E = 4.0e{-}4$, weak friction $r = 0.005$ days^{-1}; Fig. 2.7) extremely strong easterlies lie at the equator. The global winds have strengthened considerably and the jets have moved upwards and polewards. The eddy activity, however, is quite weak. The slanted Hadley Cell and eddy variability show that the atmosphere experiences strong symmetric instabilities.

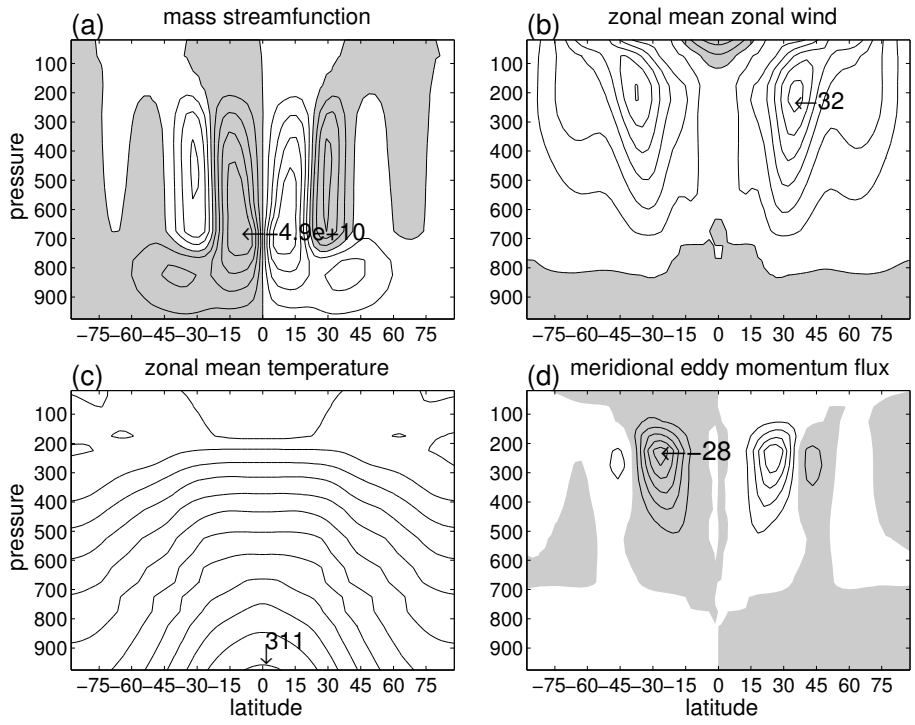


Figure 2.6: Time mean fields for the $E = 7.9$ (strong friction) atmosphere. (a) Mass streamfunction, contour interval $1x10^{10}$ kg/s. (b) Zonal mean zonal winds, contour interval 5 m/s. (c) Zonal mean temperature, contour interval 10 K. (d) $[\overline{u'v'}]\cos\phi$, contour interval 5 $\mathrm{m}^2/\mathrm{s}^2$. Shaded areas negative valued. Largest values highlighted.

2.3.6 Nondimensional vertical temperature gradient

An atmosphere with small vertical temperature forcing gradient ($\mu = 0.0017$, weak stratification $\delta_v = 0.1$ K; Fig. 2.8) has a Hadley cell that only reaches to 15°. The Hadley cell has strengthened by 50% over the control atmosphere to compensate for weaker subsidence heating in its downward branch. The jets and eddy activity both move equatorward. In addition to eddy activity weakening, the characteristic zonal wavenumber increases from 6 in the control to 8 (not shown). This change in eddy length scale reflects the change in stratification and, consequently, the change in the deformation radius.

A large vertical temperature forcing gradient ($\mu = 1.7$, strong stratification $\delta_v = 100$ K; Fig. 2.9), has a more dramatic effect. There is modest equatorial superrotation at several pressure levels, although there is little indication of acceleration by horizontal eddy fluxes.

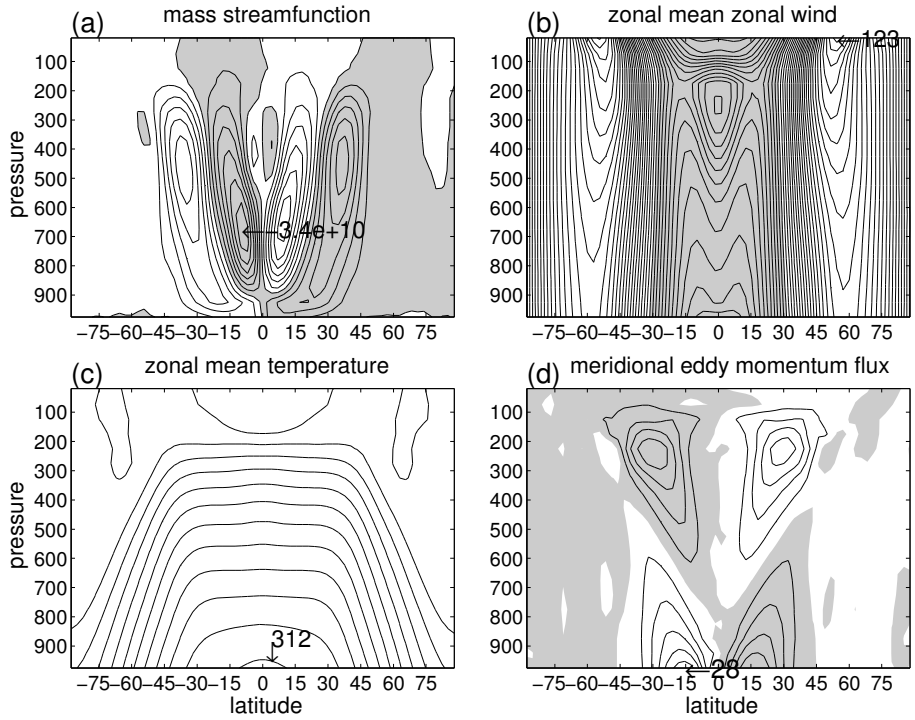


Figure 2.7: Time mean fields for the $E = 4.0e-4$ (weak friction) atmosphere. (a) Mass streamfunction, contour interval $5x10^9$ kg/s. (b) Zonal mean zonal winds, contour interval 5 m/s. (c) Zonal mean temperature, contour interval 10 K. (d) $[\overline{u'v'}]\cos\phi$, contour interval 5 m^2/s^2. Shaded areas negative valued. Largest values highlighted.

The Hadley cell is weaker, wider and taller than the control, while jets and eddy activity have strengthened and shifted poleward and upward. In contrast to the weak stratification atmosphere the characteristic zonal wavenumber has decreased to 3, reflecting the strong stratification's effect on the deformation radius. The entire depth of the tropical atmosphere is significantly warmer and the stratosphere has disappeared.

2.4 Superrotation parameter regime

Fig. 2.10 summarizes the model integrations in parameter space. Fig. 2.10a plots the pressure weighted vertical-, time- and zonal-mean equatorial zonal wind versus the four nondimensional parameters discussed above. Fig. 2.10b plots the maximum (in the vertical) of the equatorial zonal mean zonal wind.

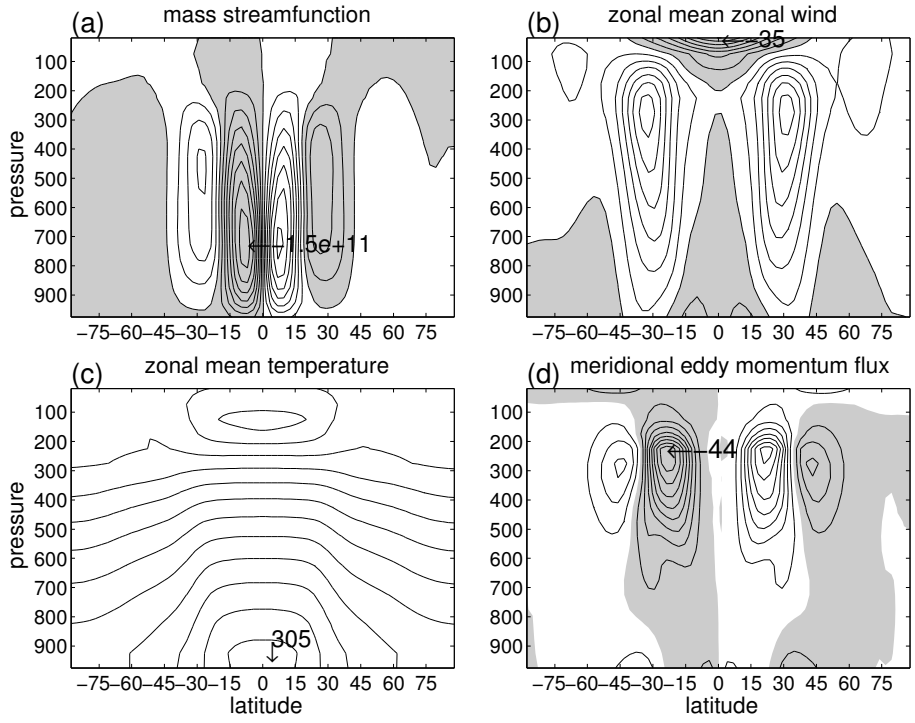


Figure 2.8: Time mean fields for the $\mu = 0.0017$ (weak stratification) atmosphere. (a) Mass streamfunction, contour interval $2x10^{10}$ kg/s. (b) Zonal mean zonal winds, contour interval 5 m/s. (c) Zonal mean temperature, contour interval 10 K. (d) $[\overline{u'v'}]\cos\phi$, contour interval 5 $\mathrm{m}^2/\mathrm{s}^2$. Shaded areas negative valued. Largest values highlighted.

The figure showing maximum equatorial winds is included for completeness but we concentrate on superrotation in the vertical mean. To understand this we manipulate the zonal momentum equation (2.1) by decomposing fields into zonal means and deviations following, for example, Kraucunas and Hartmann (2005), to get

$$\frac{\partial[\overline{u}]}{\partial t} = f[\overline{v}] - [\overline{v}]\frac{1}{a\cos\phi}\frac{\partial}{\partial\phi}\left([\overline{u}]\cos\phi\right) - [\overline{\omega}]\frac{\partial[\overline{u}]}{\partial p} - \frac{1}{a\cos^2\phi}\frac{\partial}{\partial\phi}\left([\overline{u'v'}]\cos^2\phi\right) - \frac{\partial[\overline{u'\omega'}]}{\partial p} - [\overline{F_x}]. \tag{2.6}$$

Where primes again denote a deviation from the zonal mean, overlines denote a time average, brackets denote zonal means and F_x is the Rayleigh drag acting on the zonal flow. The metric terms and diffusion of horizontal momentum are neglected. $[\overline{u'v'}]$ is the transient meridional

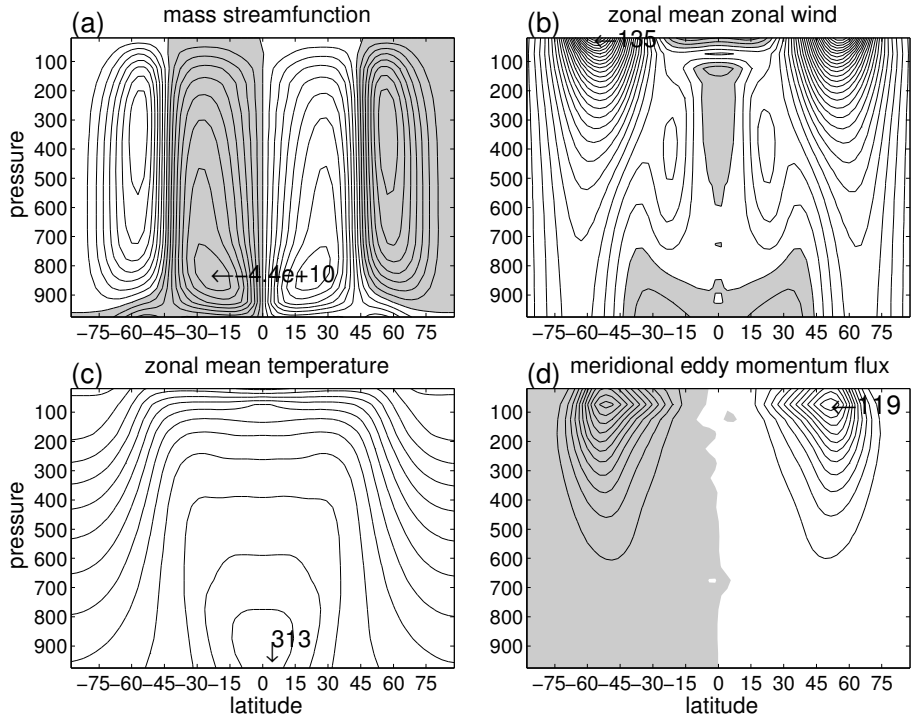


Figure 2.9: Time mean fields for the $\mu = 1.7$ (strong stratification) atmosphere. (a) Mass streamfunction, contour interval $5x10^9$ kg/s. (b) Zonal mean zonal winds, contour interval 5 m/s. (c) Zonal mean temperature, contour interval 10 K. (d) $[\overline{u'v'}]\cos\phi$, contour interval 10 $\mathrm{m}^2/\mathrm{s}^2$.Shaded areas negative valued. Largest values highlighted.

zonal momentum flux and $[\overline{u'\omega'}]$ is the transient vertical zonal momentum flux. As a note these equations are only valid for axisymmetric forcing that is constant in time and the inclusion of zonally asymmetric forcing would add stationary eddy terms in both meridional and vertical zonal momentum flux. Taking the pressure weighted vertical mean (denoted by $\langle * \rangle$) of (2.6) and using the zonal mean mass conservation equation gives

$$\frac{\partial \langle [\overline{u}] \rangle}{\partial t} = -\frac{1}{a\cos^2\phi}\frac{\partial}{\partial \phi}\left(\langle [\overline{u}][\overline{v}] \rangle \cos^2\phi\right) - \frac{1}{a\cos^2\phi}\frac{\partial}{\partial \phi}\left(\langle [\overline{u'v'}] \rangle \cos^2\phi\right) - \langle r[\overline{u}] \rangle. \qquad (2.7)$$

In the vertical mean the the Coriolis term disappears due to mass conservation — there cannot be a mean flow of mass out of the column. More importantly for our study the vertical eddy momentum flux divergence term disappears since $[\overline{u'\omega'}]$ is zero at the surface and the top of the atmosphere. Combining equation (2.7) with Hide's theorem — a maximum in angular

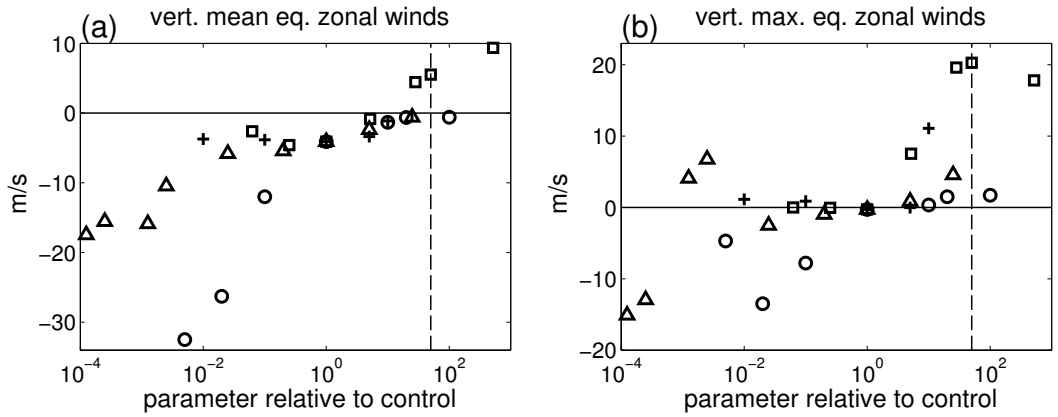


Figure 2.10: (a) Vertical mean equatorial winds and (b) Maximum equatorial winds as a function of nondimensional parameters. Squares indicate an experiment with the thermal Rossby number varied, triangles the nondimensional radiative timescale, circles the Ekman number, and pluses the nondimensional vertical temperature gradient. Nondimensional parameters are normalized by their control value. As a reference the vertical dashed line denotes the location of the $R_o = 1$ (fifty times larger than the control $R_o = 0.02$) case which is discussed in detail in the text.

momentum must be maintained by eddy momentum transport — says that superrotation in the vertical mean must be maintained by meridional eddy momentum fluxes. Conversely when superrotation exists at only a few model levels but the vertical mean equatorial winds are easterly the superrotation can be driven by either vertical or horizontal eddy momentum fluxes. This provides a way to distinguish between superrotation that is definitely (i.e., the QBO and some models of Venus' superrotation, e.g. Fels and Lindzen (1974); Zhu (2006)) or may possibly be (i.e., the small τ runs; Fig. 2.4) driven by vertical eddy momentum fluxes and that which is definitely driven by meridional momentum fluxes (i.e., the large R_o runs; Fig. 2.2).

As an aside equation (2.7) provides a fundamentally different view of the columnar momentum balance between the equator of a permanent equinox superrotating atmosphere and the midlatitudes of an Earth-like atmosphere. In the midlatitudes of Earth-like atmospheres equation (2.7) can be approximated as (in steady state) $\langle \mathcal{S} \rangle = \langle r[\overline{u}] \rangle$ (e.g. Schneider, 2006). This balance can be interpreted as the need for surface westerlies to remove westerly momen-

tum from the column in the same region where Rossby waves flux westerly momentum into the column. However this balance is fundamentally different at the equator of a superrotating permanent equinox atmosphere. The balance now requires another term and becomes $1/(a\cos^2\phi)\partial/\partial\phi\left(\langle[\overline{u}][\overline{v}]\rangle\cos^2\phi\right) = \langle\mathcal{S}\rangle - \langle r[\overline{u}]\rangle$. As we have argued above an atmosphere with westerlies in the equatorial vertical mean must have $\mathcal{S} > 0$. Additionally, the Rayleigh drag term $-\langle r[\overline{u}]\rangle$ is also greater than zero because there are mean easterlies in the tropical boundary layer due to the return flow of the Hadley cell. Therefore both eddies and drag add momentum to the equatorial atmosphere and the Hadley cell takes it away.

Going back to Fig. 2.10a, vertical-mean equatorial westerlies only exist at large thermal Rossby number (squares), and so it is the dominant control parameter for superrotation driven by meridional momentum fluxes. Starting from an Earth-like atmosphere, for strong stability (large Δ_v; pluses), strong friction (circles), and weak radiative damping (triangles) the vertical mean winds go to zero. On the other end of the parameter range strong easterlies dominate at small nondimensional radiative timescale and Ekman number. A similar parameter sweep starting from a large thermal Rossby number atmosphere rather than the Earth-like control can be found in Pinto and Mitchell (2014).

The maximum equatorial zonal winds show less organized trends. For the nondimensional radiative timescale (triangles), for instance, the model produces superrotation in at least one pressure level on either side of the control run. Also for Δ_v (pluses), there is strong superrotation at large values and there is very weak superrotation at small values. The maximum equatorial wind dependence of the thermal Rossby number (squares) is similar to the dependency of the vertical mean, with westerlies existing for larger parameters.

Taken together, the most robust conclusion is that the thermal Rossby number is the dominant control parameter for equatorial superrotation.

2.5 Spectral characteristics of the intermediate thermal Rossby number modes

We now turn our focus to better understanding the variability driving the superrotation in the intermediate thermal Rossby number atmospheres. We focus on the $R_o = 1$ ($a = 9e5$) m atmosphere since the $R_o = 10$ ($a = 2.8e5$) m atmosphere is less amenable to analysis and was explored in depth in MV10. Fig. 2.11 shows climatological values for the $R_o = 1$ atmosphere. The $R_o = 1$ atmosphere superrotates more weakly than the $R_o = 10$ atmosphere (fig 2.2) but does contain somewhat stronger eddies. This likely reflects the fact that, unlike the $R_o = 10$ atmosphere, the $R_o = 1$ zonal mean state (Fig. 2.11d) retains some of the control atmosphere's tendency for baroclinic instability.

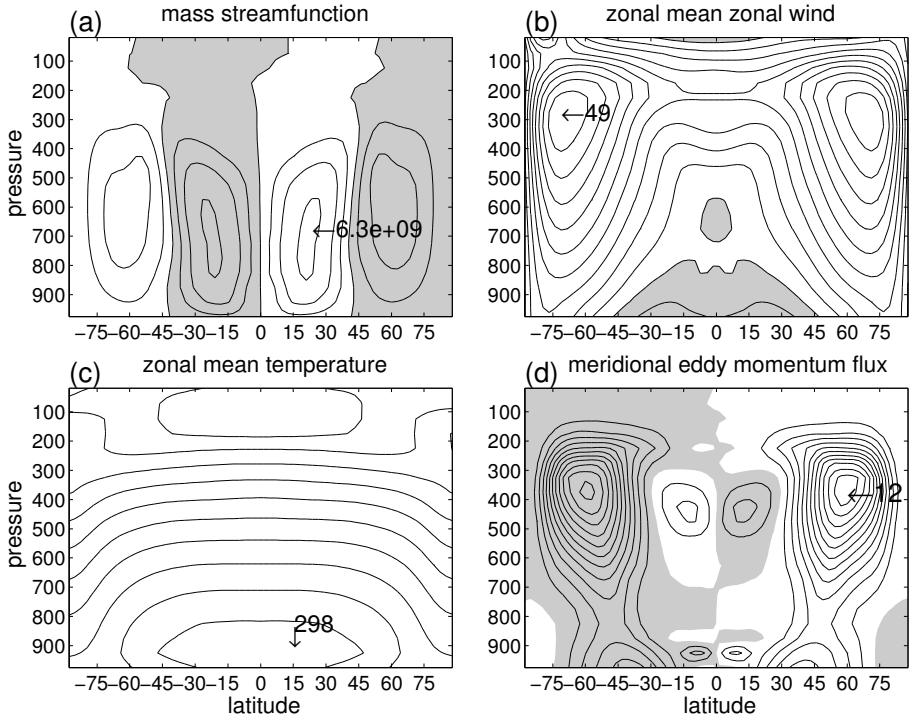


Figure 2.11: Time mean fields for the $R_o = 1$ atmosphere. (a) Mass streamfunction, contour interval $2x10^9$ kg/s. (b) Zonal mean zonal winds, contour interval 5 m/s. (c) Zonal mean temperature, contour interval 10 K. (d) $[\overline{u'v'}]\cos\phi$, contour interval 1 m^2/s^2. Shaded areas negative valued. Largest values highlighted.

We use the spectral methods of Wheeler and Kiladis (1999), Hayashi (1982), and Randel and Held (1991) to identify the tropical mode that gives rise to superrotation. A symmetric mode Wheeler-Kiladis diagram of the geopotential height field at 275 mb for the control atmosphere is shown in Fig. 2.12a. Overlaid with solid lines are theoretical shallow water dispersion curves for Kelvin waves and $n = 1$ equatorial Rossby waves. These curves are drawn for equivalent depths $H = 12, 40, 200$ m. The clearest signal is the Kelvin wave corresponding to an equivalent depth of 40 m. On the westward (left hand) side of the figure the clearest signal is a global Rossby-Haurwitz wave (Hendon and Wheeler, 2008; Kasahara, 1980). The Rossby-Haurwitz dispersion relation can be approximately represented by the equatorial Rossby wave dispersion relation with a large equivalent depth and a Doppler shifting wind (Hendon and Wheeler, 2008). In this model an equivalent depth of 13 km and a Doppler shifting wind of 15 m/s provides a good fit to the Rossby-Haurwitz mode. The large equivalent depth of the Rossby-Haurwitz mode is due to its barotropic structure.

How does this compare to the real atmosphere? Fig. 2.13a is a symmetric mode Wheeler-Kiladis diagram for brightness temperature from the CLAUS data set (Environmental Systems Science Center, Project Scientist G.J. Robinson, 2002-). There are readily apparent differences. The strongest signal is the Madden-Julian oscillation at low frequencies and wavenumbers 1-5 (e.g. Wheeler and Kiladis, 1999; Zhang, 2005). A strong n=1 equatorial Rossby wave signal is apparent in the CLAUS data. It is not surprising that the dry model does not mimic real world variability with any particular accuracy: the dry model has extremely idealized physics and, most importantly, no moist convection parameterization. Though the Rossby-Haurwitz mode does not show up when looking at brightness temperature it is visible for Earth's atmosphere in dynamical fields like u or geopotential height (Hendon and Wheeler, 2008).

The Wheeler-Kiladis diagram for the geopotential height field at 475 mb in the $R_o = 1$ ($a = 9e5$ m) is shown in Fig. 2.14a. The level of the analysis is dropped from 275 to 475 mb to

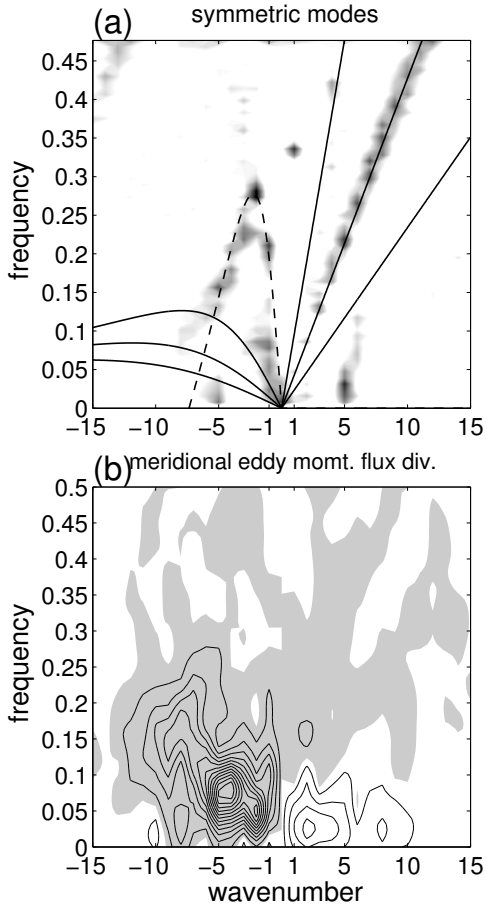


Figure 2.12: Spectral diagnostics for the control atmosphere at 275 mb. (a) Symmetric mode Wheeler-Kiladis diagram of the geopotential height field. Maximum amplitude 2.4. Solid curves show theoretical dispersion relations for Kelvin waves ($k > 0$) and equatorial Rossby waves ($k < 0$) of equivalent depths $H = 200, 40, 12$ m. Dashed curve shows theoretical dispersion relation for a Rossby-Haurwitz wave with equivalent depth of 13 km Doppler shifted by a 15 m/s wind. (b) $\mathcal{S}$ in $\omega - k$ space at the equator at 275 mb. Shaded values negative. Contour intervals arbitrary.

reflect the fact that eddy activity is lower in the high R_o atmospheres. Changing the pressure level of this analysis does not qualitatively change the results and Figs. 2.12a, 2.13a, and 2.14a are meant to be compared directly. Fig. 2.14a plots frequencies up to 1/day to better capture the shift to higher frequency variability when the radius is decreased. Fig. 2.14a shows a much simpler picture than that of the control atmosphere. Almost all westward activity has vanished and the primary variability are wavenumber-1 and 2 Kelvin waves. Note that the dispersion curves are steeper as the planetary radius a has decreased. It is interesting

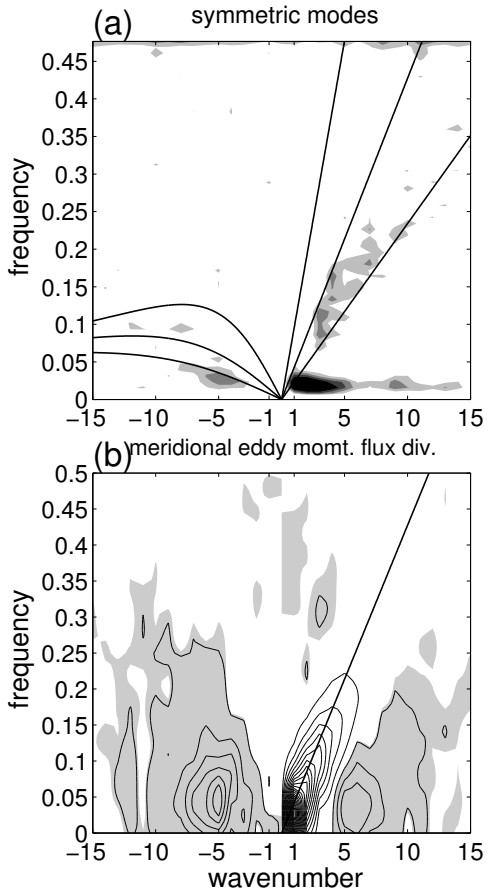


Figure 2.13: Spectral diagnostics for Earth's atmosphere. (a) Symmetric mode Wheeler-Kiladis diagram for the CLAUS brightness temperature data set. Maximum amplitude 1.9. Solid curves show theoretical dispersion relations for Kelvin waves ($k > 0$) and equatorial Rossby waves ($k < 0$) of equivalent depths $H = 200, 40, 12$ m. (b) $\mathcal{S}$ in $\omega - k$ space at the equator and 200 mb for the NCEP II Reanalysis. Solid line shows the $H = 40$ Kelvin wave dispersion relation. Shaded values negative. Contour intervals arbitrary.

that the dominant Kelvin wave variability in both the control and $R_o = 1$ atmospheres lie along the 40 m equivalent depth line. In their paper Wheeler and Kiladis (1999) noted that the background OLR spectrum is slightly weighted toward westward wavenumbers due to the climatological easterlies overlying the equator. Assuming a half-wavelength structure in the troposphere (e.g. Kiladis et al., 2009) and the climatological temperature fields both the control and $R_o = 1$ atmosphere have tropical equivalent depths of approximately 40 m, which agrees with Figs. 2.12a and 2.14a. It is therefore somewhat surprising that the Kelvin

wave variability in 2.14a lies along the 40 m equivalent depth line since any Kelvin wave would experience strong superrotating westerlies and would consequently be expected to be Doppler-shifted to higher eastward frequencies. It is possible that the Kelvin wave has a steering level in the lower atmosphere where zonal winds are near zero but this needs to be investigated further.

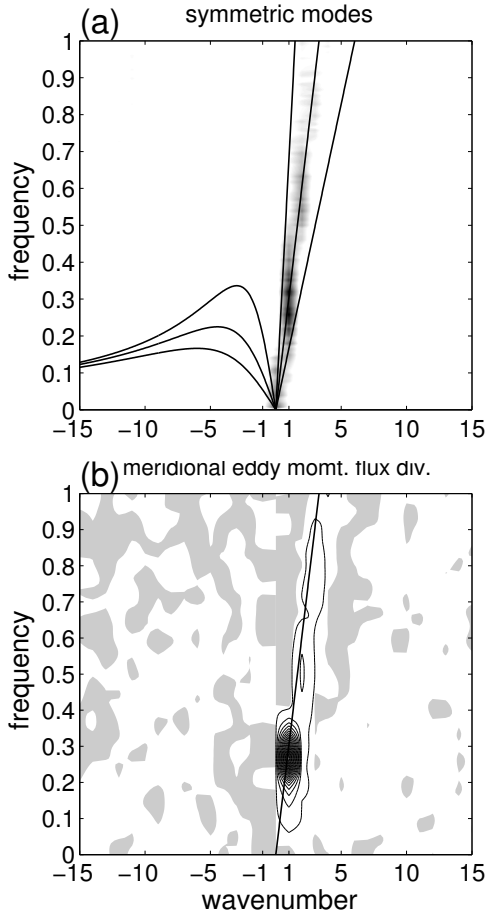


Figure 2.14: Spectral diagnostics for the $R_o = 1$ atmosphere at 475 mb. (a) Symmetric mode Wheeler-Kiladis diagram of the geopotential height field. Maximum amplitude 5.8. Solid curves show theoretical dispersion relations for Kelvin waves ($k > 0$) and equatorial Rossby waves ($k < 0$) of equivalent depths $H = 200, 40, 12$ m. (b) $\mathcal{S}$ in $\omega - k$ space at the equator. Solid line shows the $H = 40$ Kelvin wave dispersion relation. Shaded values negative. Contour intervals arbitrary.

While it is clear that the control and $R_o = 1$ atmospheres have very different equatorial variability it is unclear what is producing superrotation in the latter case. To answer this

question figures 2.12b and 2.14b plot equatorial $\mathcal{S}$, the transient eddy driving of zonal mean zonal winds, in the same frequency-wavenumber space as the Wheeler-Kiladis diagrams discussed above (Hayashi, 1982; Randel and Held, 1991). This figure makes it possible to not only see which modes are present in the tropics but which are important for the tropical momentum balance. In Fig. 2.12b the control atmosphere $k > 0$ eddies accelerate the zonal wind. This acceleration peaks at $k = 1$ and extends at low frequency to higher wavenumbers. It is possible this variability is due to low frequency Kelvin waves. On the $k < 0$ side of the spectrum what appears to be a combination of Rossby-Haurwitz waves propagating from midlatitudes and equatorial mixed Rossby-gravity waves decelerate the zonal wind. This stands in stark contrast to the eddy driving in the $R_o = 1$ atmosphere, Fig. 2.14b, where the only significant features are at wavenumbers 1 and 2. These features exactly correspond to the Kelvin waves highlighted in Fig. 2.14a.

As a sidenote, not too much should be read into the resemblance between the low frequency $k > 0$ variability in the control dry atmosphere (Fig. 2.12b) and the MJO in Earth's atmosphere (Fig. 2.13b). The point in the control atmosphere at which the Fig. 2.12b decomposition is done in the dry model, 275 mb at the equator, has in its mean state a meridional eddy acceleration of -0.06 m/s/day. This is extremely weak variability when compared to the much larger acceleration of 1.8 m/s/day at 475 mb at the equator for the $R_o = 1$ atmosphere in Fig. 2.14, where the Kelvin wave signal is much stronger.

A plot of $\mathcal{S}$ as a function of phase speed and latitude is also shown in Fig. 2.15. The Kelvin wave's influence can be seen to extend 50 degrees from the equator, just beyond what appears to be a critical/turning line, where it draws momentum from the mean flow and deposits it at the equator. At higher latitudes, a separate mode is transporting momentum from even higher latitudes to the Kelvin wave's sink region. These modes combine in a "bucket brigade" to produce equatorial superrotation from the momentum of the high-latitude jets. The connection between the high and low latitudes mode can also be seen in the dashed curve

which shows a line of constant angular frequency which corresponds to the peak Kelvin wave speed of 18 m/s at the equator. The acceleration due to the Kelvin wave is balanced by deceleration with the same angular velocity at higher latitudes.

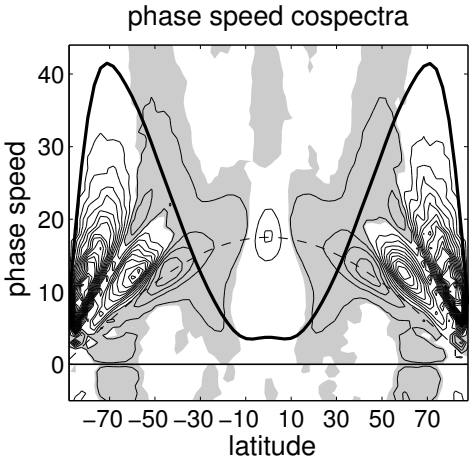


Figure 2.15: Contours of $\mathcal{S}$ as a function of phase speed and latitude at 475 mb for the $R_o = 1$ atmosphere. Dark line shows the time mean zonal mean zonal wind at the same pressure level. Shaded values negative. Contour intervals arbitrary. The dashed line shows the angular frequency corresponding to the peak Kelvin wave speed of approximately 18 m/s at the equator.

It is not immediately obvious that a Kelvin wave can transport momentum meridionally since in the standard theory the wave does not manifest itself in the meridional velocity field: $v' = 0$ (Matsuno, 1966). However, studies have shown the importance of Kelvin wave momentum fluxes in Venus-like models (Iga and Matsuda, 2005; Imamura, 2006) and Showman and Polvani (2011) showed that if phased correctly a Kelvin wave and an equatorial Rossby wave can produce equatorward momentum fluxes. Imamura et al. (2004) showed that in the presence of a meridional circulation that maintains meridional shear a Kelvin wave does have a small but important v' component that can lead to zonal accelerations. It is possible this explains the momentum fluxes found in the $R_o = 1$ as an inspection of Fig. 2.11 shows that the deep tropical momentum fluxes are collocated with the outflow of the Hadley cell. The specific structure of this Kelvin wave does need to be understood in greater detail but we can conclude that the superrotation in the intermediate thermal Rossby number

atmospheres is a direct result of Kelvin waves fluxing momentum meridionally into the deep tropics.

Further proof of the relevance of Kelvin wave meridional momentum transport in intermediate thermal Rossby number atmospheres is demonstrated in Fig. 2.16. $\mathcal{S}$ as a function of wavenumber and frequency is shown at the equator for the $R_o = 0.1$ ($a = 2.8e6$) m and $R_o = 0.55$ ($a = 1.2e6$) m atmospheres. Eastward accelerations can be seen lying along the $H = 40m$ Kelvin wave dispersion curve.

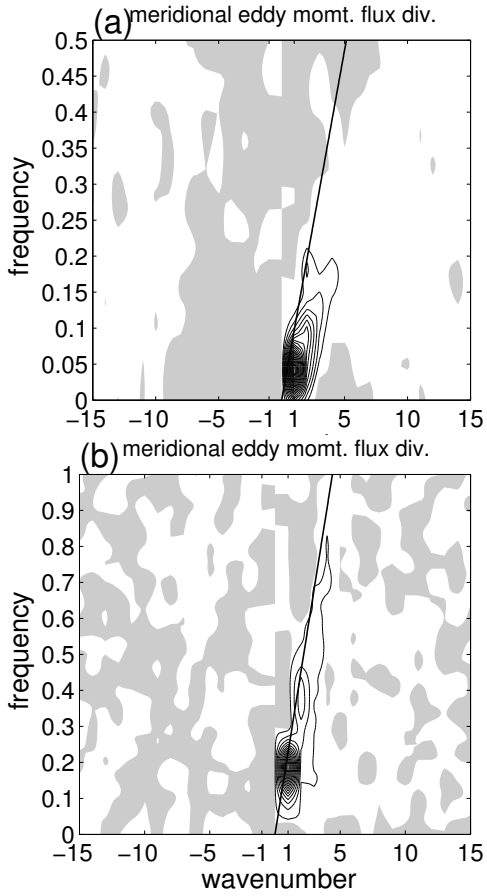


Figure 2.16: (a) $\mathcal{S}$ in $\omega - k$ space at the equator for (a) the $R_o = 0.1$ atmosphere at 275 mb and (b) the $R_o = 0.55$ atmosphere at 425 mb. Solid line shows the $H = 40$ Kelvin wave dispersion relation. Shaded values negative. Contour intervals arbitrary.

2.5.1 Wavenumber-frequency filtering

To provide further evidence of the dry dynamical core's Kelvin wave we use wavenumber-frequency filtering to show the structure of the model's primary modes (e.g. Straub and Kiladis, 2003a). A time series of zonal wind at 475 mb and a single equatorial latitude is Fourier transformed in time and space and filtered to only retain variability that exists for $k = 1$ and frequencies between 0.17 and 0.37 1/day. This filtered variability is inverse Fourier transformed to provide a time series that is regressed against u, v and geopotential height. This process gives Fig. 2.17 which shows that the equatorial variability in the $R_o = 1$ atmosphere is primarily due to a wavenumber-1 Kelvin wave and the high latitude variability is dominated by a wavenumber-1 Rossby wave. The equatorial part of Fig. 2.17 should be directly compared to the classical Kelvin wave solution of a beta-plane shallow water model such as Fig. 3f of Kiladis et al. (2009). The connection between the Kelvin and Rossby waves seen here also corresponds to the acceleration and deceleration that fall along the same angular frequency curve in Fig. 2.15.

Regressing the first principal component of equatorial zonal wind onto global fields gives a near identical result to Fig. 2.17 (not shown). The wavenumber-1 Kelvin wave (first and second principal components) is responsible for roughly 70% of the equatorial zonal wind variance, the wavenumber-2 Kelvin wave (third and fourth principal components) explains roughly 10% of the variance and the wavenumber-3 Kelvin wave (fifth and sixth principal components) explains about 4% of equatorial variance. This corresponds nicely to the Kelvin wave signal in Fig. 2.14 and further demonstrates the dominance of Kelvin wave variability in the large thermal Rossby number tropical atmospheres.

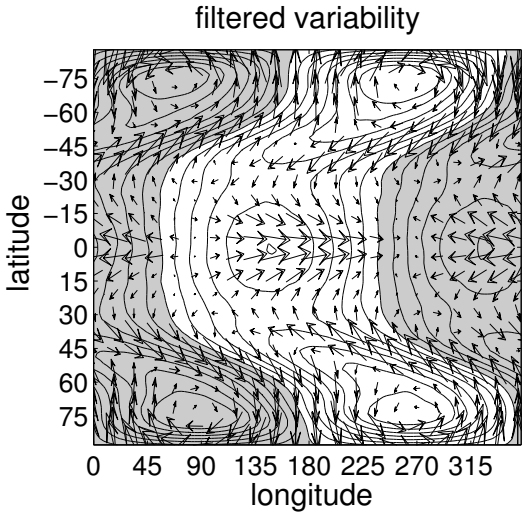


Figure 2.17: Geopotential height (contours) and u and v (arrows) for the $R_o = 1$ atmosphere at 475 mb regressed against an equatorial zonal wind time series filtered to retain only variability existing at wavenumber-1 with frequency between 0.17 and 0.37 1/day. Contour level 2 m with shaded regions negative. Maximum wind vector 4.3 m/s.

2.6 Meridional Kelvin wave momentum transport in other contexts

2.6.1 Kelvin waves in Williams (2003)

Further proof of the importance of Kelvin waves to the tropical momentum balance of dry dynamical cores is found by analyzing the results of Williams (2003). As discussed in the introduction, Williams induced superrotation in a dry dynamical core similar to the one used here by changing the power in the latitudinal distribution of thermal forcing from $\cos^2\phi$ to $\cos^n\phi$. The zonal mean zonal winds for a re-creation of Williams' $n = 16$ results is shown in Fig. 2.18a and should be compared to figure 5a in Williams (2003). Correspondence is not exact due to slight differences in the models' details. As done before the dynamically relevant tropical modes are identified by plotting $\mathcal{S}$ in $\omega - k$ space in Fig. 2.18b. The most prominent signal lies along the equivalent depth of 40 m Kelvin wave dispersion curve, though there are

other features at low frequency and $\pm 5k$. This result shows the relevance of Kelvin waves even in more Earth-like superrotating atmospheres.

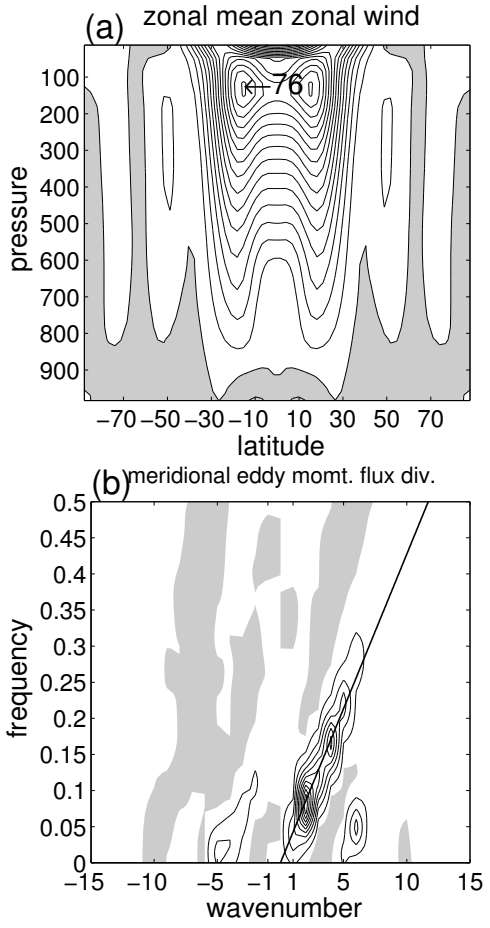


Figure 2.18: For re-creation of the $n = 16$ atmosphere in Williams (2003). (a) Zonal mean zonal winds. Contour interval 5 m/s. Shaded values negative. Largest value highlighted. (b) $\mathcal{S}$ in $\omega - k$ space at 550 mb. Solid line shows the $H = 40$ Kelvin wave dispersion relation. Shaded values negative. Contour intervals arbitrary.

2.6.2 Momentum flux divergence on Earth

There is some correspondence between the dry dynamical core results and Earth's atmosphere. Fig. 2.13b plots $\mathcal{S}$ in $\omega - k$ space for Earth's atmosphere using the daily-averaged 200 mb NCEP-DOE Reanalysis II values of u and v. The strongest signal in the NCEP diagram is at wavenumber one and low frequencies. This overlaps with the MJO signal in

Fig. 2.13a and seems to imply that the strongest source of horizontal eddy momentum flux in the upper equatorial troposphere is associated with the MJO, a result previously shown by Lee (1999). Though the MJO is the largest signal, the Kelvin wave meridional momentum convergence found in the dynamical core also exists in Earth's atmosphere. A clear Kelvin wave signal exists between wavenumbers one and five. In the NCEP II reanalysis the Hadley outflow peaks at 200 mb, which may explain the clear Kelvin wave signal in Fig. 2.13b. At other tropospheric pressure levels the Kelvin signal is weaker while the low frequency, wavenumber-1 signal dominates. This fits within the theory of Imamura et al. (2004) that Kelvin wave momentum flux convergence is reliant on a meridional circulation.

2.7 Sensitivity of the superrotating state to horizontal resolution, vertical resolution, and an upper atmosphere sponge

Since we have used the dynamical core in a circulation regime far from the Earth-like circulation it is made for, we have checked the results discussed above for sensitivity to resolution and a top of atmosphere sponge. Figs. 2.19, 2.20, and 2.21 show the climatologies for the $R_o = 1$ ($a = 9e5m$) atmosphere for T85 horizontal resolution (20 evenly spaced vertical levels, no sponge), 60 unevenly spaced vertical levels (T42, no sponge), and a top-of-atmosphere eddy damping sponge (T42, 20 evenly spaced vertical levels), respectively.

All of these options have very modest effects on the climatology relative to the standard numerics T42, 20 level, no sponge integration (Fig. 2.11), with, for example, maximum wind speeds being changed on the order of 1 m/s, or max temperatures being changed 1 K. The integration higher vertical resolution has considerably more vertical structure, but the superrotation is still clearly present, and reaches a similar magnitude as the standard

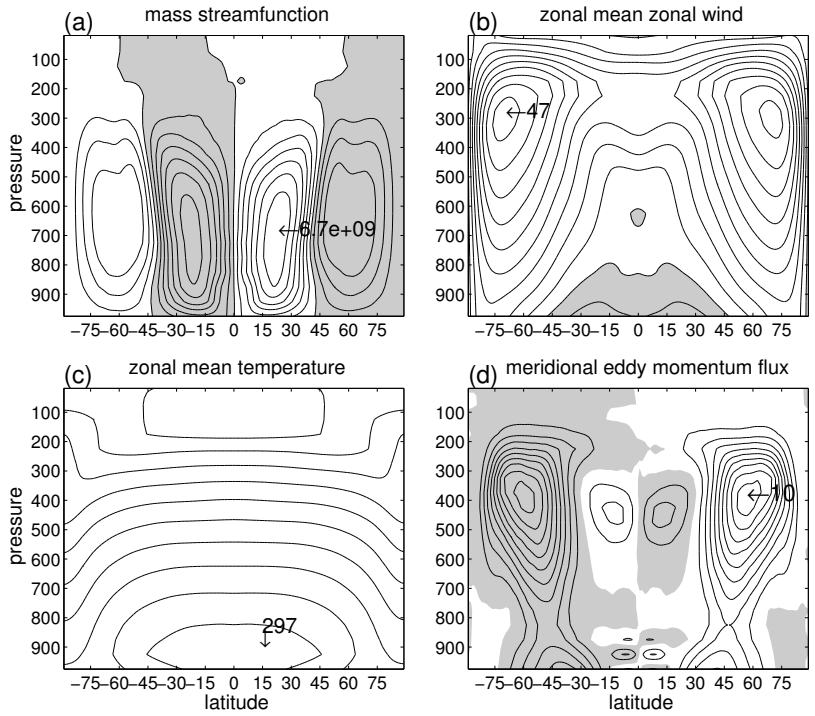


Figure 2.19: Time mean fields for the $R_o = 1$ atmosphere with T85 horizontal resolution. (a) Mass streamfunction, contour interval $1x10^9$ kg/s. (b) Zonal mean zonal winds, contour interval 5 m/s. (c) Zonal mean temperature, contour interval 10 K. (d) $[\overline{u'v'}]\cos\phi$, contour interval 1 m^2/s^2. Shaded areas negative valued. Largest values highlighted.

numerics integration. Both the height and the magnitude of the tropical wave source are very similar across all four runs (compare part d of Figs. 2.11 and 2.19, 2.20, and 2.21).

The spectral characteristics of the $R_o = 1$ atmosphere's tropical variability are also little changed. Fig. 2.22 shows $\mathcal{S}$ in $\omega - k$ space for the three integrations described above and should be compared to Fig. 2.14b, albeit with less temporal resolution and some aliasing of higher-frequency eastward variability. The primary Kelvin wave signal is virtually identical across all four integrations, lying along the $H = 40$ Kelvin wave line and peaking at $k = 1$. Though not shown here, the cospectra (Fig. 2.15) and mode structure (Fig. 2.17) are recreated in the higher resolution and sponge integrations. The robustness of the climatology to changes in the numerics shows that the integrations discussed in detail above are not artifacts of the model numerics.

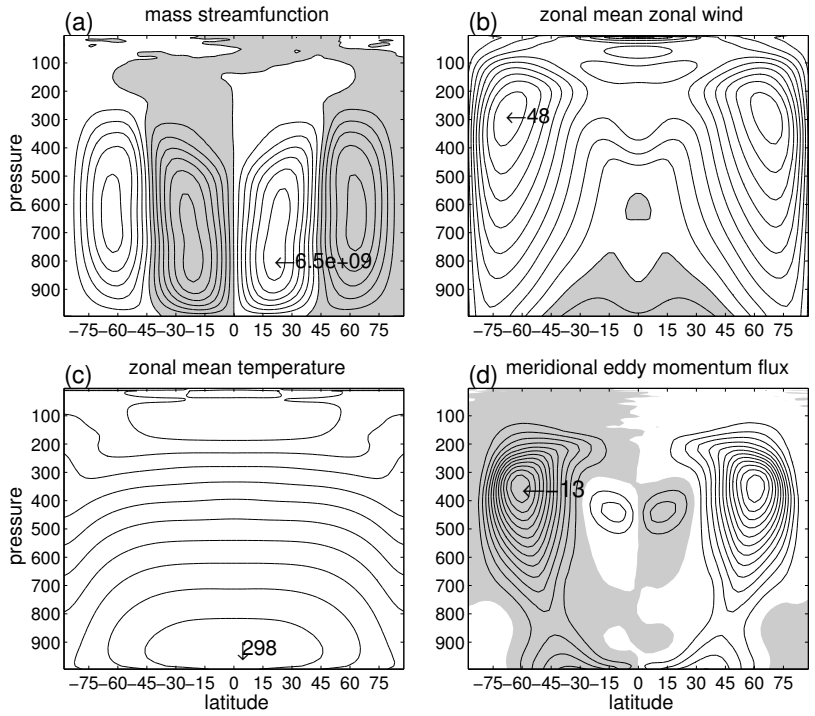


Figure 2.20: Time mean fields for the $R_o = 1$ atmosphere with 60 unevenly spaced vertical levels. (a) Mass streamfunction, contour interval $1x10^9$ kg/s. (b) Zonal mean zonal winds, contour interval 5 m/s. (c) Zonal mean temperature, contour interval 10 K. (d) $[\overline{u'v'}]\cos\phi$, contour interval 1 m^2/s^2. Shaded areas negative valued. Largest values highlighted.

2.8 Discussion and Conclusions

In this paper we have swept through a broad section of the parameter space of a non-convecting dry dynamical core, thermally forced with a Newtonian relaxation, and found that the thermal Rossby number is the most important single nondimensional parameter governing the momentum balance of the equatorial troposphere. A high thermal Rossby is, as in MV10, associated with a superrotating state. Of the other nondimensional quantities, a small Ekman number leads to strong equatorial easterlies, but a large Ekman number only induces weak superrotation at several model levels and not in the vertical mean. As the radiative timescale is decreased the mean equatorial zonal winds become strongly easterly, and as the timescale is increased these winds go to zero. Changing the radiative timescale

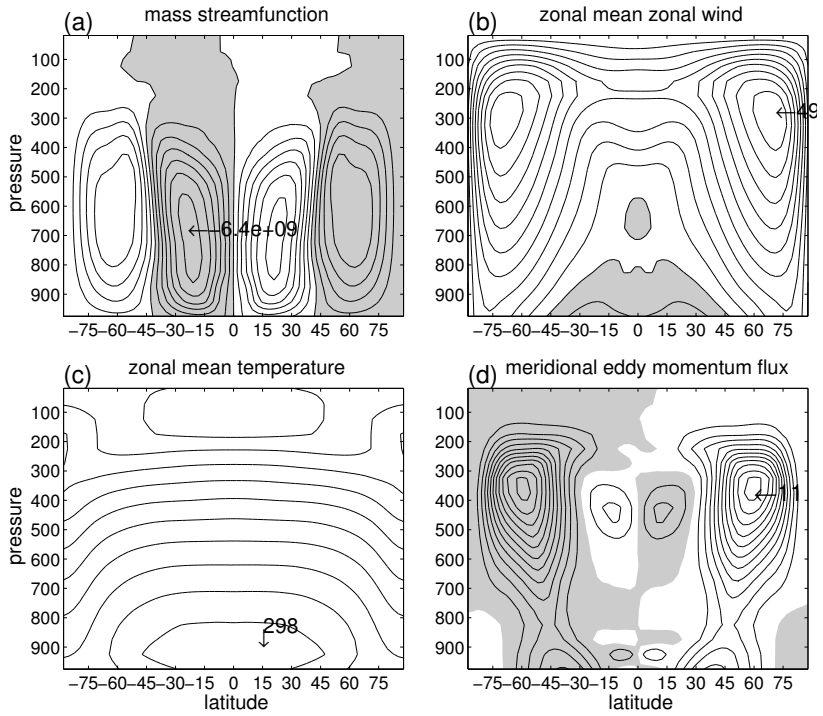


Figure 2.21: Time mean fields for the $R_o = 1$ atmosphere with an eddy-damping sponge at the uppermost layer. (a) Mass streamfunction, contour interval $1x10^9$ kg/s. (b) Zonal mean zonal winds, contour interval 5 m/s. (c) Zonal mean temperature, contour interval 10 K. (d) $[\overline{u'v'}]\cos\phi$, contour interval 1 $\mathrm{m}^2/\mathrm{s}^2$. Shaded areas negative valued. Largest values highlighted.

or the vertical temperature forcing gradient can induce strong superrotation but only at a few pressure levels and not in the vertical mean.

Building on Caballero and Huber (2010) and Lee (1999), when latent heat release is important and organized convection leads to tropical phenomena such as the Madden-Julian oscillation and moist Kelvin modes, a warm and moist atmosphere with large thermal Rossby number is even more likely to superrotate than a dry atmosphere with the same large thermal Rossby number. Lian and Showman (2010) and Liu and Schneider (2011) have shown that convection plays a key role in generating superrotation on planets with larger radii, though it is unclear how their findings relate to our large thermal Rossby number (small radius) results.

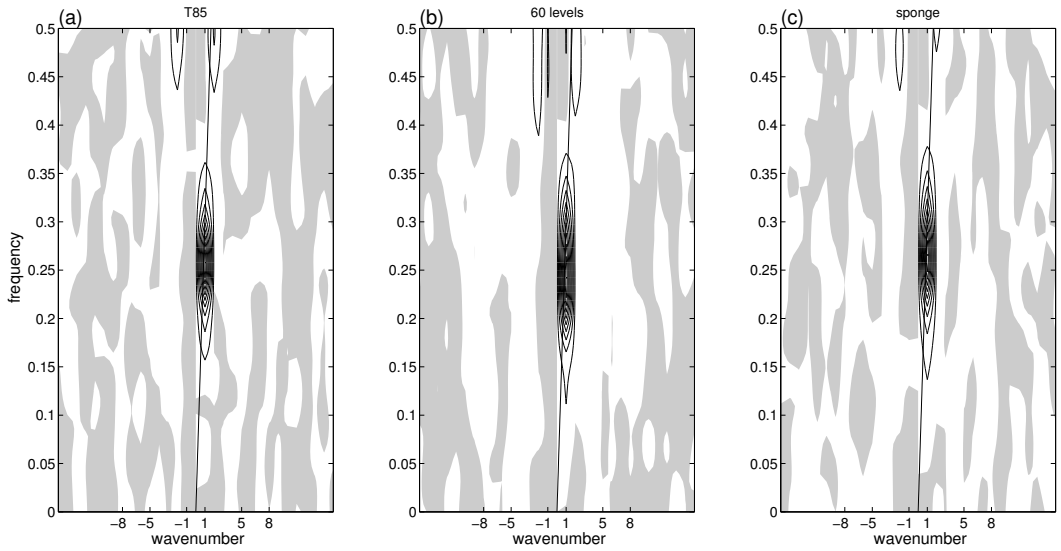


Figure 2.22: $\mathcal{S}$ in $\omega - k$ space at the equator for the $R_o = 0.1$ atmosphere and various integration configurations. Solid line shows the $H = 40$ Kelvin wave dispersion relation. Shaded values negative. Contour intervals arbitrary. (a) T85 horizontal resolution at 475 mb. Decomposition of 1.9 m/s/day acceleration. (b) 60 unevenly spaced vertical levels at 440 mb. Decomposition of 2.1 m/s/day acceleration. (c) Top-of-atmosphere eddy damping sponge at 475 mb. Decomposition of 1.7 m/s/day acceleration.

Our parameter sweep results correspond with what is known of terrestrial planets with large thermal Rossby number atmospheres like Venus and Titan, both of which are superrotating. However it turns out that the superrotation on at least Titan is more subtle than simply having a large thermal Rossby number. Pinto and Mitchell (2014) have shown that the thermal damping timescale also plays an important role and when the overturning circulation is made to be too strong superrotation can be shut down.

We have analyzed the dry dynamical core's tropical variability in an attempt to isolate the mechanism producing the superrotation, in particular by decomposing various fields in spectral space and trying to associate the variability with wave motion. Using the upper tropospheric geopotential height field we found that the control run of the dynamical core has strong Kelvin wave and Rossby-Haurwitz signals. Earth's atmosphere has richer variability, with strong Kelvin wave, equatorial Rossby wave, and MJO activity (focusing only

on symmetric and lower frequency modes). As the thermal Rossby number increases in the model the Kelvin wave response grows stronger and low wavenumbers become dominant.

In particular, we decomposed the equatorial eddy momentum flux convergence ($\mathcal{S}$) in spectral space and found that in the control atmosphere there exists a weak acceleration by eastward eddies (likely low-frequency Kelvin waves) that is overpowered by westward eddies (extratropical Rossby waves and mixed Rossby-gravity waves) decelerating the flow. The eddy activity changes as the thermal Rossby number increases and now equatorial eddies, with a Kelvin-wave signature, strongly accelerate the equatorial zonal winds. Kelvin wave meridional momentum transport was shown to exist at other intermediate thermal Rossby numbers and Kelvin wave meridional momentum transport is also present in the superrotating cases of Williams (2003), despite the very different configuration.

Interestingly, Earth's atmosphere is also found to have strong eddy acceleration at the equator that corresponds to both the wavenumber-1 component of the MJO and low wavenumber Kelvin waves. The fact that superrotation does not occur in the Earth's atmosphere is due to the presence of a seasonal cycle (with westward momentum brought to the equator by the Hadley Cell) and to a lesser extent the decelerating effects of Rossby wave breaking (Lee, 1999). More generally a strong seasonal cycle does not necessarily suppress superrotation if the overturning circulation is sufficiently weak and the thermal damping time becomes another key parameter controlling superrotation (Mitchell et al., 2014). Titan, for example, has both a strong seasonal cycle and strong superrotation.

We believe that the Kelvin wave mechanism discussed here provides a more robust explanation for dry dynamical core superrotation than the hypothesis of barotropic instability as discussed in MV10 and Williams (2003). As mentioned in the introduction barotropic instability cannot bring eddy fluxes directly to the equator, since $\beta - u_{yy}$ cannot change sign there when the north and south hemispheres are symmetric. The Kelvin-wave mechanism

allows for meridional eddy acceleration to be centered on the equator, a structure that can be seen in all of our superrotating runs (not shown).

One thing missing from our discussion is the source of the equatorial Kelvin waves that we see in the dry model. Figure 2.17 suggests that the equatorial Kelvin wave cannot be considered separately from the extratropical Rossby wave.

Chapter 3

Reflection of barotropic Rossby waves in sheared flow and validity of the WKB approximation

This chapter is a reproduction of Potter et al. (2013).

3.1 Introduction

The Wentzel-Kramers-Brillouin (WKB) method is an approximation useful for studying wave transmission through inhomogeneous but slowly varying media. It has proven to be very useful for understanding the propagation of atmospheric Rossby waves. Hoskins and Karoly (1981) used the WKB approximation to study the meridional propagation of barotropic Rossby waves in zonally symmetric flows and Karoly and Hoskins (1982) used the approximation to study the vertical propagation of planetary waves. The WKB approximation allows us to speak of a local dispersion relation and, in particular, a stationary Rossby wavenumber, concepts that are used continually in discussion of stationary wave-trains in models and observations.

In the WKB approximation, a Rossby wave is deformed or refracted as it passes through the inhomogeneous mean flow, but reflections are assumed small. Given the central role played by the WKB approximation, we believe that it is useful to quantify the amount of reflection that does in fact occur under conditions in which this approximation is traditionally applied.

Previous studies in the literature on linear Rossby wave propagation have examined the wave reflection and the breakdown of WKB in the presence of Rossby wave critical layers, focusing on the link between instability and overreflection (e.g. Lindzen and Tung, 1978; Halevy and Peltier, 1985). The questions we address are simpler. We are concerned with estimating the reflection in typical problems in which WKB is invoked, away from critical latitudes. We address these questions by examining idealized cases of barotropic propagation in detail.

As an application, we study wave reflection in the East Pacific window (EPW) region. Past studies have suggested that the upper level westerlies in the Eastern Pacific may provide a pathway for interhemispheric interaction, (Webster and Holton, 1982; Hoskins and Ambrizzi, 1993). We investigate the degree of reflection and transmissivity in this region to evaluate the ease with which linear Rossby waves may be propagating through the window region.

3.2 Meridional Wave Propagation

For this study we restrict our attention to the simplest case of meridional Rossby wave propagation. We start with the non-divergent barotropic vorticity equation in Cartesian coordinates linearized about a zonally symmetric shear flow $\bar{u}$ (e.g. Vallis, 2006)

$$\frac{\partial \nabla^2 \psi}{\partial t} + \bar{u}\frac{\partial \nabla^2 \psi}{\partial x} + (\beta - \bar{u}_{yy})\frac{\partial \psi}{\partial x} = 0 \tag{3.1}$$

where ψ is a streamfunction and $\beta = df/dy$, a constant. We look for steady solutions of the form

$$\tilde{\psi} = \mathsf{Re}\{\psi(y)\exp[ik(x-ct)]\}, \tag{3.2}$$

where k is the zonal wavenumber and c is the eastward phase speed, resulting in an equation of the form

$$\psi_{yy} + V(y)\psi = 0 \tag{3.3}$$

with

$$V(y) \equiv \frac{\beta - \bar{u}_{yy}}{\bar{u} - c} - k^2. \tag{3.4}$$

We recall that the spherical equivalent of (3.3) reduces to this Cartesian version when expressed in Mercator coordinates (Hoskins and Karoly, 1981).

We restrict $\bar{u}$ such that it becomes constant at $\pm\infty$, where we also apply the boundary conditions for ψ. We will also require that $\bar{u} \neq c$ throughout the profile. For $\bar{u}$ approaching a constant at $\pm\infty$ the solutions to (3.3) are meridionally propagating plane waves and the boundary conditions at $\pm\infty$ can be enforced as

$$\psi^- = e^{i\ell^- y} + Re^{-i\ell^- y} \tag{3.5}$$

$$\psi^+ = Te^{i\ell^+ y}. \tag{3.6}$$

ψ^+ and ψ^- are the streamfunctions near + and − infinity, respectively and,

$$\ell^- = \sqrt{\frac{\beta}{\bar{u}_{-\infty} - c} - k^2} \tag{3.7}$$

$$\ell^+ = \sqrt{\frac{\beta}{\bar{u}_{+\infty} - c} - k^2} \tag{3.8}$$

are the meridional wavenumbers for $y \to -\infty$ and $+\infty$, respectively. $\bar{u}_{\pm\infty}$ are the asymptotic values of $\bar{u}$ at $\pm\infty$. R is the reflection coefficient and T is the transmission coefficient. We think of the wave as incident from the south. There is no equatorward component for $y \to +\infty$, defining our scattering problem. As the momentum flux must be uniform in y in the solution, the reflection and transmission coefficients are related by

$$\ell^-(1 - |R|^2) = \ell^+|T|^2. \tag{3.9}$$

The WKB approximation can be obtained by substituting $\psi(y) = \alpha(y) \exp i\xi(y)$ into (3.3) and dropping the term involving the second derivative of α. The result is that $\ell \equiv d\xi(y)/dy$ satisfies the local dispersion relation $\ell = \sqrt{V(y)}$ while $\alpha \propto 1/\sqrt{\ell}$. The condition that this term is, in fact, negligible, is

$$\phi \equiv \frac{1}{\ell^{3/2}} \frac{d^2 \ell^{-1/2}}{dy^2} << 1. \tag{3.10}$$

In general the WKB solution consists of waves propagating both poleward and equatorward. However if the WKB solution is valid throughout the domain, which requires in particular that there are no turning latitudes at which $\ell = 0$, then the WKB solution to our scattering problem has only a poleward propagating component with no reflected wave:

$$\psi \approx \sqrt{\frac{\ell^-}{l(y)}} \exp\left(i \int_{-\infty}^{y} l(y') \mathrm{d}y' \right). \tag{3.11}$$

In the WKB limit $R = 0$ and $|T|^2 = \ell^-/\ell^+$.

An alternate derivation that is informative when evaluating the potential for significant reflection consists of approximating the potential $V(y)$ as a series of layers within each of which V is a constant, as pictured in Fig. 3.1. For a poleward propagating wave incident on one interface, at which there is a small jump in V, and a corresponding small jump $\delta\ell$, the ratio of the amplitude of the transmitted wave to the incident wave is $1 - \delta\ell/(2\ell)$ while the amplitude of the reflected component is $\delta\ell/(2\ell)$. If one ignores the reflected wave and tracks the primary transmitted wave through the stratified medium, one rederives the WKB wavefunction with $\alpha\ell^2$ constant in y. One is effectively ignoring the contribution to the transmitted component of the re-reflection of the reflected components. By focusing instead on the reflection, and continuing to ignore multiple refections, we can accumulate the reflected waves to obtain the lowest order approximation to the reflected component. The result, as discussed in Yeh and Liu (1972), is

$$R \approx -\frac{1}{2}\int_{-\infty}^{+\infty} \frac{1}{l}\frac{dl}{dy} e^{2i\int_{-\infty}^{y} l(\tau)d\tau} dy. \tag{3.12}$$

We will refer to this as the once-reflected approximation to the reflection coefficient R.

3.3 Methods

Equation (3.3) is non-dimensionalized with $1/k$ as the length scale and k/β as the timescale. The non-dimensionalized (hatted) terms are $\hat{y} = ky$, $\hat{u} = (k^2\bar{u})/\beta$, and $\hat{c} = (k^2 c)/\beta$. The hats are now dropped and it is assumed that quantities are nondimensional. We look at two different wind profiles, both controlled by the same width and strength parameters

$$\bar{u} = \frac{1}{2}u^*(\tanh(\alpha y) + 1) \tag{3.13}$$

$$\bar{u} = u^* \mathrm{sech}^2(\alpha y). \tag{3.14}$$

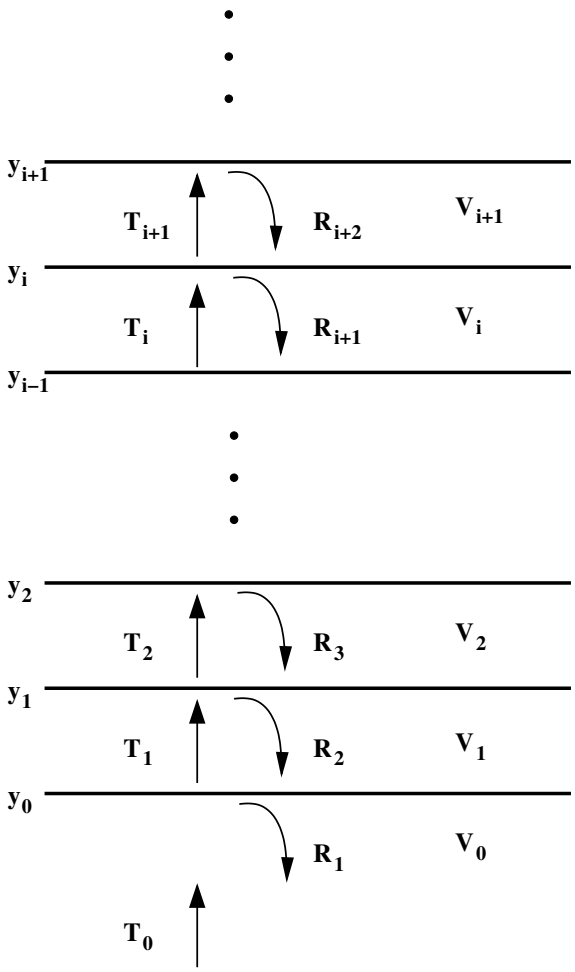


Figure 3.1: Schematic for the 'no reflection' proof of the WKB approximation. The incoming plane wave T_0 hits the shear layer at y_0 and is split into a transmitted component T_1 and a reflected component R_1. The WKB approximation tracks the transmitted wave while ignoring reflections. The once-reflected approximation to the reflection coefficient gathers all of the R_i by transmitting each once-reflected wave southward to $-\infty$ using the WKB approximation. Adapted from Yeh and Liu (1972).

u^* is the maximum velocity attained and $1/\alpha$ is the half-width of the shear zone (large α implies a narrow shear zone). These profiles will be referred to as the tanh and sech^2 profiles. After nondimensionalizing, u^*, α and c are varied while the nondimensional β and k are kept fixed at 1.

For our numerical solutions we solve equation (3.3) by discretizing in y, then solving for the solution vector by Gaussian elimination. The upper boundary condition (3.6) is enforced with

$$\frac{\partial \psi}{\partial y} = i\ell^+ \psi. \tag{3.15}$$

The lower boundary condition (3.5) is enforced by taking the derivative of ψ and adding $i\ell^-\psi$ to eliminate R

$$\frac{\partial \psi}{\partial y} + i\ell^- \psi = 2i\ell^- e^{i\ell^- y}. \tag{3.16}$$

After discretizing the boundary conditions the equation is a matrix equation of the form $A\vec{\psi} = \vec{b}$. Once ψ has been solved, the reflection coefficient is calculated at the lower boundary,

$$|R| = |\psi(y_1)e^{i\ell^- y_1} - e^{2i\ell^- y_1}| \tag{3.17}$$

where $y_1 = -15$, the lowermost value of y, is the numerical equivalent of $-\infty$.

3.4 The tanh profile

We start with the tanh profile, which is frequently used in studies of reflection (e.g. Lindzen and Tung, 1978; Halevy and Peltier, 1985). Fig. 3.2 shows reflection in (α, u^*) parameter space for (a) $c = -0.9$, (b) $c = -0.5$, and (c) $c = -0.1$. The reflection coefficient $|R|$ equals 1 for $u^* \geq 1 + c$ for any α because the wavenumber at $+\infty$, ℓ^+, is zero or imaginary. As the

resulting evanescent region is of infinite extent there is no tunneling, and reflection is perfect when ℓ^+ is zero or imaginary.

Overlaid on the reflection in Fig. 3.2 is a heavy solid contour denoting the regime boundary of flows that satisfy the necessary but not sufficient Rayleigh criterion for barotropic instability. All profiles within the area bounded by $\alpha = 0$ and the heavy solid line are stable while all profiles outside of this area are potentially unstable. A flow that is excessively unstable would not be expected to be maintained in the time mean, but it can be useful to consider this scattering problem in the unstable regime to help interpret the overall behavior of the reflection coefficient in this parameter space. Also overlaid is the regime boundary of flows and wave parameters which do and do not possess turning latitudes. All profiles within the area bounded by $\alpha = 0$ and the dashed line have $l > 0$ everywhere. WKB is at least potentially applicable for these profiles.

An informative limit is that of large α, which is strongly unstable but analytically tractable; the reflection becomes a function of u^* only as the profile becomes a 'jump': $\bar{u} = 0$ for $y < 0$ and $\bar{u} = u^*$ for $y > 0$. An infinitely sharp jump profile does not imply total reflection, despite the refractive index ℓ^2 going to $-\infty$. We use matching conditions in displacement and pressure to solve for ψ. Following Vallis (2006) the vorticity equation can be rewritten as

$$[(\bar{u} - c)\psi_y - \bar{u}_y\psi]_y + [\beta - k^2(\bar{u} - c)]\psi = 0. \tag{3.18}$$

Integrating this equation across the interface at $y = 0$ gives the first matching condition,

$$0 = \Delta[(\bar{u} - c)\psi_y - \bar{u}_y\psi] \tag{3.19}$$

where Δ denotes the difference in the bracketed quantity across the interface. The second matching condition can be found by making the substitution $\eta = \frac{\psi}{\bar{u}-c}$ into the vorticity

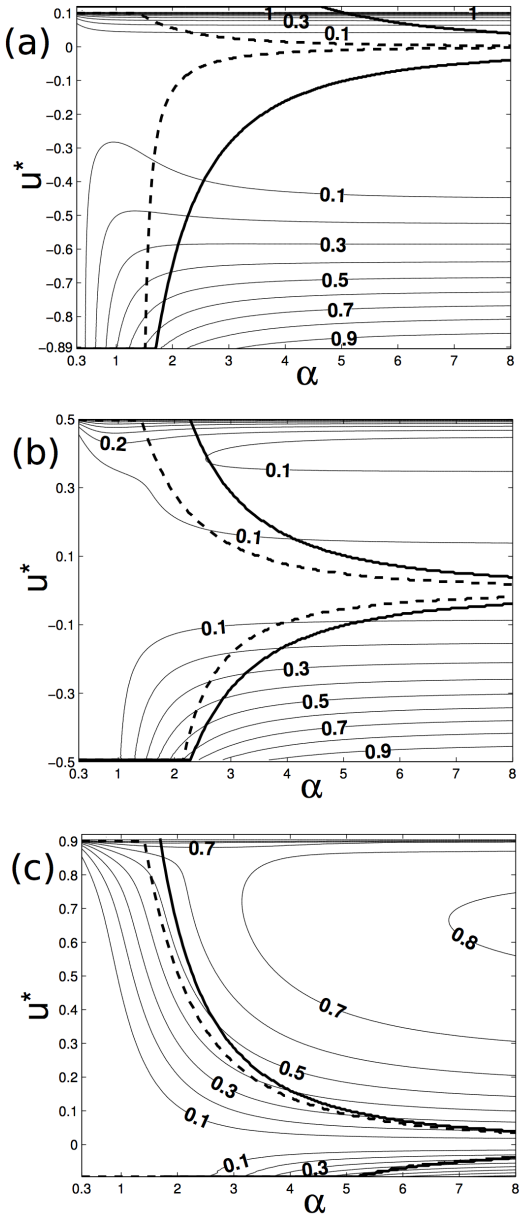


Figure 3.2: Contours of $|R|$ solved for numerically with the tanh profile for (a) $c = -0.9$, (b) $c = -0.5$, and (c) $c = -0.1$. Contour spacing is 0.1. No turning latitudes exist in the region bounded by the heavy dashed line and $\alpha = 0$. The Rayleigh instability criterion is not satisfied in the region bounded by the heavy solid line and $\alpha = 0$.

equation. This gives

$$(\eta(\bar{u}-c))_{yy} - u_{yy}\eta + (\beta - k^2(\bar{u}-c))\eta = 0. \tag{3.20}$$

Integrating twice across the interface at $y = 0$, yields

$$\Delta\eta = \Delta\left[\frac{\psi}{\bar{u}-c}\right] = 0. \tag{3.21}$$

The reflection coefficient is then solved for by using the plane wave form of ψ from the boundary conditions (3.5) and inserting them into the matching conditions (3.19) and (3.21) to obtain

$$R = \frac{c^2\ell^- - (u^*-c)^2\ell^+}{c^2\ell^- + (u^*-c)^2\ell^+}. \tag{3.22}$$

The reflection coefficient for this limit is plotted in Fig. 3.3. The reflection is not a monotonic function of u^*. There is a zero in reflection near $u^* = -0.35$ for $c = -0.9$ and near 0.4 for $c = -0.5$, for example, in addition to the trivial zero at $u^* = 0$. This is an example of a reflectionless potential (e.g. Kay and Moses, 1956). The wave interference for the reflectionless potential is such that transmission is perfect despite the wave propagating through a varying medium. Reflectionless potentials have been studied intensively due to their connection to soliton theory by way of the inverse scattering transform.

There is a hint in the reflection results for different values of c that the reflectionless potentials obtained analytically for this jump profile still make themselves felt in the more physically relevant region of parameter space, producing broad minima in the reflection as a function of u^* in scattering problems that have no turning latitudes. In any case, the existence of these reflectionless potentials reminds us that approximate theories for reflection throughout this parameter space will be difficult to achieve.

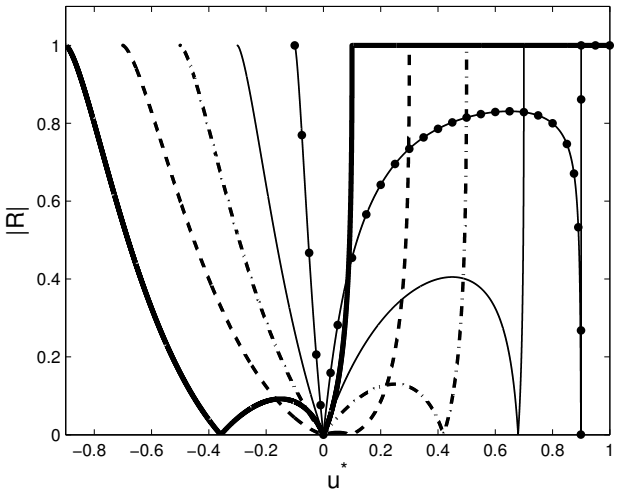


Figure 3.3: $|R|$ in the limit $\alpha \to \infty$ for, from left to right, $c = -0.9$ (heavy solid), -0.7 (dashed), -0.5 (dash-dotted), -0.3 (thin solid), -0.1 (thin solid with dots). There is a second zero for $c = -0.7$ at $u^* = 0.1$ that is not well resolved in this figure.

We determine the accuracy of the WKB approximation by plotting the percent relative error of the WKB approximated transmission coefficient versus the numerical solution, for the case with $c = -0.9$, in Fig. 3.5. Due to the relation between reflection and transmission this figure shares similarities with Fig. 3.2a, but we include it here to provide more detail. For comparison, the profile maximum of the WKB validity parameter ϕ as defined in Equation (3.10) is plotted in figure 3.4. WKB does an excellent job approximating $|T|$ despite $\phi \gg 1$ in a large part of the parameter space. Errors of less than ten percent exist in regions of parameter space in which the values of $\phi \sim 10^2$ are reached in the domain.

We have computed the once-reflected approximation for $|R|$ for the case $c = -0.9$. Plotted in Fig. 3.6 is the absolute error in this once-reflected approximation for $|R|$. In the tanh profile, the approximation does quite well for a large swath of the parameter space, approximating reflection coefficients of the order 0.1-0.3 with errors less than ten percent. It would be useful to be able to place an upper bound on the reflection, based on this once-reflected

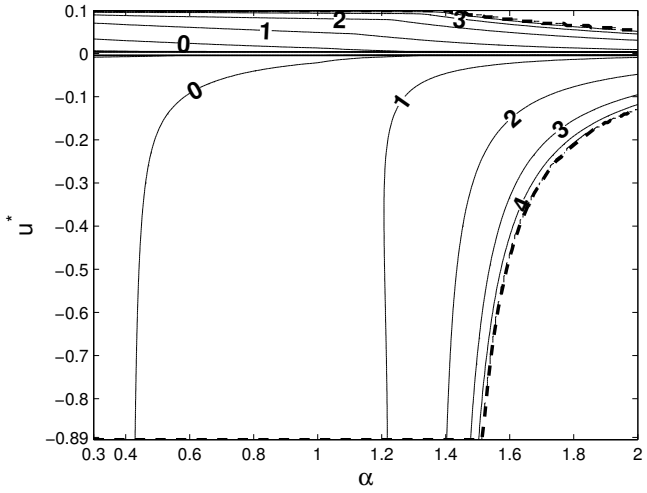


Figure 3.4: Base ten logarithm contours of the profile maximum of ϕ in the tanh profile with $c = -0.9$. Contours placed at powers of ten. No turning latitudes exist in the region bounded by the dashed line and $\alpha = 0$.

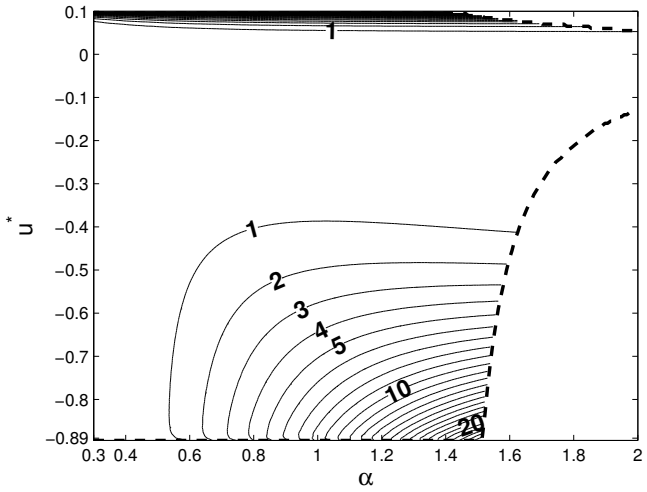


Figure 3.5: Contours of percent relative error for the WKB approximated transmission coefficient in the tanh profile with $c = -0.9$. Contour spacing is one percent error. No turning latitudes exist in the region bounded by the dashed line and $\alpha = 0$.

approximation, but this is difficult due to phase cancelations that occur in this integral, and we have not found a useful upper bound by this approach.

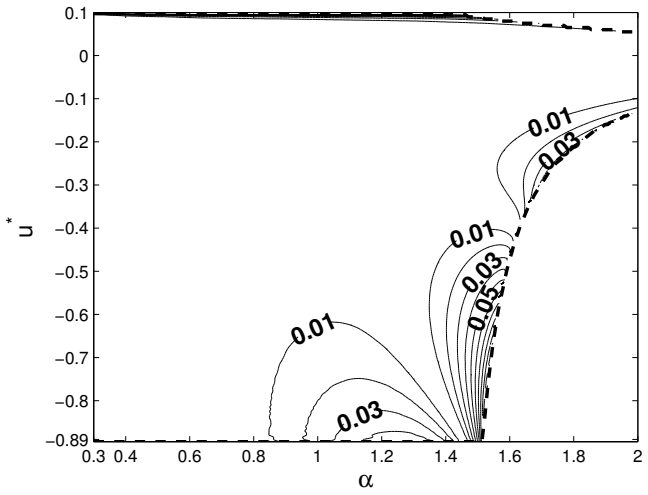


Figure 3.6: Contours of absolute error for the single scatter approximated reflection coefficient in the tanh profile with $c = -0.9$. Contour spacing is 0.01. No turning latitudes exist in the region bounded by the dashed line and $\alpha = 0$.

3.5 The squared hyperbolic secant profile

The primary difference between the tanh and sech^2 profiles is that ℓ^+ in the sech^2 profile is always such as to accomodate a wave propagating to $+\infty$, unlike the tanh profile for $u^* \geq 1 + c$, which implied total reflection. The numerical solution for $|R|$ in the sech^2 profile is shown in Fig. 3.7 for (a) $c = -0.9$, (b) $c = -0.5$, and (c) $c = -0.1$. As waves can always propagate at $+\infty$, the structure of $|R|$ is a more complicated function of u^* and α. A line of nontrivial zero reflection again exists for all three values of c, leading to a local maximum in reflection. Like the tanh profile in Fig. 3.3 this is another example of a reflectionless potential. An interesting part of this figure that we would like to point out is the ability of barotropic Rossby waves to retain significant energy despite having to tunnel through significant evanescence regions. Looking at, e.g., Fig. 3.7b, for $(\alpha, u^*) \sim (1.5, 0.9)$ the profile is well away from the WKB-applicable region but the wave transmits nearly half of its energy to $+\infty$. Despite the WKB approximation saying the wave should be completely reflected, significant wave energy is actually being transmitted.

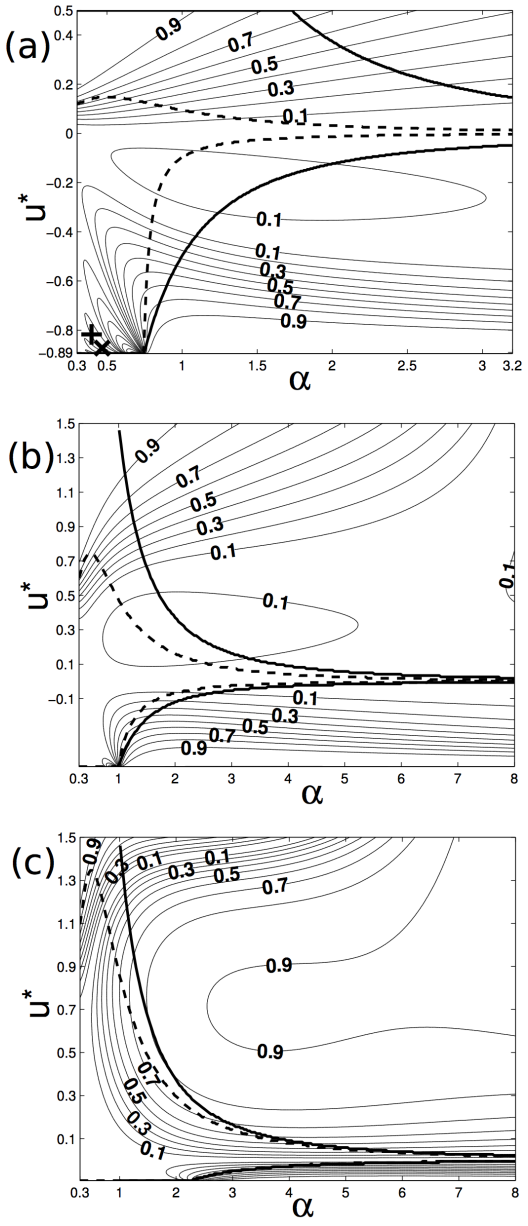


Figure 3.7: Contours of $|R|$ solved for numerically with the sech^2 profile for (a) $c = -0.9$, (b) $c = -0.5$, and (c) $c = -0.1$. Contour spacing is 0.1. No turning latitudes exist in the region bounded by the dashed line and $\alpha = 0$. The Rayleigh instability criterion is not satisfied in the region bounded by the solid line and $\alpha = 0$. In the $c = -0.9$ figure the X (MAM) and + (DJF) indicate where the seasonal EPW lies in parameter space.

As for the tanh profile, we use the $c = -0.9$ case to evaluate the WKB approximation. WKB does an excellent job approximating $|T|$. From Fig. 3.10 it can be seen that the transmission coefficient is approximated with less than ten percent error throughout the bulk of the domain. WKB is accurate despite ϕ reaching values larger than order one throughout most of the parameter space (Fig. 3.9). The once-reflected approximation does not do as well in the sech^2 profile (Fig. 3.8). The approximation has difficulty near the boundary of the WKB-applicable region as well as near the boundary where $\bar{u}$ approaches c.

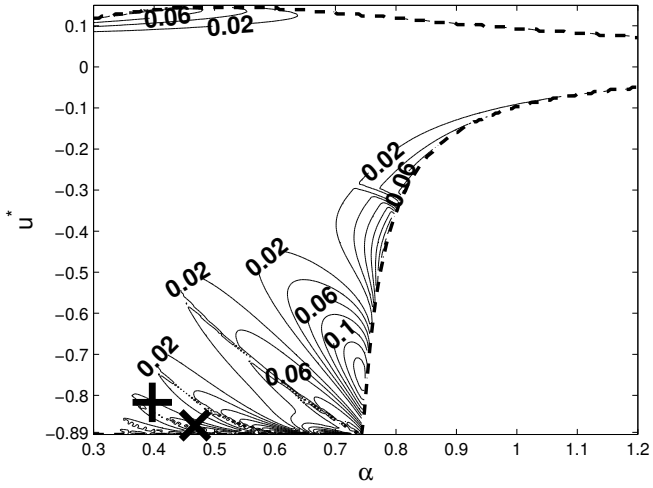


Figure 3.8: Contours of absolute error for the WKB approximated transmission coefficient in the tanh profile with $c = -0.9$. Contour spacing is 0.02. No turning latitudes exist in the region bounded by the dashed line and $\alpha = 0$. The X (MAM) and + (DJF) indicate where the seasonal EPW lies in parameter space.

3.6 An application to the East Pacific window region

Zonal winds at the 300 mb level are taken from years 1989-2010 in the ERA-Interim data set using seasonal mean winds averaged between 90W and 180W degrees longitude. At least for this dataset there are only seasonal mean westerlies during northern hemisphere winter (DJF) and spring (MAM), so we focus on these two seasons. To study this problem

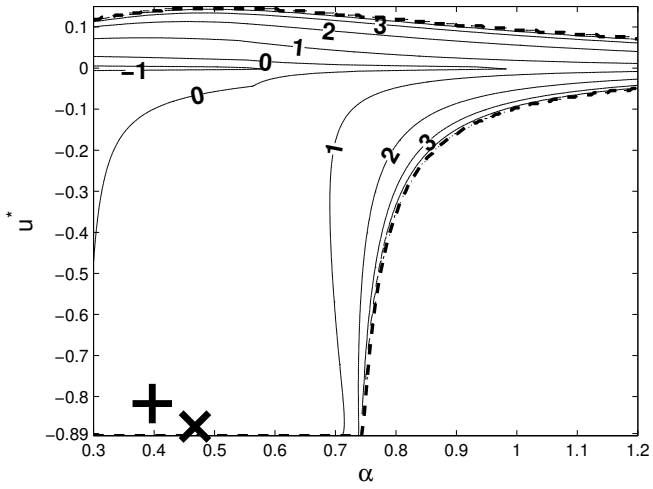


Figure 3.9: Base ten logarithm contours of the profile maximum of ϕ in the sech^2 profile with $c = -0.9$. Contours placed at powers of ten. No turning latitudes exist in the region bounded by the dashed line and $\alpha = 0$. The X (MAM) and + (DJF) indicate where the seasonal EPW lies in parameter space.

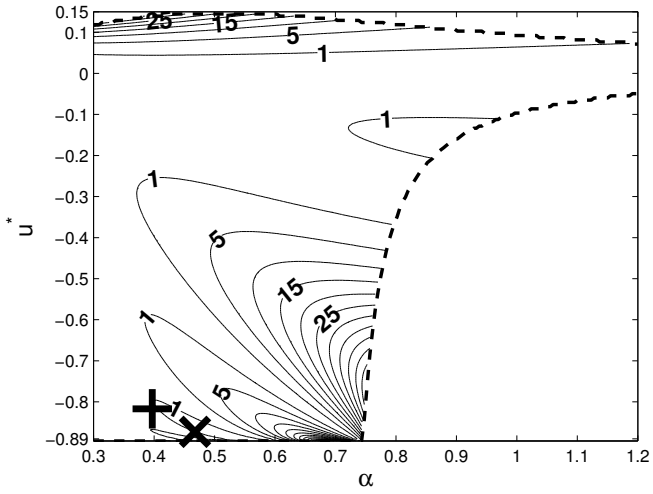


Figure 3.10: Contours of percent relative error for the WKB approximated transmission coefficient in the sech^2 profile with $c = -0.9$. Contours are placed at 1 percent and multiples of 5 percent error. No turning latitudes exist in the region bounded by the dashed line and $\alpha = 0$. The X (MAM) and + (DJF) indicate where the seasonal EPW lies in parameter space.

using the same methods as before, the spherical linearized barotropic vorticity equation is transformed to the Cartesian equivalent using Mercator coordinates, following Hoskins and Karoly (1981). After the Mercator transform, the spherical vorticity equation is identical to Equation 3.3. We choose zonal wavenumber 4 ($k = 4/a$, where a is the radius of the Earth). This can be considered as a maximum size that could propagate through the EPW, though modest changes to either the size of our EPW definition or the zonal wavenumber do not qualitatively change our results. We nondimensionalize using β at the equator and k and consider a stationary wave (c=0).

Once the observed winds are converted to Mercator coordinates and non-dimensionalized we fit them with an idealized profile of the form

$$\bar{u}_{\mathrm{EPW}} = u^* \mathrm{sech}^2(\alpha y) + u_0. \tag{3.23}$$

to mimic mid-latitude to mid-latitude interaction across the equator. Though the climatological seasonal mean minimum in the window westerlies does not occur precisely at the equator in this dataset, we assume so for simplicity of the idealized profile. The constant u_0 is chosen to fit one of the subtropical jet maxima (we choose the weaker jet maximum). In the real world the waves we are concerned with will be generated at midlatitudes. To simplify the construction of the scattering problem, we choose a non-dimensional wind profile that asympotes to the non-dimensional jet maximum u_0, thereby forcing the meridional wavenumber at $-\infty$ to mirror the meridional wavenumber of a wave generated near the jet maximum. Once u_0 is chosen u^* is determined as $u^* = \min(\bar{u}_M) - u_0$ where $\min(\bar{u}_M)$ is the minimum of the nondimensional Mercator transformed observed climatological wind $\bar{u}_M$.

The remaining parameter α is chosen to minimize the squared error between $\bar{u}_{\mathrm{EPW}}$ and $\bar{u}_M$ between the equator and the latitude of the subtropical jet closest to the equator. As an example, the MAM best fit $\bar{u}_{\mathrm{EPW}}$ is plotted in the lower panel of figure 3.11. The dimensional

form of the fit in the upper panel of figure 3.11 shows that $\bar{u}_{\mathrm{EPW}}$ is roughly capturing the equator-jet-pole structure of the zonal wind.

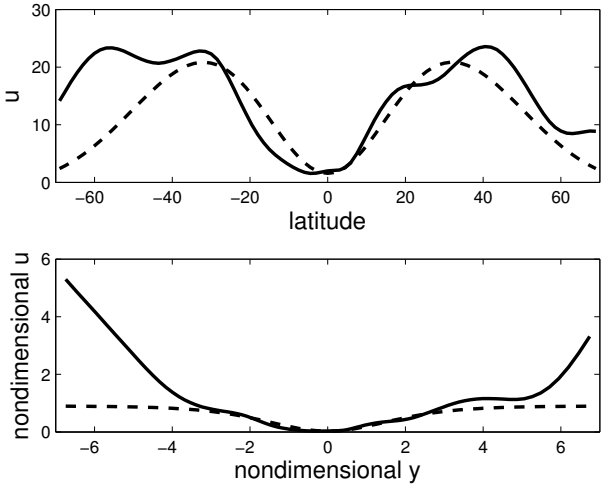


Figure 3.11: Upper panel: the MAM dimensional $\bar{u}_{\mathrm{EPW}}$ (dashed) plotted with the MAM 300 mb ERA-interim $\bar{u}$ (solid). Lower panel: MAM $\bar{u}_{\mathrm{EPW}}$ (dashed) plotted with the nondimensional Mercator-transformed MAM 300 mb ERA-interim zonal wind, $\bar{u}_M$ (solid).

We exploit the Galilean invariance of the system, i.e., there is no difference between a given u_0 with $c = 0$ and a given $c = -u_0$. This allows direct comparison of the East Pacific window problem, where $u_0 = 0.9$, to the $c = -0.9$ sech^2 plots in figures 3.7(a), 3.10, 3.9 and 3.8. As can be seen, the real-world winds seem to lie well within the regime where WKB applies: the WKB validity condition is between order zero and one and WKB approximates the transmission coefficient with 1-2 percent error.

This seemingly low reflection may be misleading. In Fig. 3.12 we visualize reflection in the EPW as a function of $u_{\min}$, the minimum of $\bar{u}_{\mathrm{EPW}}$. Since $u^* < 0$, equation (3.23) gives $u_{\min} = u^* + u_0$ at $y = 0$. Figure 3.12 is a cross section of Fig. 3.7a for α fixed at the best fit MAM value. $u_{\min}$ runs from just above $u_{\min} = 0$, where reflection quickly becomes total, and $u_{\min} = 0.9$, where reflection is zero. Changing the wind minimum from 0.1 to 0.17 is sufficient to raise the reflection coefficient to 0.3, due to altered constructive or destructive

interference of the weakly reflected waves. While these reflections are subtle, they indicate that modest reflections back into midlatitudes are possible in the absence of (nonlinear) critical layers or turning points. In addition this result may be altered by nonlinearity (see, for example, Fyfe and Held, 1990), as waves can be expected to break in the region of the wind minimum if of sufficient amplitude, even if the linear theory shows minimal reflection.

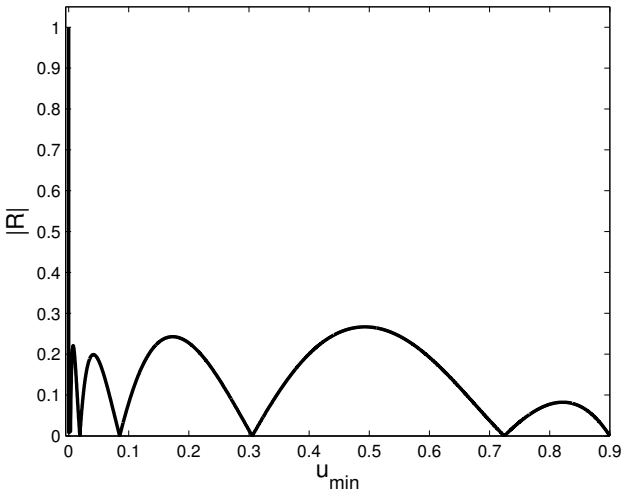


Figure 3.12: $|R|$ in the idealized EPW as a function of minimum nondimensional westerlies. $u_{\min} = 0$ is the stationary wave critical latitude and on the right $u_{\min} = 0.9$ implies $u^* = 0$, a constant wind profile.

3.7 Conclusions

We have presented numerical and analytical solutions for the reflection coefficient of a barotropic Rossby wave in the linearized barotropic vorticity equation. We have compared the full numerical solution to approximations for both the transmission coefficient (WKB approximation) and the reflection coefficient (once-scattered approximation). Lastly we applied our ideas to a climatological flow by studying wave transmission through the East Pacific window region.

If we assume that real-world zonal wind profiles averaged over long enough time and length scales will not satisfy the Rayleigh criterion for barotropic instability our results suggest that the WKB approximation is very accurate when approximating wave transmission in climatological flows. In the profiles without turning points the magnitude of the reflection coefficient appears to be a good proxy for the validity of WKB. The reflection coefficient, in turn, is decently approximated by the single-scattering approximation and the approximated reflection coefficient provides a metric by which to evaluate the validity of the WKB approximation for a given zonal wind profile. Despite doing a good job throughout most of the domain, the WKB approximation can completely neglects significant transmission. It is easy to find regions of (α, u^*) parameter space in the sech^2 profile where WKB can not apply but 0.1-0.9 of a wave is being transmitted to $+\infty$. This suggests that significant Rossby wave energy may be able to tunnel through evanescent regions and have an appreciable impact on the atmosphere. We return to this idea in Ch. 4.

On the flip side, our analytical results for the jump profile show that it is possible for wave transmission to be perfect even in parameter regimes with turning points. Even our idealized East Pacific window model exhibits reflectionless potentials, though it is unclear if this phenomenon could manifest itself in the real world.

Our application to the East Pacific window suggests that the region can be quite transparent to stationary Rossby waves. However, at least within our idealized setup, significant reflection on the order of 30% can occur with small changes in the zonal winds. Therefore, the WKB approximation should be applied with caution when discussing Rossby wave propagation into the Tropics as significant reflection can occur even in the absence of a turning point. These results assume the relevance of the non-divergent barotropic model. While this assumption seems fine for the deep tropics, the sub-tropics, where a Rossby wave would encounter low level easterlies, may give rise to more complex behavior.

It would be of interest to perform calculations similar to those done here for vertically propagating Rossby waves in vertical shear so as to analyze more closely models of troposphere-stratosphere interactions in the style of Holton and Mass (1976). In that setup the waves would be generated at the surface in midlatitudes while propagating vertically into the stratosphere whereas our EPW application tracked waves generated in midlatitudes as they propagated meridionally into the tropics.

Chapter 4

Some sufficient conditions for dynamically active equatorial modes

4.1 Tropical and extratropical variability in spectral space

Several modeling and observational studies have shown the importance of the extratropics in the excitation of tropical variability. Using tropical OLR data as a measure of convection and midlatitude 500 mb geopotential height as a measure of extratropical variability Liebmann and Hartmann (1984) showed that intraseasonal tropical variability is strongly correlated with midlatitude variability that occurred days before. In another observational study Straub and Kiladis (2003a) showed that Pacific Kelvin wave activity during austral winter can be directly tied to an extratropical Rossby wave train propagating into the tropics. Lastly, Lin et al. (2000) used an idealized AGCM in which midlatitude eddies generated by baroclinic instability could be shut off to show that when midlatitudes eddies no longer exist tropical intraseasonal variability disappears.

Idealized modeling studies have also shown that extratropical forcing directly projects onto tropical modes. Zhang and Webster (1992) and Zhang (1993) used a linearized β-plane shallow water model to show that off equatorial forcing (in their case, a heating) excites equatorial Rossby, mixed Rossby-gravity, or Kelvin modes depending on the frequency matching of the extratropical forcing and the natural frequency of the equatorial wave. Doppler shifting is shown to have a large effect on the magnitude of the response with the mixed Rossby and equatorial Rossby waves' response being stronger in mean westerlies and the Kelvin wave response being larger in mean easterlies. Hoskins and Yang (2000) extended these results by performing similar model runs in a global sigma-coordinate primitive equations model. They showed that the results of Zhang and Webster (1992) and Zhang (1993) still applied in their more complex model with either heating or vorticity forcing in the extratropics. A robust tropical response was found even when the extratropical forcing was as far poleward as 60°.

Using OLR as a proxy for tropical convection Wheeler and Kiladis (1999) (from hereon WK99) showed that atmospheric variability in Earth's tropical troposphere can in large part be understood in the context of the family of theoretical equatorial β-plane shallow water waves found by Matsuno (1966). To diagnose tropical variability WK99 Fourier transformed tropical variability in longitude and time. Tropical latitudes (equatorwards of 15°) and many time slices are averaged together to form a single wavenumber-frequency climatology of tropical variability. The key part of WK99's analysis is to generate a red background spectral climatology by applying a simple smoother in spectral space. Wave-like variability is then highlighted by dividing the raw spectral climatology by the smoothed background. WK99 showed that much of the tropical atmosphere's variability falls along the theoretical dispersion curves for Kelvin, equatorial Rossby, mixed Rossby-gravity, and inertio-gravity waves. WK99 showed several exceptions to this neat classification, with westward tropical depres-

sions and the eastward Madden-Julien oscillation (the strongest convective intraseasonal tropical signal) not fitting into the family of theoretical equatorial waves.

Mitchell and Vallis (2010) and Potter et al. (2014) showed that even a spectral primitive equations model forced with the highly idealized dry Held-Suarez physics has strong tropical variability. WK99's method applied to the dry dynamical core showed strong Kelvin wave activity. The author's showed that this Kelvin wave signal becomes increasingly dominant as a key nondimensional parameter in the model, the thermal Rossby number $R_o = R\Delta_h/(2\Omega a)^2$, is increased. It was shown that as the Kelvin wave becomes increasingly strong it leads to strong horizontal eddy momentum fluxes that eventually bring the model to strongly superrotate.

In this writeup we wish to demonstrate that a key to *spontaneous* superrotation in dry atmospheric models is the ability of extratropical Rossby waves to excite tropical waves. A hindrance to extratropical excitation and, consequently, superrotation, is the inability for extratropical wave energy (either propagating or evanescent) to reach the tropics and project onto tropical waves. We structure this chapter around the ideas of Hayashi and Young (1987). The authors explored instability on the equatorial β-plane with a background mean flow and found that instability in this system could be understood as an unstable coupling or resonance between stable modes. In their model, these modes were primarily equatorial Kelvin waves and edge waves trapped at the model's boundary front. When the edge waves were Doppler-shifted to have the same frequency as the Kelvin waves, the two modes were able to couple, resonate, and grow. Combining the literature discussed above and Hayashi and Young (1987) we will attempt to understand the superrotation in Mitchell and Vallis (2010), Potter et al. (2014), and Williams (2003) as the result of a coupling between extratropical and tropical waves.

We hope that this work acts as a complement to two more rigorous studies of instability and superrotation. Iga and Matsuda (2005) showed that superrotation in a Venus-like

model arises from the excitation of a Kelvin wave that is excited via lateral coupling to an extratropical Rossby wave. Wang and Mitchell (2014) studied global instabilities of large R_o atmospheres and found that a global Kelvin-Rossby mode became active at sufficiently large R_o. The authors showed that this global mode fluxed momentum towards the equator and caused superrotation.

This chapter is organized as follows. Section 4.2 examines the spectra of the tropics and extratropics in the Earth-like dynamical core. Section 4.3 derives a crude dispersion relation for extratropical variability and compares it to the Matsuno equatorial shallow water waves. Section 4.4 examines how both extratropical and tropical variability change in superrotating atmosphere. Lastly, in section 4.5 we discuss the importance of Rossby wave evanescence in the excitation of equatorial waves.

4.2 Spectral characteristics of the dynamical core

We use the GFDL FMS spectral dynamical core with T42L20 resolution forced by Held-Suarez physics. The control atmosphere climatology is shown in Fig. 2.1.

Fig. 4.1a shows the base ten logarithm of the spectral power of tropical geopotential height at 275 mb as a function of wavenumber and frequency. This plot has no decomposition for symmetric or antisymmetric modes. For eastward wavenumbers there is a clear Kelvin wave signal for an equivalent depth of 40 m. The westward side of the Fig. shows a clear Rossby-Haurwitz mode. There are hints of extratropical power at wavenumber ± 5.

A similar spectral power diagram is shown in Fig. 4.1b but for 275 mb geopotential height at 45°. The primary feature of this midlatitude spectrum is a ridge running straight from roughly eastward wavenumber 5. There is a weaker signal with a similar slope starting from eastward wavenumber 5. There is also a weaker signal for eastward wavenumbers 1-5 starting at the origin, which perhaps corresponds to the equatorial Kelvin wave signal seen in the

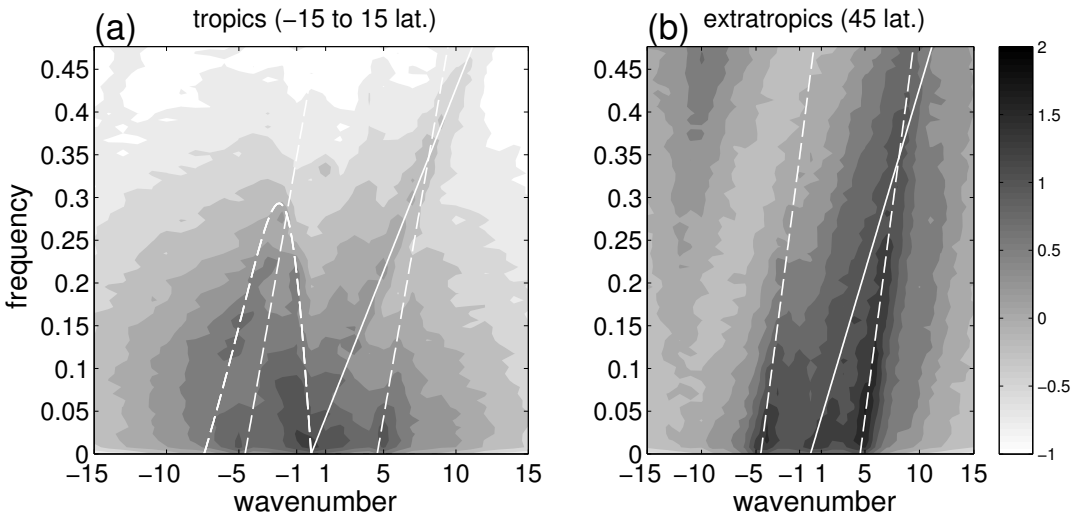


Figure 4.1: Base ten logarithm of the spectral power of the geopotential height field at 275 mb for the control atmosphere. Solid line shows theoretical dispersion relations for Kelvin waves ($k > 0$) with equivalent depth $H = 40$ m. (a) Spectral power between -15 and 15 degrees latitude. Dashed curve shows theoretical dispersion relation for a Rossby-Haurwitz wave with equivalent depth of 15 km Doppler shifted by a 15 m/s wind. (b) Spectral power at 45 degrees latitude. The dashed lines show the approximate Rossby wave dispersion relation, Eq. 4.8, discussed in the text.

tropical spectrum. It is interesting to note that, in contrast to the equatorial spectrum, the strongest signals do not cross through the origin.

These extratropical signals are Rossby waves generated by baroclinic instability, and they can also be seen in studies by Pratt (1977) (Figs. 1 and 2), Lee and Held (1993) (Fig. 4), Hoskins and Yang (2000) (Fig. 2), and Adames et al. (2014) (Fig. 4). In the next section we exploit the clear linear structure in Fig. 4.1b to define a crude dispersion relation.

4.3 An approximate dispersion relation for the extra-tropical Rossby wave signal

We start with equatorial Rossby wave dispersion relation on a barotropic beta-plane:

$$\omega = \overline{u}k - \frac{\beta k}{k^2 + \ell^2}. \tag{4.1}$$

Since the model output suggests a linear dispersion relation we can break our problem into two simple parts: finding the slope, γ, the zero frequency intercept, k_0, and plugging them into $\omega = \gamma(k - k_0)$ to get the new dispersion relation. The intercept can be found by setting $\omega = 0$ and solving for k^2. Since we are viewing things in the $\omega - k$ plane we do not want to consider the meridional wavenumber ℓ. In the Matsuno solution of the shallow water equatorial beta plane, meridional structure is modeled using Hermite polynomials (Matsuno, 1966). Here we are much cruder, and simply take $\ell = k$. To get the intercept we rewrite the stationary wavenumber $k_s = (\beta/\overline{u})^{1/2})$ to get

$$2k_0^2 = \frac{\beta}{\overline{u}_0} = k_s^2 \tag{4.2}$$

$$\frac{2k_0^{*2}}{a^2\cos^2\phi} = \frac{2\Omega/a\cos\phi}{\overline{u}_0} \tag{4.3}$$

$$k_0^* = \pm\left(\frac{2\Omega a\cos^3\phi}{2\overline{u}_0}\right)^{1/2} \tag{4.4}$$

where k^* is the number of waves that fit around a latitude circle, a quantity conserved in latitude (e.g. Randel and Held, 1991). k^* is the quantity on the x-axis of Fig. 4.1. $\overline{u}_0$ is the zonal mean zonal wind at the relevant latitudes and pressure levels, as discussed below.

The slope of the line is found either empirically, by calculating the slope from the line in Fig. 4.1b, or, as it turns out, by neglecting the second term on the righthand side of Eq. (4.1)

$$\gamma = \partial\omega/\partial k \approx \overline{u}_0. \tag{4.5}$$

With the slope and the intercept the complete dispersion relation is

$$\omega = \overline{u}_0 \left(k \pm \frac{\sqrt{2}}{2} k_s \right) \tag{4.6}$$

It turns out that this is almost, but not quite, correct. Using Fig. 4.1 as a guide, a correction factor of 2 is required to obtain the correct zero-frequency intercept:

$$\omega = \overline{u}_0 \left(k \pm \sqrt{2} \left(\frac{2\Omega/a\cos\phi}{\overline{u}_0} \right)^{1/2} \right) \tag{4.7}$$

$$\omega = \frac{\overline{u}_0}{a\cos\phi} \left(k^* \pm \sqrt{2} \left(\frac{2\Omega a \cos^3\phi}{\overline{u}_0} \right)^{1/2} \right) \tag{4.8}$$

This correction factor is not needed at all if, instead of assuming $\ell = k$ to obtain the intercept, the meridional wavenumber is taken as $\ell = -i\sqrt{2}/2k$. This would imply that the Rossby waves are evanescing rather than propagating over a distance somewhat larger than the zonal wavelength. Regardless of whether the correction factor can be justified with an improved derivation, the dispersion relation appears to work quite well. Eq. 4.8 is plotted in Fig. 4.1, overlying the logarithm of the spectral power of extratropical geopotential height. The dispersion relation clearly captures the peaks of spectral power starting from $k^* = \pm 5$. The eastward ($k^* > 0$) component is dominant. We note that while the dispersion relation clearly captures the peaks of the spectral power, there is non-negligible power 2-3 wavenumbers away from the peak.

To obtain the correct $\overline{u}_0$ and latitude, ϕ, for Eq. 4.8 we use the following recipe. First, the latitude ϕ is diagnosed by looking for the latitude (or latitudes) where surface zonal

winds reach their peak. This is meant to find the center of the storm track where Rossby waves are generated. In the dynamical core which has no real 'surface' we use the lowest pressure level. Second, the mean wind $\overline{u}_0$ is diagnosed by finding the pressure level(s) at the latitude ϕ described above where eddy activity is maximal. Here, this level was diagnosed by both eddy kinetic energy and horizontal eddy momentum divergence, $\mathcal{S}$, which give the same pressure level. The relevant $\overline{u}_0$ is then calculated by averaging the zonal mean zonal wind at the latitude(s) and pressure level(s) diagnosed above. Lastly, for plotting purposes, ω is converted from radians per second to cycles per day by multiplying by $86400/(2\pi)$.

It is interesting to note that the relevant circulation-dependent parameters ϕ and $\overline{u}_0$ can be calculated from climatologies. Though we use eddy quantities to diagnose the correct pressure levels, even this eddy calculation can be neglected by using, for example, the pressure level of maximum zonal wind. This is a large contrast to diagnosing the equivalent depths relevant to equatorial waves in a moist atmosphere. Moist convection *locally* modifies the equivalent depths that equatorial waves see and, consequently, the relevant equivalent depths cannot be diagnosed from mean climatologies and must be backed out of spectral diagnostics (Wheeler and Kiladis, 1999; Kiladis et al., 2009).

Using the recipe described above we demonstrate the flexibility of the approximate dispersion relation Eq. 4.8 in Figs. 4.2 and 4.3. Fig. 4.2 is a diagram of spectral power for the tropics and extratropics of the $a = 9e5$ m atmosphere. The tropics are dominated by an $H = 40$ Kelvin wave signal. The $k^* < 0$ signal is aliased Kelvin wave variability, and the only signal that does not clearly associate with the $H = 40$ Kelvin wave is the $k^* = 1$ signal between 1 and 1.8 cycles per day. The extratropical variability, diagnosed following the recipe above, sits entirely at $k^* = 1$ (with some aliased variability at $k^* = -1$). While the approximate dispersion relation does not perfectly capture the extratropical variability it does make it clear that the variability must be wavenumber-1 since the spectral power cannot sit at partial wavenumbers.

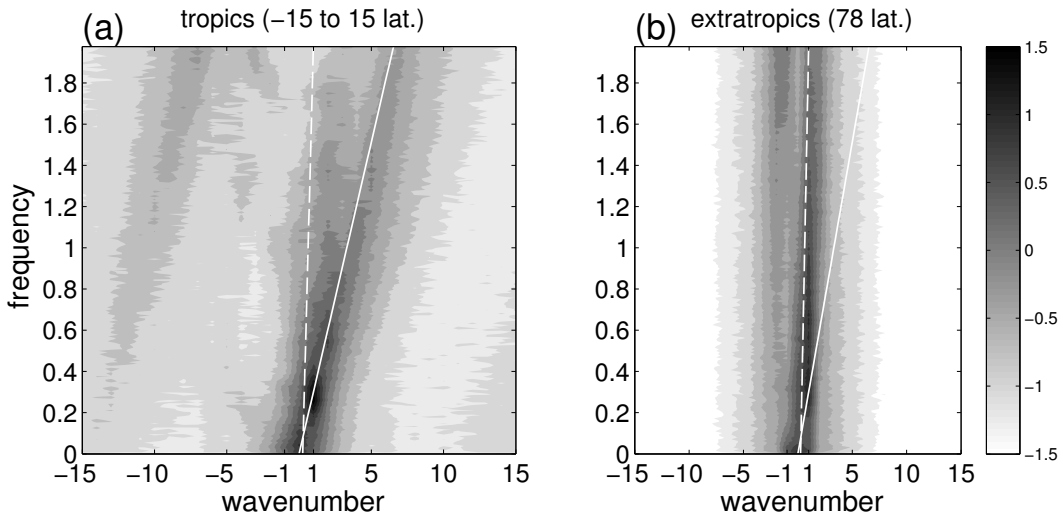


Figure 4.2: Base ten logarithm of the spectral power of the geopotential height field at 475 mb for the $a = 9e5$ m atmosphere. (a) Spectral power between -15 and 15 degrees latitude. (b) Spectral power at 78 degrees latitude. Solid lines show the $H = 40$ Kelvin wave dispersion curve and the dashed lines show the approximate Rossby wave dispersion relation, Eq. 4.8.

Fig. 4.3 shows spectral power at another extreme, $a = 1.2e7$ m (double Earth's radius). There is very clear Kelvin variability for $H = 200$ and $H = 40$. The strongest eastward variability, which sits at wavenumber-1 and 0.35 cycles/day, perhaps corresponds to an extremely fast Kelvin wave. Again the recipe to construct Eq. 4.8 succeeds extremely well in capturing the main signals in extratropical variability.

The dispersion relation is also able to capture Rossby waves where they are generated and where they break. Fig. 4.4 shows the eddy momentum flux divergence, $\mathcal{S}$, in the $\omega - k^*$ plane at the central latitude where extratropical Rossby waves are generated (45°, Fig. 4.4a) and the central latitude where they break (24°, Fig. 4.4b). Note that the dispersion relation for both plots is evaluated at the storm track center, 45°. The wavenumber and frequency of the Rossby waves are conserved as they move towards the equator. Note that there is not perfect correspondence between the accelerating and decelerating regions – Rossby waves meet their critical line at different latitudes, and slower Rossby waves will propagate farther towards the equator.

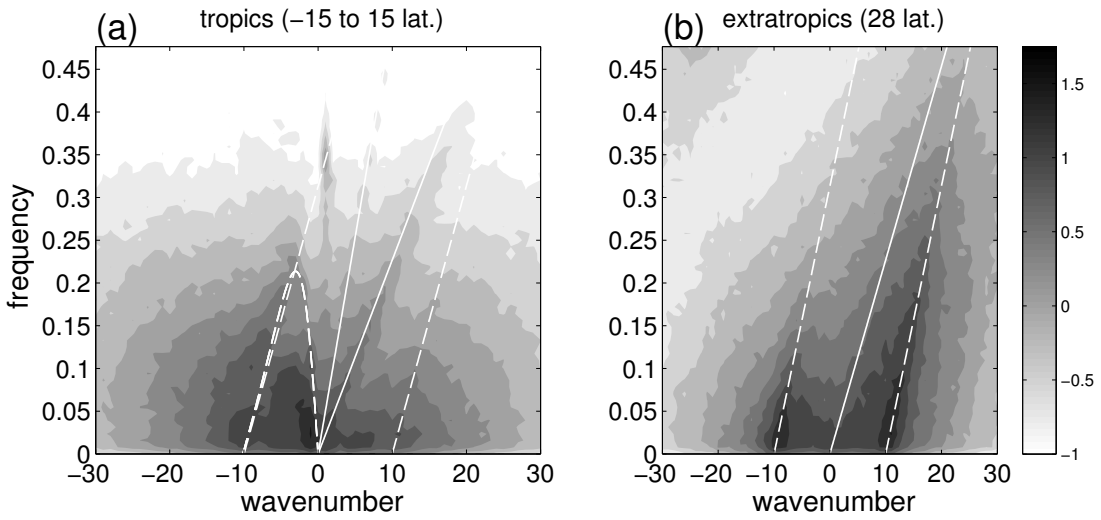


Figure 4.3: Base ten logarithm of the spectral power of the geopotential height field at 225 mb for the $a = 1.2e7$ m atmosphere. (a) Spectral power between -15 and 15 degrees latitude. Dashed curve shows theoretical dispersion relation for a Rossby-Haurwitz wave with equivalent depth of 15 km Doppler shifted by a 15 m/s wind. (b) Spectral power at 29 degrees latitude. Solid lines shows the $H = 40$ Kelvin wave dispersion curve and the dashed lines show the approximate Rossby wave dispersion relation, Eq. 4.8.

4.3.1 Nondimensional equation

Nondimensionalizing by 2Ω, Eq. 4.8 can alternately be written as

$$\omega/(2\Omega) = \frac{\overline{u}_0}{2\Omega a \cos\phi}\left(k^* \pm \sqrt{2}\left(\frac{2\Omega a \cos^3\phi}{\overline{u}_0}\right)^{1/2}\right) \tag{4.9}$$

$$\omega/(2\Omega) = \frac{R_o}{\mu}\left(k^* \pm \sqrt{2}\left(\frac{\mu^3}{R_o}\right)^{1/2}\right). \tag{4.10}$$

Two nondimensional parameters emerge: a Rossby number, $R_o = \overline{u}_0/(2\Omega a)$ and the latitude, $\mu = \cos\phi$. Note that the R_o here is different from the thermal Rossby number, $Ro_T = R\Delta H/(2\Omega a)^2$, which is diagnosed entirely from external parameters.

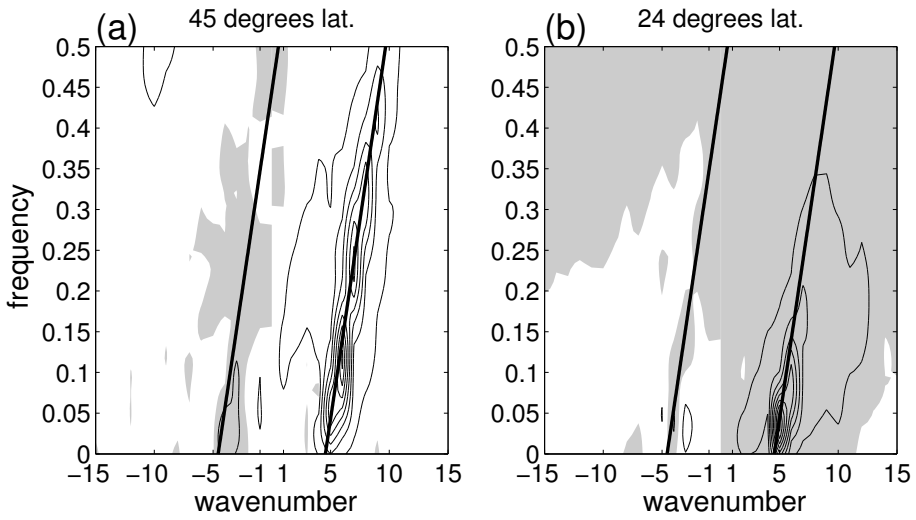


Figure 4.4: $\mathcal{S}$ in $\omega - k^*$ space. Contour intervals arbitrary, shaded regions negative. (a) At 45°, acceleration at this point is 5.2 m/s/day. (b) At 24°, acceleration at this point is -2.4 m/s/day. Solid lines show the approximate Rossby wave dispersion relation, Eq. 4.8 evaluated at 45°.

4.3.2 Frequency matching

One of the necessary conditions for excitation of tropical modes by extratropical variability is matching of the waves' wavenumber and frequency (e.g. Hayashi and Young, 1987; Zhang and Webster, 1992; Hoskins and Yang, 2000). Now that we have a dispersion relation for extratropical Rossby waves we can directly compare extratropical variability to the family of equatorial shallow water waves and locate where in spectral space they meet.

We start by setting the eastward component of our approximate Rossby wave dispersion relation (Eq. 4.8) equal to the Kelvin wave dispersion relation

$$\omega_{\mathrm{Ro}} = \frac{\overline{u}}{a\cos\phi}\left(k^* - \sqrt{2}\left(\frac{2\Omega a\cos^3\phi}{\overline{u}}\right)^{1/2}\right) = \sqrt{gH}\frac{k^*}{a} = \omega_{\mathrm{K}} \tag{4.11}$$

Where ω_{Ro} is the Rossby wave dispersion relation and ω_{K} is the Kelvin wave dispersion relation. H is the equivalent depth and $\sqrt{gH}$ is the gravity wave speed. Note again that

k^* is the key wavenumber quantity, since k^*/a is the wavenumber on the equatorial β-plane and $k^*/(a\cos\phi)$ is the relevant wavenumber for the extratropical Rossby waves.

Solving for k^* gives

$$k^*_{\text{match}} = \left(\frac{2\Omega a\cos^3\phi}{\overline{u}_0}\right)^{1/2} \Big/ \left(1 - \frac{\sqrt{gh}}{\overline{u}_0/\cos\phi}\right) \tag{4.12}$$

Plugging Eq. 4.12 into Eq. 4.11 gives the matched frequency

$$\omega_{\text{match}} = 2\sqrt{2}\Omega\left(\frac{\overline{u}_0\cos\phi}{2\Omega a}\right)^{1/2} \Big/ \left(\frac{\overline{u}_0/\cos\phi}{\sqrt{gh}} - 1\right) \tag{4.13}$$

We again nondimensionalize to get

$$k^*_{\text{match}} = \frac{\sqrt{2}(\mu^3/R_o)^{1/2}}{1-\mu/Fr} \tag{4.14}$$

$$\omega_{\text{match}}/(2\Omega) = \frac{\sqrt{2}(R_o\mu)^{1/2}}{Fr/\mu - 1} \tag{4.15}$$

where $Fr = \overline{u}/\sqrt{gh}$ is a Froude number, the ratio of the (extratropical) mean zonal wind speed to the gravity wave speed.

The frequency and wavenumber are plotted in Figs. 4.5 and 4.6 as functions of R_o, Fr, and ϕ. For fixed $\mu = 0.71$ (which gives $\phi = 45°$, the control atmosphere value) in Fig. 4.5, the wavenumber is mostly a function of R_o, except at low values of Fr. Wavenumbers are maximized at low Fr and R_o and minimized for large Fr and R_o. The slowest frequencies occur for small R_o and large Fr, while the fastest happen at small Fr and large R_o.

In Fig 4.6 k^* and ω are plotted for fixed $Fr = 1.6$ (the value in the control atmosphere, taking $\overline{u} = 32$ and $H = 40$) for varying R_o and latitude ϕ. We plot versus latitude ϕ rather than cosine of latitude μ to better illustrate the latitude of Rossby wave generation. k^* is maximized at low latitudes and small R_o, while the smallest wavenumbers occur at high

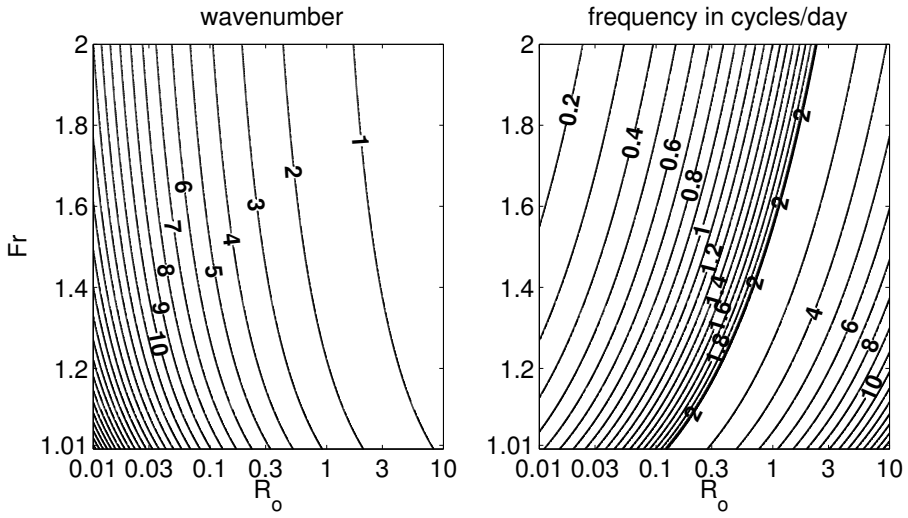


Figure 4.5: Wavenumber k^*, Eq. 4.14 (a) and frequency in cycles per day ω, Eq. 4.15 as functions of the Rossby number $R_o = \overline{u}/(2\Omega a)$ and Freude number $Fr = \overline{u}/\sqrt{gH}$ for fixed cosine of 45° latitude, $\mu = 0.71$. (a) Contours at every wavenumber. (b) Contours every 0.1 cycles/day up to 2 then contours every 1 cycle per day.

latitudes and large R_o. The lowest frequencies occur at small R_o and high latitudes, while the fastest are at large R_o and low latitudes.

4.4 Equatorial waves in the superrotating a = 9e5 m and Williams 2003 atmospheres

Now that we have predictions for where in $\omega - k$ space tropical and extratropical waves might overlap and resonate, we can test to see if the predicted intersection actually manifests in superrotating atmospheres. We will use two example atmospheres, the $a = 9e5$ m atmosphere discussed above and in Ch. 2 and the $\cos^{32}\phi$ Williams atmosphere discussed below.

Williams (2003) showed that as the exponent of the latitudinal dependence of Newtonian cooling $\cos^r \phi$ is increased from $r = 2$ to increasing powers of two, the atmosphere transitions to strong superrotation. Potter et al. (2014) showed that this superrotation was the result of equatorial Kelvin waves fluxing momentum towards the equator. Here we do not mimic

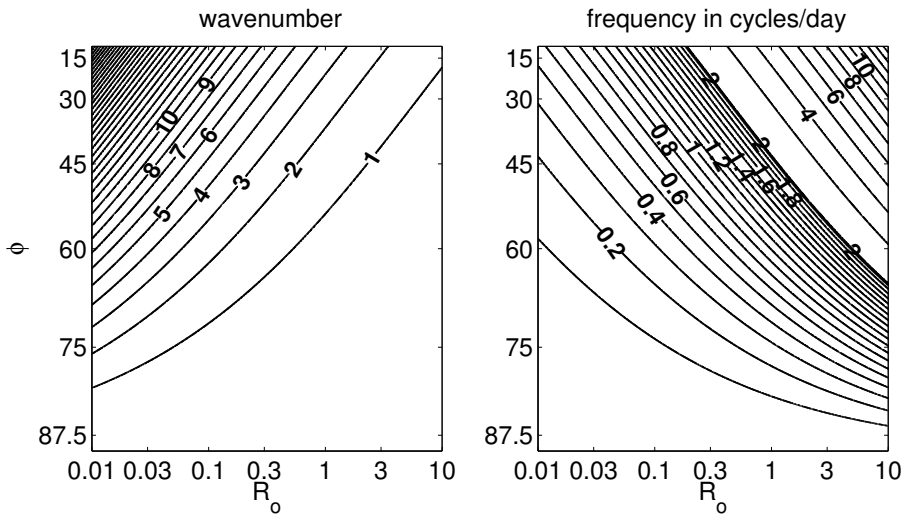


Figure 4.6: Wavenumber n, Eq. 4.14 (a) and frequency in cycles per day ω, Eq. 4.15 as functions of the Rossby number $R_o = \overline{u}/(2\Omega a)$ and latitude ϕ for Freude number $Fr = 1.6$. (a) Contours at every wavenumber. (b) Contours every 0.1 cycles/day up to 2 then contours every 1 cycle per day.

exactly Williams' result, but simply modify the Held-Suarez Newtonian cooling to have $r = 32$ latitudinal dependence. We will refer to this as the $\cos^{32}\phi$ atmosphere, which is strongly superrotating. The climatology of the $\cos^{32}\phi$ atmosphere is shown in Fig. 4.7, which should be compared to the control atmosphere in Fig. 2.1. The most obvious feature of the $\cos^{32}\phi$ atmosphere is the strong superrotation and strong jets lying very near the equator at 20°. The main temperature contrast lies much closer to the equator, following the much steeper Newtonian cooling profile. The eddy momentum flux, like the jets, lies much closer to the equator.

The spectral power of the tropical and extratropical geopotential height of the $\cos^{32}\phi$ atmosphere are shown in Fig. 4.8. The tropical spectrum has strong signals near the $k^* = 2$ and 3 near the $H = 40$ Kelvin wave line (Fig. 4.8a). There is now another signal starting near $k^* = 5$ in the tropical variability, which clearly corresponds to the main signal in the extratropical Fig. (Fig. 4.8b). The tropics also clearly reflects on the extratropics, with the strong $k^* = 2$ Kelvin wave signature clearly showing up nearly 30° from the equator.

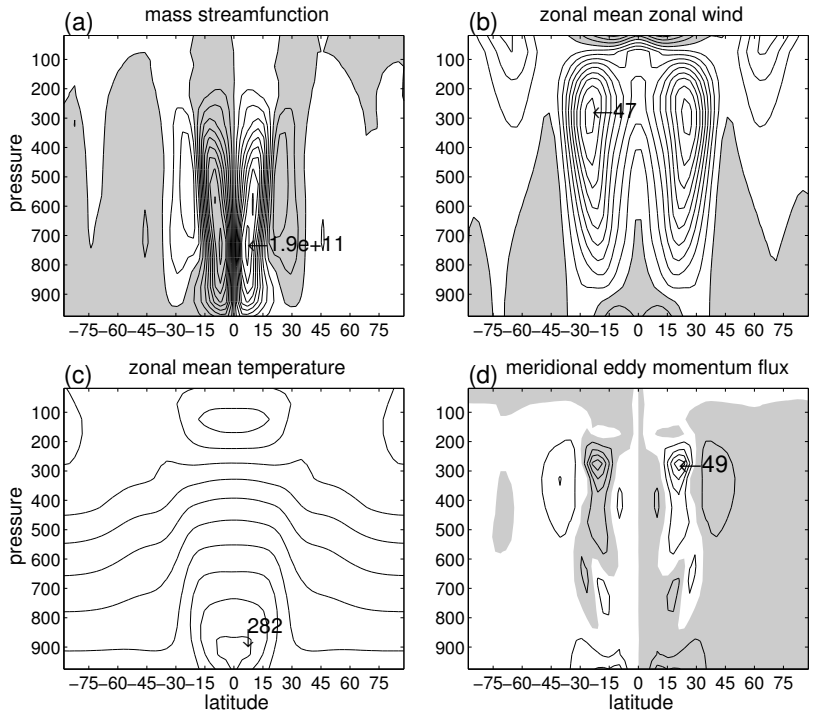


Figure 4.7: Climatological fields for the $\cos^{32}\phi$ atmosphere. (a) Mass streamfunction, contour interval $2e10$ kg/s. (b) Zonal mean zonal winds, contour interval 5 m/s. (c) Zonal mean temperature, contour interval 10 K. Shaded areas negative valued. (d) $\overline{u'v'}\cos\phi$, contour interval 5 $\mathrm{m}^2/\mathrm{s}^2$. Largest values highlighted.

Now that we have characterized the tropical and extratropical variability in these two superrotating atmospheres we can check to see if the matching arguments can predict which tropical mode is the result of unstable coupling with extratropical modes and, consequently, responsible for fluxing momentum to the equator. Fig. 4.9 shows $\mathcal{S}$ in $\omega - k$ space for the (a) $a = 9e5$ m atmosphere and (b) the $\cos^{32}\phi$ atmosphere. Overlaid are the $H = 40$ Kelvin wave dispersion lines (solid) and the dominant (eastward) extratropical Rossby wave dispersion relation. If we follow the reasoning discussed above, we can say that any predicted variability with $0 < k^* < 1$ should be taken to be at $k^* = 1$, and the predicted $k^* = 1$, low frequency mode matches the actual mode. This is *not* the case in the $\cos^{32}\phi$ atmosphere. The dominant mode lies at $k^* = 2$ and roughly 0.07 cycles/day, far away from the predicted mode near $k^* = 8$ and 0.4 cycles/day. This is evidence that overlapping of the Kelvin wave

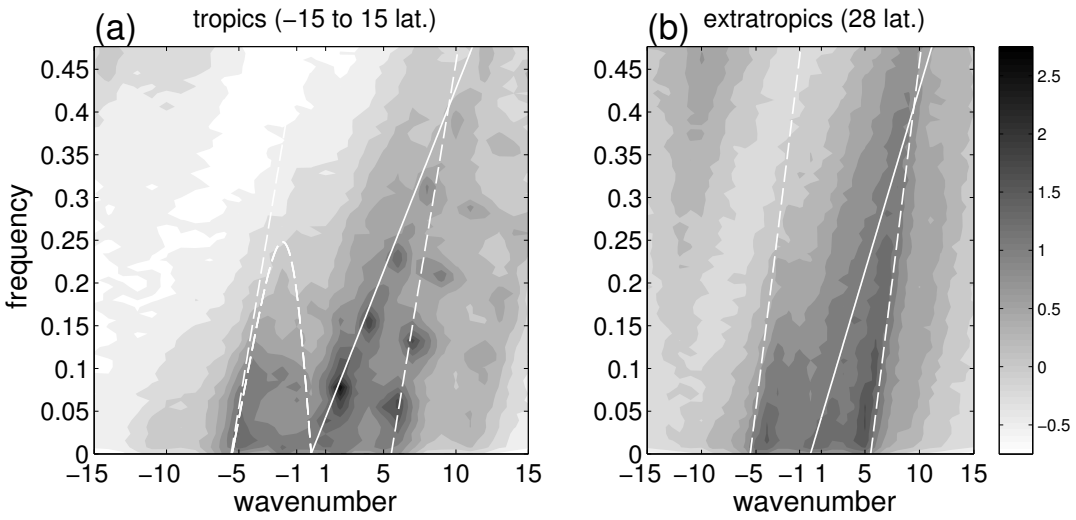


Figure 4.8: Base ten logarithm of the spectral power of the geopotential height field at 425 mb for the $\cos^{32}\phi$ atmosphere. (a) Spectral power between -15 and 15 degrees latitude. Dashed curve shows theoretical dispersion relation for a Rossby-Haurwitz wave with equivalent depth of 15 km Doppler shifted by a 15 m/s wind. (b) Spectral power at 28 degrees latitude. Solid lines shows the $H = 40$ Kelvin wave dispersion curve and the dashed lines show the approximate Rossby wave dispersion relation, Eq. 4.8, discussed in the text.

and extratropical Rossby wave frequencies and wavenumbers is necessary but insufficient to lead to coupled tropical-extratropical modes. Though the spectral power is roughly an order of magnitude weaker away from the ridge starting at $k^* = 5$ in Fig. 4.8, there is still non-negligible power at wavenumbers relevant to $k^* = 1, 2, 3, 4$ Kelvin waves. The importance of low-wavenumber tropical-extratropical coupling is discussed in the following section.

4.5 A wave evanescence argument

From the previous sections it is clear that wavenumber and frequency matching of tropical and extratropical modes is insufficient for coupled tropical-extratropical modes to develop. In this section we describe a second condition for this wave coupling – that the waves are able to 'see' each other.

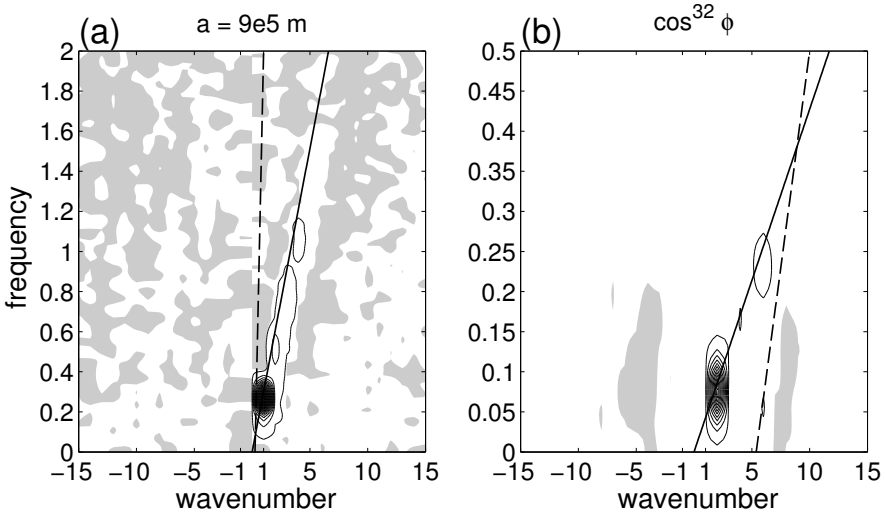


Figure 4.9: $\mathcal{S}$ in $\omega - k$ space at the equator for the (a) a = $9e5$ m atmosphere (acceleration at this point is 1.7 m/s/day) and the (b) $\cos^{32}\phi$ atmosphere (acceleration at this point is 0.24 m/s/day). Contour intervals arbitrary, shaded regions negative. The overlaid lines are the $H = 40$ Kelvin wave dispersion relation (solid) and the approximate (eastward only) extratropical Rossby wave dispersion relation (solid) as plotted in Fig. 4.2b for the a = $9e5$ m atmosphere and Fig. 4.8b for the $\cos^{32}\phi$ atmosphere.

As discussed in the introduction, Zhang and Webster (1992); Zhang (1993); Hoskins and Yang (2000) showed that a wavemaker located on the equatorward side of the equatorial waveguide excited equatorial waves. Here we take a similar idea but assume that the wavemakers are the storm tracks, and that the wave energy must move equatorward before it reaches the equatorial waveguide.

The outline of the argument is sketched in Fig. 4.10. The key distance between the extratropical and tropical waves is $a(\phi_0 - \phi_1)$, the distance between where the extratropical waves meet their critical line and break, ϕ_0 and the edge of the equatorial waveguide (equatorial Rossby radius of deformation), ϕ_1. The key to excitation of equatorial modes is minimizing loss of wave energy as the extratropical wave energy evanesces from ϕ_0 to ϕ_1.

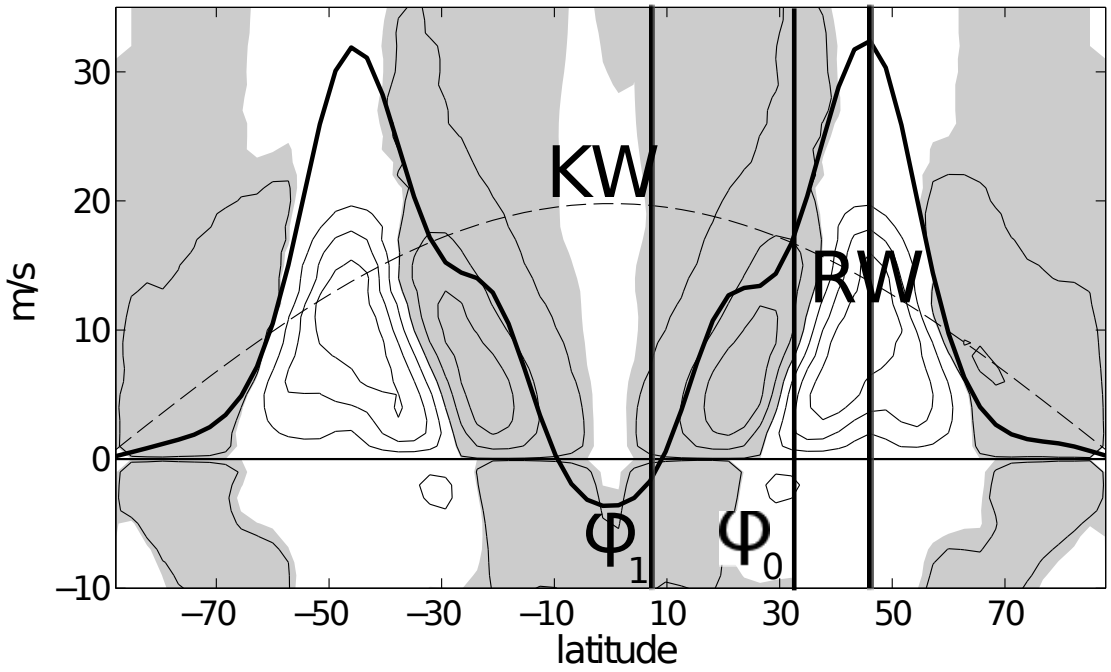


Figure 4.10: Outline of evanescence argument. The zonal mean zonal wind (thick black curve) overlays the $\mathcal{S}$ cospectra (contours and shading, gray shading negative). The angular frequency of the zonal mean zonal wind equals the Kelvin wave frequency at ϕ_0 (2nd black vertical line). The equatorial radius of deformation extends from the equator to ϕ_1 (first black vertical line). The Kelvin waves are centered over the equator, the Rossby waves are generated at the latitude labeled by the third black vertical line.

4.5.1 Equatorial deformation radius

ϕ_1 is the waveguide (turning latitude) of equatorial waves, the equatorial Rossby radius of deformation (Matsuno, 1966; Zhang and Webster, 1992):

$$a\phi_1 = \left(\frac{\sqrt{gH}}{\beta|_{equator}}\right)^{1/2} \tag{4.16}$$

$$\rightarrow \phi_1 = \left(\frac{\sqrt{gH}}{2\Omega a}\right)^{1/2} = \left(\frac{\overline{u}}{2\Omega a}\frac{\sqrt{gH}}{\overline{u}}\right)^{1/2} \tag{4.17}$$

$$\rightarrow \phi_1 = \left(\frac{R_o}{Fr}\right)^{1/2}. \tag{4.18}$$

R_o and Fr are again the Rossby and Froude number, respectively. We assume $\overline{u}$ is defined similarly as before, the maximum jet strength at the latitude band where the westerlies peak.

A smaller Froude number (e.g. faster gravity wave speed) and larger R_o (e.g. smaller radius or rotation rate) leads to a larger ϕ_1.

4.5.2 Determination of critical latitude

There is no simple way to estimate ϕ_0. In the midlatitudes a continuous spectrum of modes will be excited having angular velocities between the angular velocities defined by the zonal wind minimum and maximum (e.g. Held, 1985). ϕ_0 is the latitude where the zonal mean wind has angular velocity equal to the equatorial gravity wave speed, $\overline{u}/\cos\phi = \sqrt{gH}$ and a Rossby wave that breaks at ϕ_0 will have a frequency matching that of an equatorial Kelvin wave. We assume there is one dominant equivalent depth in the tropical troposphere, as is true in the control atmosphere (Fig. 4.1a), but may not be true in a moist atmosphere (Wheeler and Kiladis, 1999). ϕ_0 will always be equatorward of the latitude ϕ that was used to determine the dispersion relation Eq. 4.8. While we do not have a direct estimate of ϕ_0, the the center of the storm tracks as determined from zonal mean climatology provides an upper bound.

4.5.3 A crude description of evanescence between the Rossby wave breaking latitude and the tropical waveguide

To describe the meridional movement of the extratropical Rossby wave energy we make the WKB assumption (e.g. Ch. 3) and approximate the meridional component of the stream-function ψ as

$$\psi(\phi) \approx \psi_0 \exp(i\ell a\phi) \tag{4.19}$$

$$\ell^2 = \left[\beta - \frac{1}{a^2}\frac{\partial}{\partial\phi}\left(\frac{1}{\cos\phi}\frac{\partial}{\partial\phi}(\overline{u}\cos\phi)\right)\right] / (\overline{u} - a\cos\phi\omega) - \frac{k^{*2}}{a^2\cos^2\phi} \tag{4.20}$$

Where ψ_0 is an initial magnitude of ψ and ℓ is an approximate local meridional wavenumber. $a\cos\phi\omega$ is the phase speed and ω is the frequency.

We want to see what maximizes the fraction of the wave energy that starts at ϕ_0 and reaches ϕ_1:

$$\psi(\phi_1)/\psi(\phi_0) = \exp\left(i\overline{\ell}a(\phi_1 - \phi_0)\right) \tag{4.21}$$

where we are now defining an 'effective' or mean meridional wavenumber $\overline{\ell}$ that captures the changes in ℓ between ϕ_0 and ϕ_1. This is clearly a fabrication but it allows us to capture gross changes in ℓ and say that a smaller $|\ell|$ will lead to less evanescence.

We can nondimensionalize ℓ by absorbing the factor of a. We note that the relevant Rossby wave frequency is equal to the Kelvin wave frequency, so we can set $\omega = \sqrt{gH}k^*/a$ and Eq. 4.20 can be rewritten as

$$a\ell = \left(\left[2\Omega a\cos\phi - \frac{\partial}{\partial\phi}\left(\frac{1}{\cos\phi}\frac{\partial}{\partial\phi}(\overline{u}\cos\phi)\right)\right] / \left(\overline{u} - \sqrt{gH}\cos\phi\right) - \frac{k^{*2}}{\cos^2\phi}\right)^{1/2} \tag{4.22}$$

$$= \left(\left[\frac{1}{R_o}\cos\phi - \frac{\partial}{\partial\phi}\left(\frac{1}{\cos\phi}\frac{\partial}{\partial\phi}(u^*\cos\phi)\right)\right] / (u^* - \cos\phi/Fr) - \frac{k^{*2}}{\cos^2\phi}\right)^{1/2} \tag{4.23}$$

where $u^* = \overline{u}/\overline{u}_0$ and R_o and Fr are defined as before. Closer to the equator β dominates the zonal wind curvature term, so the numerator of the first term in Eq. 4.23 will be positive, while past the critical latitude the denominator will be negative. Therefore an increase in R_o or Fr will decrease the magnitude of $a\ell$. A smaller wavenumber k^* clearly reduces the magnitude of $a\ell$. The retention of evanescing wave energy seems to be preferred for large R_o, large Fr and small k^*.

4.5.4 Why the small radius and Williams 2003 atmospheres are prone to superrotation.

We can now quickly see why the $\cos^{32}\phi$ atmosphere superrotates. In the control atmosphere the extratropical Rossby waves are generated at 45°, so $\phi_0 < 45°$. In both the control and $\cos^{32}\phi$ atmospheres the tropical waveguide (Eq. 4.17) with an equivalent depth of $H = 40$ m is $\phi_1 = 8.4°$. Therefore the distance $\phi_0 - \phi_1$ has an upper bound of 36.6° or 60% of the Earth's radius. In the $\cos^{32}\phi$ atmosphere the extratropical Rossby waves are generated at 28°, so the distance $\phi_0 - \phi_1$ has an upper bound of 19.6° or 34% of Earth's radius. Therefore the extratropical wave energy has to evanesce over approximately half the distance to reach the tropical waveguide in the $\cos^{32}\phi$ atmosphere. We can also understand why the $k^* = 2$ mode dominates the tropical $\cos^{32}\phi$ atmosphere in Figs. 4.8a and 4.9b. As discussed above a smaller k^* leads to a smaller $|\ell|$, and, consequently, less evanescence. Even though the extratropical energy is stronger near $k^* = 5$ in Fig. 4.8b, the $k^* = 2$ wave energy is better able to reach the tropical waveguide and excite tropical modes.

There are two reasons why the evanescence is minimized in the $a = 9e5$ m atmosphere. First, in the $a = 9e5$ m atmosphere $\phi_0 - \phi_1$ is larger than in the control. Extratropical Rossby waves are generated at 78° and $\phi_1 = 22.3°$ gives an upper bound to $\phi_0 - \phi_1$ of 55.7°. However, the distance between the two points in meters is only 14% of Earth's radius, compared to 60% in the control atmosphere. Secondly, the Rossby radius of deformation is largely unchanged even as a is decreased. This implies that the scale of Rossby waves relative to the planetary size is greatly increased and the dominant extratropical wavenumber decreases from 5-8 in the control extratropics (Fig. 4.1b) to 1 in the $a = 9e5$ atmosphere (Fig. 4.2b). Extratropical waves take on a planetary, rather than a synoptic, scale. This behavior is also captured in our matching conditions in Figs. 4.5a and 4.6a, where the large Rossby number atmospheres clearly have a preference for small n waves. This combination of small a and small k^* serves

to decrease both $a(\phi_1 - \phi_0)$ and $|\ell|$ and consequently greatly decreases the evanescence of extratropical wave energy.

4.6 Conclusion

In this chapter we have attempted to understand why and when tropical and extratropical waves couple and resonate. By looking at midlatitude spectral power we were able to derive an approximate dispersion relation for extratropical Rossby waves. This dispersion relation allowed for a direction comparison of equatorial (with dispersion relations provided by Matsuno (1966)) and extratropical waves and we explored where in $\omega - k^*$ space extratropical Rossby waves and equatorial Kelvin waves have overlapping dispersion relations. A simple overlap between the Kelvin and Rossby wave dispersion relations was all that was necessary to predict which equatorial mode is responsible for superrotation in the $a = 9e5$ m atmosphere. This overlap argument, however, was insufficient to describe the relevant modes in the superrotating $\cos^{32}\phi$ atmosphere from Williams (2003). To better explain both the $\cos^{32}\phi$ and $a = 9e5$ m equatorial modes we lastly argued that minimizing wave evanescence between the extratropics and the equatorial waveguide was a key ingredient in superrotating atmospheres. In the $a = 9e5$ atmosphere wave evanescence is minimized because the planet is smaller (and thus extratropical waves have less distance to travel) and because the local meridional wavenumber controlling the magnitude of evanescence is decreased. In the $\cos^{32}\phi$ atmosphere the storm tracks are so close to the equator that extratropical Rossby waves easily imprint their energy onto the tropics.

Chapter 5

The momentum balance and equatorial waves of a seasonally varying dry dynamical core

5.1 Introduction

The zonal mean zonal winds in Earth's equatorial upper troposphere are easterly throughout the year. Using reanalysis, Lee (1999) showed that these easterlies are maintained by the seasonal Hadley cell. Lee's result was somewhat in opposition to previous work, which argued that Earth's tropical easterlies were in large part maintained by the breaking of midlatitude Rossby waves propagating into the deep tropics (Suarez and Duffy, 1992; Saravanan, 1993; Held, 1999). Rossby wave breaking is quite weak in the deep tropics, and Lee showed that it is only non-negligible for the deep tropical momentum balance in a permanent equinox atmosphere. Kraucunas and Hartmann (2005) showed that a model without a permanent equinox (no seasonal cycle) will superrotate with tropical stationary wave forcing similar to that found on Earth. However, this superrotation was eliminated when an idealized seasonal

forcing was placed into the model, and the authors showed that the cross equatorial flow of the seasonal Hadley cell wiped out deep tropical westerlies. Both of these studies show that seasonality is the key to maintaining Earth's equatorial easterlies.

In Lee (1999), momentum flux divergence of the seasonal mean flow (westward acceleration) was shown to be balanced by eastward acceleration due to both stationary eddies and transient eddies. Kraucunas and Hartmann (2005) looked at permanent solstitial atmospheres and found that the primary tropical balance was between the divergence of the mean momentum flux and Coriolis drag (westward acceleration) and eastward acceleration by the imposed stationary wave. Eq. 5.1 shows the free troposphere zonal mean zonal momentum equation decomposed into eddy terms (denoted by primes) and the mean flow (denoted by overbars). The metric term $uv\tan\phi$ is neglected. Kraucunas and Hartmann (2005) and Lee (1999) showed that the mean flow (first three terms on righthand side of Eq. 5.1) provides a westward acceleration to the tropical upper troposphere which is offset by stationary and transient eddies' meridional momentum transport (third term in Eq. 5.1).

$$\frac{\partial[\overline{u}]}{\partial t} = \underbrace{f[\overline{v}]}_{\text{Coriolis acceleration}} - \underbrace{\frac{\overline{v}}{a\cos\phi}\frac{\partial\overline{u}}{\partial\phi} - \overline{\omega}\frac{\partial\overline{u}}{\partial p}}_{\text{Mean flow momentum advection}} - \underbrace{\frac{1}{a\cos^2\phi}\frac{\partial}{\partial\phi}\left([\overline{u'v'}]\cos^2\phi\right)}_{\text{Meridional eddy momentum flux divergence}} - \underbrace{\frac{\partial[\overline{u'\omega'}]}{\partial p}}_{\text{Vertically eddy momentum flux divergence}} \tag{5.1}$$

We want to approach this problem from the other direction and ask: if a model has zonally symmetric forcing and a seasonal cycle, or solstitial rather than equinoctial forcing, what eddy dynamics balance the westward acceleration of the deep tropical zonal wind?

The remainder of this chapter is organized as follows. Section 5.2 describes the dry seasonal model physics. Section 5.3 shows the zonal mean climatologies and momentum budgets of equinoctial, seasonal, and solstitial atmospheres. Section 5.4 shows various spectra as-

sociated with the seasonal and solstitial atmospheres. Section 5.5 discusses the equatorial temperature minimum and tropical eddy heat transports that occur in the seasonal atmosphere. Section 5.6 discusses the timing of instability in the seasonal atmosphere.

5.2 Methods

5.2.1 Model forcing

Schneider and Bordoni (2008) studied monsoon circulations using a dry Newtonian-cooling forced dynamical core with an idealized seasonal cycle. The seasonal cycle is induced by letting the maximum surface heating vary in latitude as a function of time. The key parameter in their model is maximum latitude to which the latitudinal maximum in thermal forcing migrates to in the course of a year, $\phi_{\max}$. Unlike most studies with Held-Suarez forced dynamical cores, the Schneider and Bordoni (2008) model has an idealized, dry convection scheme which relaxes the thermal profile back to a set, stable lapse rate.

Mitchell et al. (2014) constructed a seasonally varying Newtonian cooling by starting with a simplified surface energy balance model and deriving a surface temperature profile that varies in latitude and time of year. A key difference compared to Schneider and Bordoni (2008) is the inclusion of a surface heat capacity which allows the forcing to model planetary atmospheres that have large (e.g. Earth) or minimal (e.g. Mars) surface heat capacities. The model has an obliquity of 90° and seasonality is controlled by the parameter α, which is a measure of the surface heat capacity.

We use a seasonal forcing built on Held-Suarez that uses parts of the studies mentioned above. Following Schneider and Bordoni (2008) and Held and Suarez (1994), the Newtonian

cooling profile T_e is made to be:

$$T_{\text{surface}}(t) = 315 - 60\sin^2\phi + 60S(t) \tag{5.2}$$

$$S(t) = 2\sin(\phi_{\max}\sin(2\pi t/365))\sin\phi \tag{5.3}$$

$$T_{\text{e}}(t,\sigma) = \left(T_{\text{surface}}(t) - 10\log(\sigma)\cos^2\phi\right)\sigma^{2/7} \tag{5.4}$$

where ϕ is latitude, σ is pressure normalized by the surface pressure and $S(t)$ is the seasonality factor, equal to zero in a permanent equinox integration. The Newtonian cooling timescale decreases from 4 days^{-1} at the surface to 40 days^{-1} above $\sigma > 0.7$ (the 'free troposphere') and has no latitudinal dependence. Unlike Schneider and Bordoni (2008), our model does not have a convection scheme and we do not seasonally vary the Newtonian cooling timescale.

All of our runs are done using the GFDL Flexible Modeling System spectral dynamical core. We use T42 spectral resolution with 40 unevenly spaced pressure levels, with extra resolution in the upper atmosphere. Several runs were done at higher resolution to test sensitivity to both vertical and horizontal resolution, with no significant difference in results.

5.3 Results

5.3.1 Climatologies

The control permanent equinox atmosphere is shown in Fig 5.1. The forcing here is exactly the same as Held and Suarez (1994), and Fig. 5.1 and Fig. 2.1 are almost identical, with the higher vertical resolution in Fig. 5.1 showing finer scale structure in the upper troposphere, particularly in the wind and temperature fields.

The climatology of the 23.5° $\phi_{\max}$ atmosphere is shown in Fig. 5.2. The time mean streamfunction being plotted here is weaker than that of the control (Fig. 5.1), but the seasonal, off equator Hadley cells are significantly stronger (the solstitial mass streamfunction

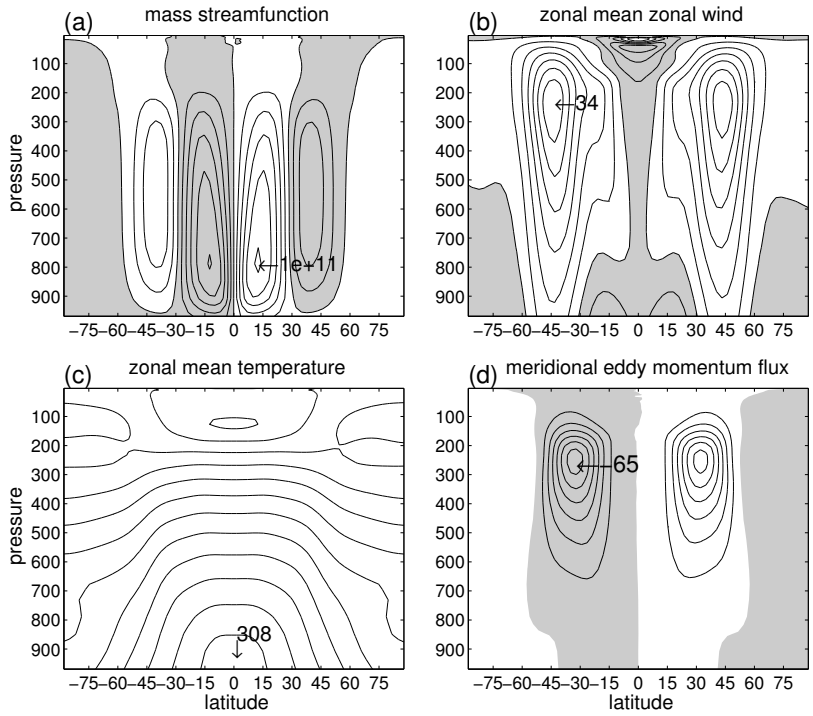


Figure 5.1: Time mean fields for the 0° $\phi_{\max}$ control atmosphere. (a) Mass streamfunction, contour interval $2x10^{10}$ kg/s. (b) Zonal mean zonal winds, contour interval 5 m/s. (c) Zonal mean temperature, contour interval 10 K. (d) $\overline{u'v'}\cos\phi$, contour interval 10 m^2/s^2. Shaded areas negative valued. Largest values highlighted.

peaks at $3.9x10^{11}$ kg/s). Temperatures are largely similar to the control, with equatorial near-surface temperatures slightly cooler. One interesting difference is the equatorial mid-troposphere minimum in temperatures, a feature that will be discussed in more detail in Section 5.5. The largest changes, however, can be seen in the zonal wind and eddy flux fields. The 23.5° $\phi_{\max}$ atmosphere has a strong easterly jet peaking at speeds greater than -20 m/s in the upper equatorial troposphere. While the deep tropics are a place of weak eddy momentum flux divergence ($\mathcal{S} < 0$) in the control climate, the 23.5° $\phi_{\max}$ atmosphere has a deep tropical wave source, with $\mathcal{S} > 0$ near the equator.

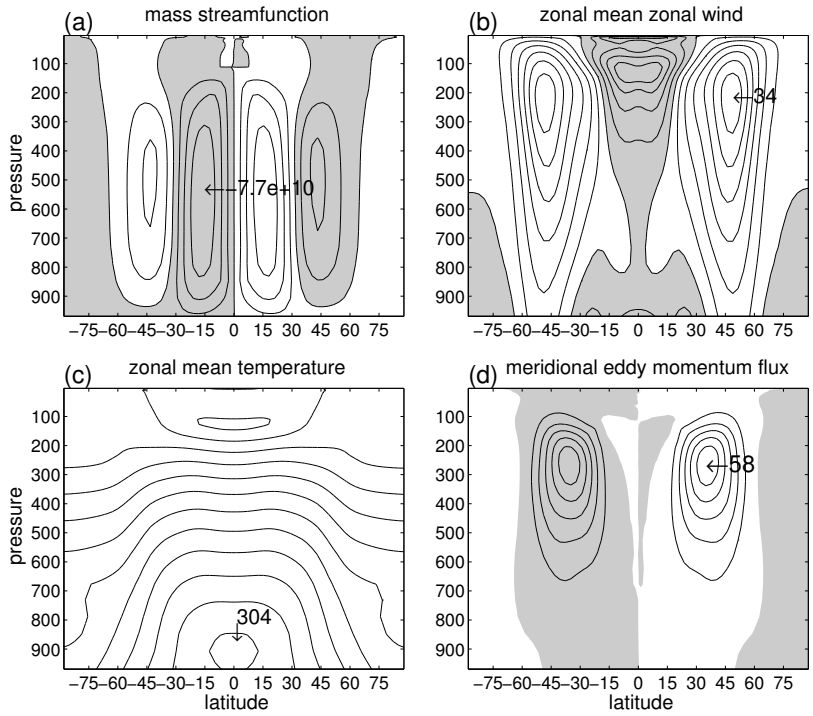


Figure 5.2: Time mean fields for the 23.5° $\phi_{\max}$ atmosphere. (a) Mass streamfunction, contour interval $1x10^{12}$ kg/s. (b) Zonal mean zonal winds, contour interval 5 m/s. (c) Zonal mean temperature, contour interval 10 K. (d) $\overline{u'v'}\cos\phi$, contour interval 20 m^2/s^2. Shaded areas negative valued. Largest values highlighted.

5.3.2 Momentum budgets

The differences in the equatorial winds and eddy fields are further broken down in Figs. 5.3 and 5.4, which show four of the five terms on the right hand side of Eq. 5.1 for the permanent equinox and 23.5° $\phi_{\max}$ atmospheres. From here on we ignore vertical eddy momentum flux divergence, which is only non-negligible in the midlatitudes of our runs. The primary balance in the control atmosphere's tropics is between Coriolis acceleration from the upper branch of the Hadley cell and deceleration by midlatitude eddies breaking as they reach their critical latitudes (Fig. 5.3c and 5.3d).

The momentum budget changes in a small but significant way in the seasonal integration (Fig. 5.4). For the seasonally varying case, momentum advection by the mean flow plays an important role in the tropical upper troposphere and meridional momentum advection

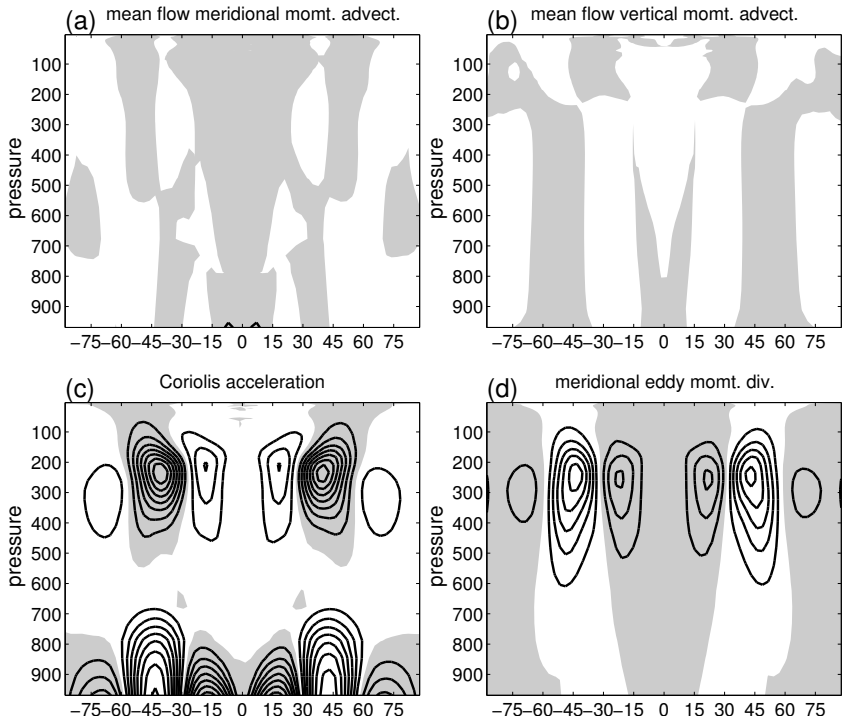


Figure 5.3: Zonal momentum budget for 0° $\phi_{\max}$ control atmosphere. Contour intervals 1 m/s/day. Shaded regions negative valued. (a) Mean flow meridional momentum advection. (b) Mean flow vertical momentum advection. (c) Coriolis acceleration. (d) Meridional eddy momentum flux divergence.

decelerates the wind (Fig 5.4a). Mean flow vertical advection accelerates the equatorial upper troposphere as the Hadley Cell acts against a strong easterly shear, advecting high momentum air from the surface (Fig 5.4a). On the whole, however, the mean flow provides an eastward torque on the equatorial upper troposphere winds. Away from the equator, the tropical momentum budget now balances three components: mean flow meridional advection and $\mathcal{S}$ (deceleration) and the Coriolis force (acceleration). Near the equator the mean flow deceleration is balanced by $\mathcal{S}$: an equatorial wave source that does not exist in the control atmosphere appears when the seasonal cycle is turned on (compare Figs. 5.3c and 5.4c).

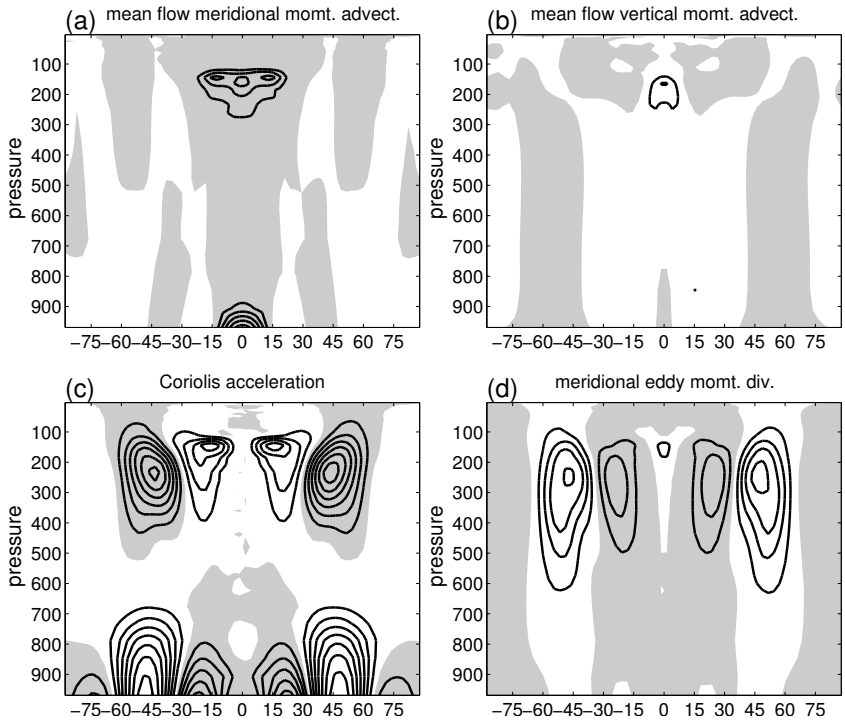


Figure 5.4: Zonal momentum budget for 23.5° $\phi_{\max}$ atmosphere. Contour intervals 1 m/s/day. Shaded regions negative valued. (a) Mean flow meridional momentum advection. (b) Mean flow vertical momentum advection. (c) Coriolis acceleration. (d) Meridional eddy momentum flux divergence.

5.3.3 Time dependency of acceleration terms

The equatorial eddy acceleration is a strong function of time-of-year. Fig. 5.5 shows the annual cycle of vertically averaged $\mathcal{S}$ averaged over the last 30 years of a 32 year run, smoothed using a 10 day running filter. Fig. 5.6 shows an annual cycle of maximum (in the vertical) of $\mathcal{S}$, after $\mathcal{S}$ has been regridded onto evenly spaced pressure levels. $\mathcal{S}$ is maximized in the midlatitudes of the winter hemisphere, reflecting the maximum in meridional temperature gradients and baroclinicity. Concurrent with the midlatitude maximum in $\mathcal{S}$ is a subtropical minimum where midlatitude waves reach their critical line and break. Equatorial $\mathcal{S} > 0$ also occurs when midlatitude variability is at its greatest. This is somewhat surprising since the breaking of midlatitude waves reaches its largest magnitude at the same time. The critical line appears to be far enough away from the equator to shield the deep tropics from breaking

midlatitude waves. As the permanent equinox control atmosphere has no equatorial $\mathcal{S} > 0$, it is not surprising that equatorial $\mathcal{S}$ maximizes near solstices.

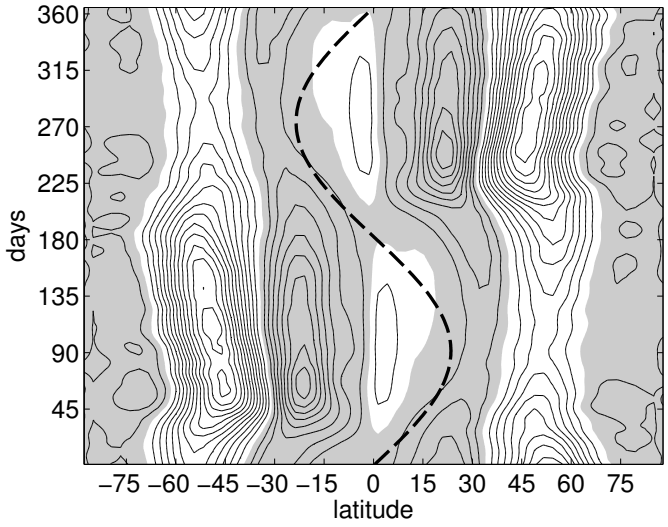


Figure 5.5: Smoothed seasonal cycle of vertically averaged $\mathcal{S}$ in the 23.5° $\phi_{\max}$ atmosphere. Contour intervals 0.25 m/s/day, shaded regions negative. The black dashed line shows the latitude of maximum Newtonian cooling temperature.

The eddy acceleration is relatively weak in the vertical mean. This is a product of the wave source being relatively thin in the vertical. As shown in Fig. 5.6 the equatorial wave source peaks at roughly 5 m/s/day, half of the peak midlatitude acceleration.

The seasonal cycle of all the acceleration terms at 144 mb (where the acceleration terms take on their largest values in the tropics) in Eq. 5.1 is shown in Fig. 5.7. By far the dominant terms are Coriolis acceleration and deceleration by the meridional advection of $\overline{u}$ in the winter hemisphere. Both terms decelerate the deep tropics of the summer hemisphere. The residual of these two dominant terms seems to determine the response of the rest of the terms. $\mathcal{S}$ and the mean flow vertical momentum advection (acting against a strong easterly shear) accelerate the deep tropical summer hemisphere after the tropical easterlies have peaked. The vertical eddy momentum term accelerates the winter extratropics and decelerates the winter subtropics, but contributes little to the tropical momentum balance.

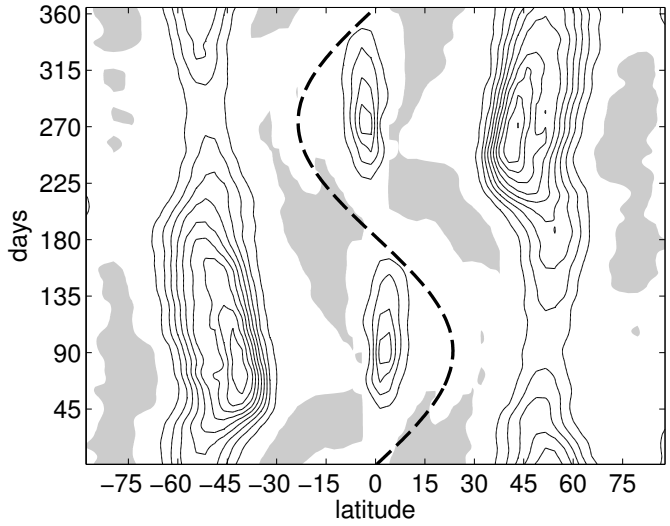


Figure 5.6: Smoothed seasonal cycle of maximum $\mathcal{S}$ in the 23.5° $\phi_{\max}$ atmosphere. Contour intervals 1 m/s/day, shaded regions negative. The black dashed line shows the latitude of maximum Newtonian cooling temperature.

5.3.4 Solstitial atmosphere

The extreme differences in the solstitial atmosphere circulation are shown in Figs. 5.8 and 5.9. The solstitial atmosphere is forced with a Newtonian cooling profile fixed at day 90, which is the northern hemisphere summer solstice. A strong solstitial Hadley cell now extends between 20°N and 30°S. The latitudinal maximum in surface temperature sits near 30°N and the equator has a local minimum in temperature throughout much of the troposphere. The equatorial easterly jet is much stronger, reaching a magnitude of 50 m/s near the equatorial tropopause, as compared to 20 m/s in the seasonally varying case (Fig. 5.2b).

All of the acceleration terms in Figs. 5.3 and 5.4 are exaggerated in the solstitial atmosphere in Fig. 5.9. The mean flow meridional advection strongly decelerates both hemispheres of the tropical upper troposphere, reaching 7 m/s/day eastward acceleration. This is in part balanced by the mean flow vertical advection which decelerates a thin region of the upper southern hemisphere troposphere but accelerates the northern hemisphere from 900 to 100 mb, reaching a magnitude of 5 m/s/day. The Coriolis term decelerates from 800 to 100 mb

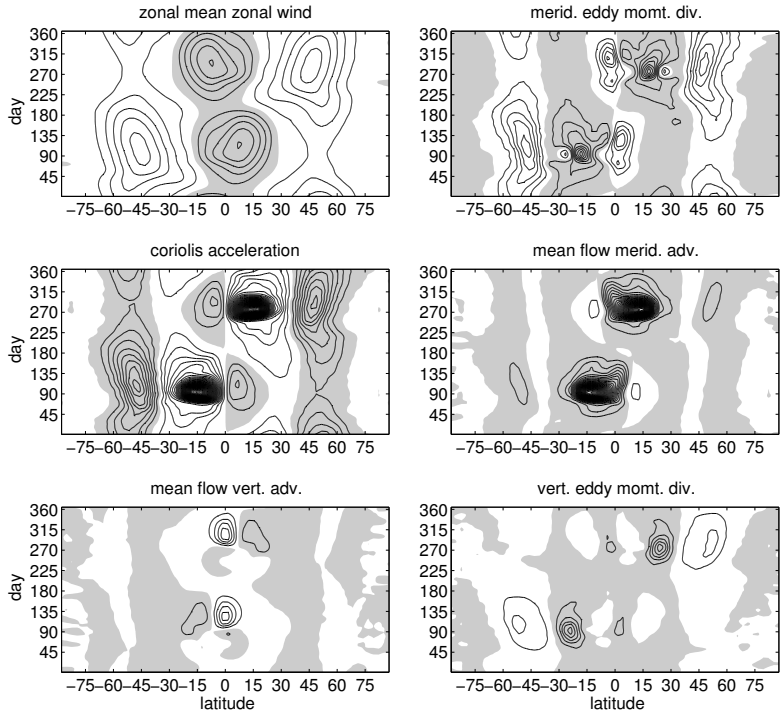


Figure 5.7: Smoothed seasonal cycle of (a) zonal mean zonal wind and (b)-(f) the five terms on the righthand side of the free troposphere momentum budget, Eq. 5.1 at 144 mb in the 23.5° $\phi_{\max}$ atmosphere. Contour intervals 1 m/s/day, shaded regions negative.

in the northern hemisphere and accelerates in the southern hemisphere upper troposphere, reflecting the solstitial Hadley cell. The elongated, tilted structure in vertical advection and Coriolis acceleration are a reflection of the slanting of the Hadley cell in the northern hemisphere (Fig. 5.8). The eddy term also takes on two signs in the tropical upper troposphere. $\mathcal{S} < 0$ in the southern hemisphere tropics and a small bullseye of $\mathcal{S} > 0$ exists between 100 and 200 mb in the northern hemisphere tropics. reaching a magnitude of 4 m/s/day, twice as strong as the acceleration found in the northern hemisphere's weak storm track.

The intermediate seasons (between days 1-90) show circulations that are intermediate between the control, equinox atmosphere (Figs. 5.1 and 5.3) and the solstitial day 90 atmosphere (Figs. 5.8 and 5.9). However, the equatorlal variability changes character over the course of the year, which we will discuss in the next section.

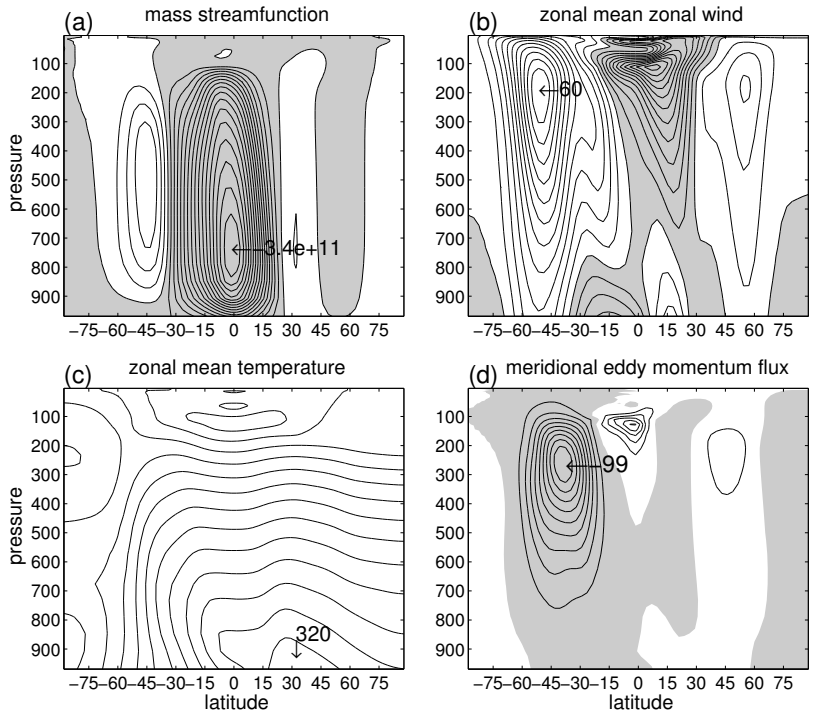


Figure 5.8: Time mean fields for the 23.5° $\phi_{\max}$ atmosphere fixed at Northern Hemisphere solstice forcing. (a) Mass streamfunction, contour interval $1x10^{12}$ kg/s. (b) Zonal mean zonal winds, contour interval 5 m/s. (c) Zonal mean temperature, contour interval 10 K. (d) $\overline{u'v'}\cos\phi$, contour interval 20 m^2/s^2. Shaded areas negative valued. Largest values highlighted.

5.4 Spectral diagnostics of seasonal atmospheres

As discussed in Ch. 2 we decompose $\mathcal{S}$ in wavenumber-frequency space to highlight the tropical modes that contribute to the maintenance of equatorial upper troposphere winds. Fig. 5.10 shows this diagnostic in the 40-level control atmosphere. The control has very weak eddy momentum fluxes at the tropical upper troposphere — at this point the acceleration is only -0.1 m/s/day. As in the 20 level model (Fig. 2.12b) there is weak acceleration due to a slow Kelvin-wave like eastward signal. Stronger deceleration can be seen for westward variability, likely comprised of breaking midlatitude Rossby waves that have propagated into the deep tropics. Fig. 5.11 shows the same diagnostic for several different versions of the

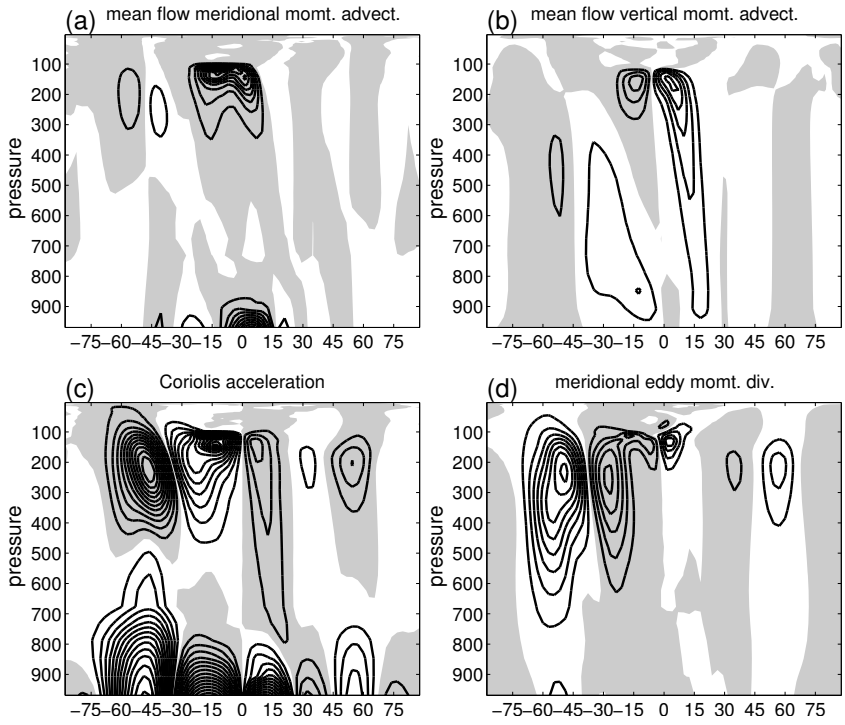


Figure 5.9: Zonal momentum budget for 23.5° $\phi_{\max}$ atmosphere fixed at Northern Hemisphere solstice forcing. Contour intervals 1 m/s/day. Shaded regions negative valued. (a) Mean flow meridional momentum advection. (b) Mean flow vertical momentum advection. (c) Coriolis acceleration. (d) Meridional eddy momentum flux divergence.

23.5° $\phi_{\max}$ atmosphere: seasonally varying forcing, forcing fixed at day 25, fixed at day 60, and fixed at day 90 (permanent solstitial forcing).

The four plots in Fig. 5.11 show three distinct types of equatorial wave variability. Overlaid on top of the figures are curves corresponding to the theoretical dispersion curves for equatorial shallow water waves (solid) and the theoretical curves with simple Doppler shifting (dashed) (Matsuno, 1966). All four atmospheres have a distinct Kelvin wave signal, mostly at wavenumber-1 and frequencies near 0.05 day^{-1} and lower. This signal seems to correspond best to a Kelvin wave with equivalent depth of 58 m (gravity wave speed$\sim$ 24 m/s) that is Doppler shifted by a -15 m/s zonal wind (dashed line for $k > 0$), although it is difficult to accurately judge the appropriate equivalent depth when the zonal winds are so strong. The almost-equinoctial fixed 25 atmosphere has the strongest relative Kelvin wave

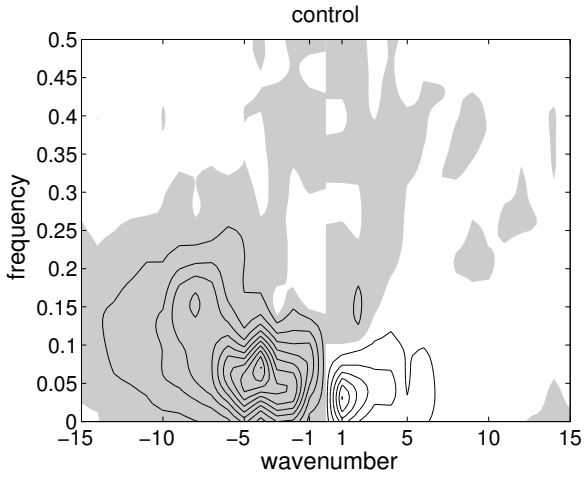


Figure 5.10: $\mathcal{S}$ in $\omega - k$ space at the equator and 260 mb in the control permanent equinox atmosphere. Acceleration is -0.1 m/s/day at this point.

signal. This signal is strongest at $k = 1$ but extends to higher wavenumbers at low frequency. All four atmospheres also have an equatorial Rossby (ER) wave signal ($k < 0$, solid line), though the fixed 90 atmosphere's signal is quite weak. In all the atmospheres the ER signal peaks at westward wavenumber-2 and low frequencies. The ER signal is strongest for the fixed 60 and time varying forcing atmospheres.

The third signal is somewhat unexpected. On the $k < 0$ side of the figures straight lines of eastward acceleration extend from $k = 0$ with varying slopes. Starting from fixed day 25 forcing the slope of this signal gets steeper closer to the solstice. The varying case splits the difference between these three fixed day cases. This signal appears to be easterly waves, also called 'tropical depressions' (Wheeler and Kiladis, 1999; Kiladis et al., 2009). Easterly waves are found over Africa/North Atlantic during summer months – "African Easterly Waves" (e.g. Kiladis et al., 2006) – as well as in the tropical Pacific (e.g. Magnusdottir and Wang, 2008). The 'dispersion relation' for these easterly waves can be approximated as an $n = 1$ equatorial Rossby wave that has been Doppler shifted by a mean zonal wind (Magnusdottir and Wang, 2008; Tulich et al., 2011). Fig. 5.12 shows that the dependence of equatorial zonal wind on time-of-year. As the forcing approaches solstice, the easterly winds get stronger,

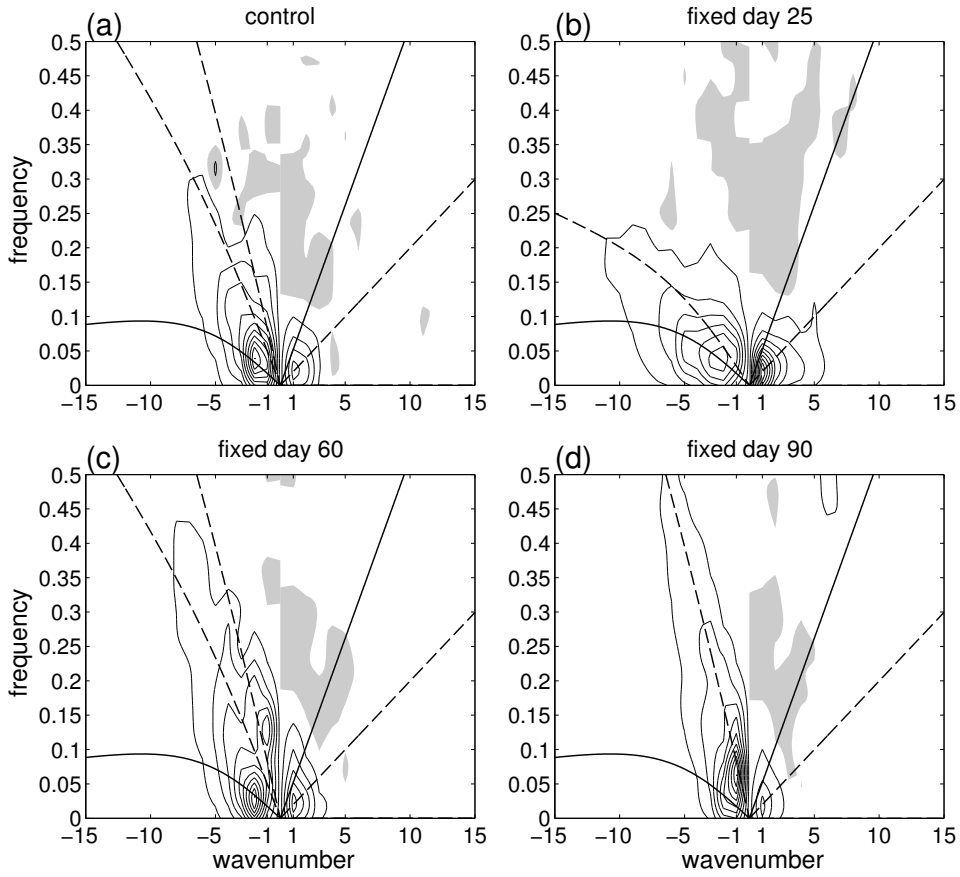


Figure 5.11: $\mathcal{S}$ in $\omega - k$ space at the equator and a specific pressure level for the 23.5° $\phi_{\max}$ atmosphere both seasonally varying and fixed at days 25, 60, and 90. Overlaid are dispersion relations for various equatorial waves with an equivalent depth of 58 m. On the lefthand side of all plots ($k < 0$) the solid line denotes an $n = 1$ equatorial Rossby (ER) wave and the dashed lines show the ER dispersion relation Doppler shifted by -5, -10, and -15 m/s winds. On the right hand side of all figures the solid line is a Kelvin wave and the dashed line is a Kelvin wave Doppler shifted by a -15 m/s zonal wind. (a) Seasonally varying atmosphere, acceleration 1.3 m/s/day at 144 mb. (b) Fixed day 25 atmosphere, acceleration 0.9 m/s/day at 163 mb. (c) Fixed day 60 atmosphere, acceleration 3.8 m/s/day at 144 mb. (d) Fixed day 90 atmosphere, acceleration 4.8 m/s/day at 127 mb.

as also seen in Fig. 5.7. This change in zonal wind clearly shows up in the easterly wave signal in Fig. 5.11. As the easterlies get stronger, the easterly wave signal, relatively flat in Fig. 5.11b, grows increasingly steeper up to the solstice, Fig. 5.11d.

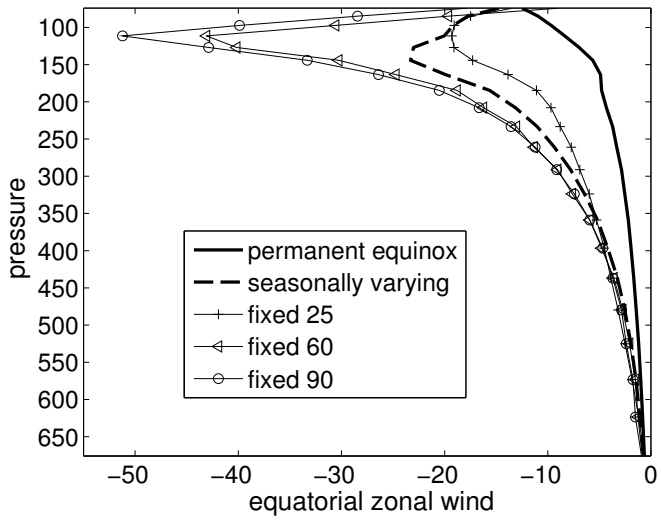


Figure 5.12: Equatorial zonal wind at the equator for the control (permanent equinox) atmosphere (solid black), seasonally varying atmosphere (dashed), fixed day 25 atmosphere (pluses), fixed day 60 atmosphere (sideways triangles), and fixed day 90 (permanent solstitial) atmosphere (circles).

5.5 The equatorial temperature minimum and equatorial waves

As mentioned above, an interesting feature of the climatology of the seasonally varying atmosphere (Fig. 5.2) is the mid-tropospheric minimum in equatorial temperatures. Another view of this feature is seen in Fig. 5.13, which shows the temperature difference between the 23.5° $\phi_{\max}$ atmosphere and the control equinox atmosphere. The largest magnitude change is a considerably cooler equatorial surface, with warmer surface temperatures being spread to higher latitudes when the peak in temperature forcing is made to migrate between ±23.5°. The largest feature, however, is a broad region of warmth (2-3 K warmer, relative to the control) in the mid-troposphere of the subtropics and extratropics, that manifests itself as an equatorial minimum in temperatures (Fig. 5.2b).

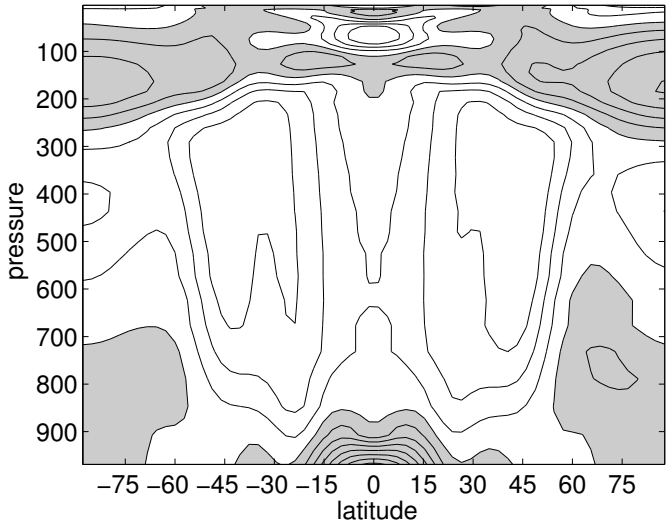


Figure 5.13: Difference in climatological temperatures between the 23.5° $\phi_{\max}$ and the control equinox atmospheres. Contour intervals 1 K, shaded regions negative.

What causes the equatorial minimum? We start with the thermodynamic budget, following J. M. Wallace (2012) and modified for a dry Held-Suarez physics dynamical core:

$$\frac{\partial \overline{T}}{\partial t} = \underbrace{-\frac{\overline{v}}{a}\frac{\partial \overline{T}}{\partial \phi}}_{\text{Mean flow merid. adv.}} - \underbrace{\overline{\omega}\left(\frac{\partial \overline{T}}{\partial p} - \frac{\kappa \overline{T}}{p}\right)}_{\text{Mean flow vert. adv. + adiabatic}} - \underbrace{\frac{1}{a\cos\phi}\frac{\partial}{\partial \phi}\overline{v'T'}\cos\phi}_{\text{Merid. eddy transport}} \tag{5.5}$$

$$- \underbrace{\frac{\partial}{\partial p}\overline{\omega'T'} + \frac{\kappa}{p}\overline{\omega'T'}}_{\text{Vert. eddy transport}} + \underbrace{\frac{\overline{T} - T_{\text{eq}}}{\tau}}_{\text{Newtonian cooling}} . \tag{5.6}$$

With notation the same as used in previous sections. Fig. 5.14 shows the second and third terms from Eq. 5.5, $\overline{\omega}\left(\frac{\partial \overline{T}}{\partial p} - \frac{\kappa \overline{T}}{p}\right)$, the vertical advection of temperature by the mean flow and adiabatic cooling/heating for the permanent equinox control and the 23.5° seasonally varying atmosphere. These two terms are the dominant terms in the subtropical and tropical troposphere above 850mb (not shown), and, as shown in Fig. 5.14, they mostly cancel each other out. In the equinoctial atmosphere, Fig. 5.14a, there is upper troposphere warming centered at 30° and weak cooling over the equator extending to 15°. This changes in the seasonally varying atmosphere, Fig. 5.14b, with warming extending well towards the upper

equatorial troposphere. The equatorial cooling near 150 mb is considerably stronger, cooling at a rate of more than 2 K/day. This combination of greater off-equatorial heating and equatorial cooling in the upper troposphere appears to lead directly to the equatorial minimum in temperatures (compare Fig. 5.1b to 5.2b).

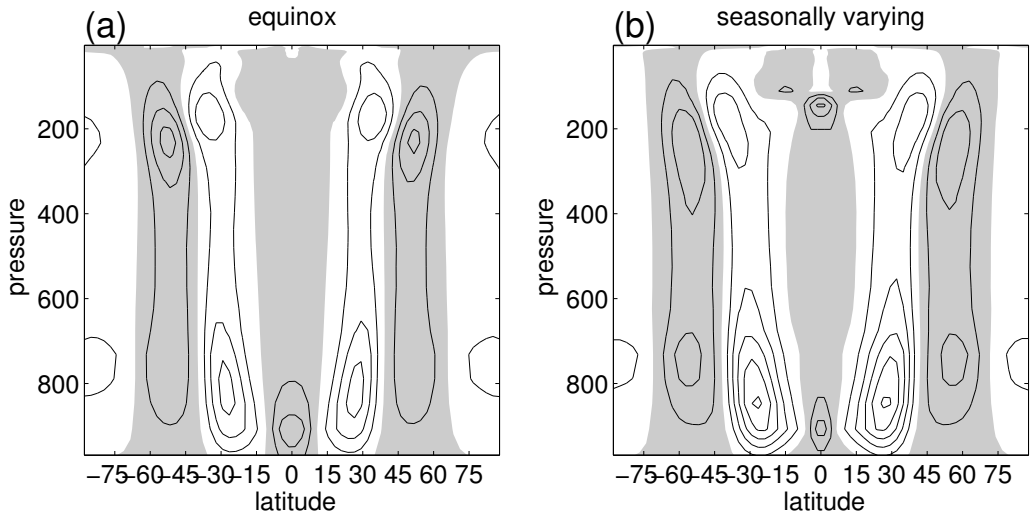


Figure 5.14: $\overline{\omega}\left(\partial\overline{T}/\partial p - \kappa\overline{T}/p\right)$ for (a) the permanent equinox control atmosphere and (b) the 23.5° $\phi_{\max}$ atmosphere. Contour levels 0.25 K/day with shaded regions negative.

The equatorial upper troposphere cooling is balanced by eddies. Fig. 5.15 shows $(a\cos\phi)^{-1}\partial/\partial\phi(\overline{v'T'}\cos\phi)$, the meridional eddy temperature flux divergence, in the solstitial atmopshere. Aside from the large high latitude winter hemisphere warming and subtropical cooling caused by baroclinic eddies the largest signal is a small dipole in the equatorial upper troposphere. The tropical eddy heating is strongest in the deep tropics of the winter hemisphere while the cooling is centered at 15° in the winter hemisphere, reaching magnitudes over 1.25 K/day.

We can directly compare the spectral signature of the eddy heat transport to that of the eddy momentum transport by calculating $(a\cos\phi)^{-1}\partial/\partial\phi(\overline{v'T'}\cos\phi)$ in $\omega - k$ space. Fig. 5.16 shows eddy heat transport in $\omega - k$ space for the varying atmosphere and three fixed day atmospheres, and should be directly compared to Fig. 5.11. Similar to the $\omega - k$

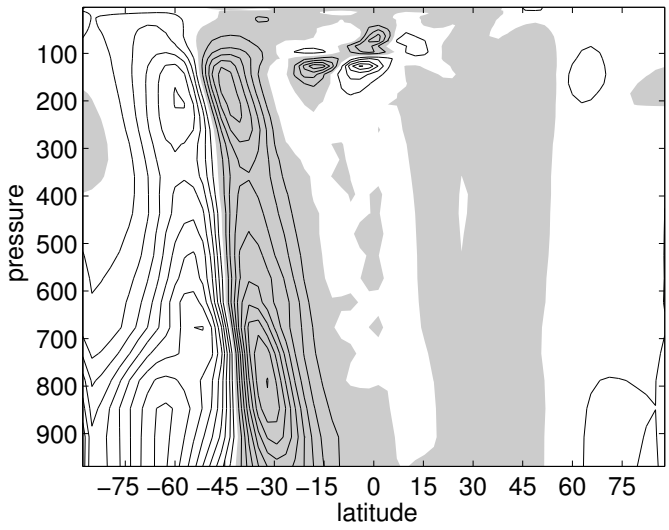


Figure 5.15: $(a\cos\phi)^{-1}\partial/\partial\phi(\overline{v'T'}\cos\phi)$ at 144 mb in the permanent solstice atmosphere. Contour intervals 0.25 K/day with shaded regions negative.

structure of $\mathcal{S}$, signals corresponding to Kelvin waves, $n = 1$ equatorial Rossby waves, and easterly waves can clearly be seen. The fixed day 25 atmosphere has very weak eddy heating (~ 0.1 K/day) that is mostly due to slow Kelvin waves and some easterly waves. The fixed day 60's eddy heat is mostly due to the $k = -2$ equatorial Rossby wave while the solstitial fixed day 90 is dominated by easterly waves.

5.6 Seasonal instability

To characterize instability in the seasonal and equinox atmospheres we use the quasi-geostrophic potential vorticity gradient as defined by Edmon et al. (1980):

$$\overline{q}_\phi = 2\Omega\cos\phi - \frac{\partial}{\partial\phi}\left[\frac{1}{a\cos\phi}\frac{\partial}{\partial\phi}(\overline{u}\cos\phi)\right] + f\frac{\partial}{\partial p}\left(\frac{\partial\theta/\partial\phi}{\partial\theta/\partial p}\right). \tag{5.7}$$

$\overline{q}_\phi$ acts as an approximate sufficient condition for instability. Where $\overline{q}_\phi = 0$, instability can develop. A vertical zero line of $\overline{q}_\phi$ is taken to be barotropic instability and a horizontal zero line is taken to indicate baroclinic instability. $\overline{q}_\phi$ for the permanent equinox control and the

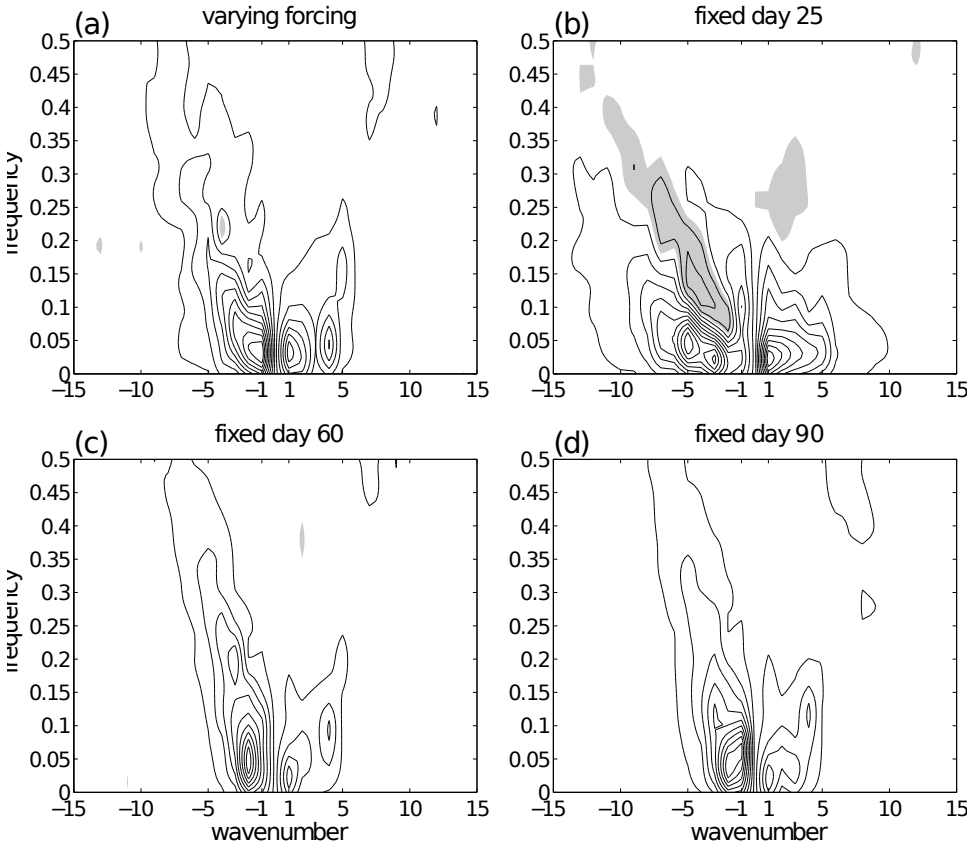


Figure 5.16: Meridional eddy temperature flux divergence decomposed into wavenumber-frequency space at -1.3° and a specific pressure level for the 23.5° $\phi_{\max}$ atmosphere both seasonally varying and fixed at days 25, 60, and 90. (a) Seasonally varying atmosphere, eddy heating of 0.22 K/day at 144 mb. (b) Fixed day 25 atmosphere, eddy heating of 0.09 K/day at 163 mb. (c) Fixed day 60 atmosphere, eddy heating of 0.72 K/day at 127 mb. (d) Fixed day 90 atmosphere, eddy heating of 1.2 m/s/day at 127 mb. Contour intervals arbitrary with shaded regions negative.

the 23.5° $\phi_{\max}$ atmospheres is shown in Fig. 5.17. Both atmospheres have broad bands of extratropical instability that correspond to midlatitude baroclinic instability. The primary difference between the two atmospheres is a small region with $\overline{q}_\phi = 0$ in the deep tropics centered at 200 mb. This region of $\overline{q}_\phi = 0$ is a result of the strong meridional shear of the tropical easterlies in the seasonally varying atmosphere (Fig. 5.2) and clearly corresponds to the eddy momentum and heat transports discussed above.

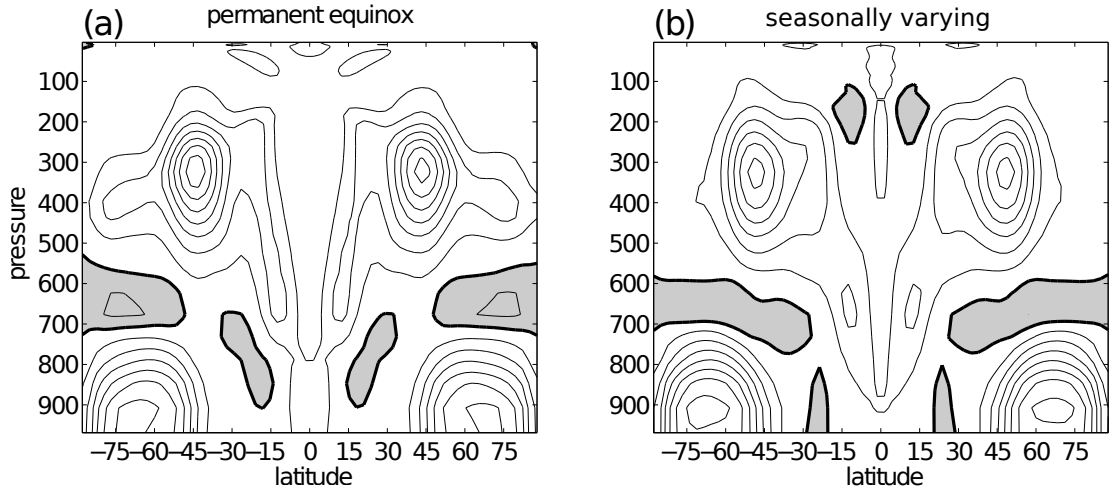


Figure 5.17: Annual mean gradient of quasi-geostrophic potential vorticity in the (a) permanent equinox control atmosphere and (b) the 23.5° $\phi_{\max}$ atmosphere. Contour intervals 2Ω with shaded regions negative and the zero line bolded

Fig. 5.18 shows the annual cycle of zonal mean zonal wind and $\overline{q}_\phi$ at 144 mb. Fig 5.18 should be directly compared to the 144 mb momentum balance in Fig. 5.7. Near the solstice, the Coriolis force and meridional advection of momentum act to strongly decelerate the summer hemisphere. There are strong easterlies in the summer hemisphere tropics until roughly 45 days after solstice. At this point two things start to happen. First, the Hadley cell migrates close enough to the equator that the mean vertical motion acting against a strong easterly shear (Fig. 5.7) acts to accelerate the near-equatorial summer hemisphere winds. Second, the strong easterly winds have strong easterly shear that leads to barotropic instability (Fig. 5.18). This barotropic instability manifests itself as equatorial Rossby waves, Kelvin waves, and easterly waves (Fig. 5.11) that accelerate the summer hemisphere. This eddy acceleration ends at the equinox and the entire process starts over again in the opposite hemisphere.

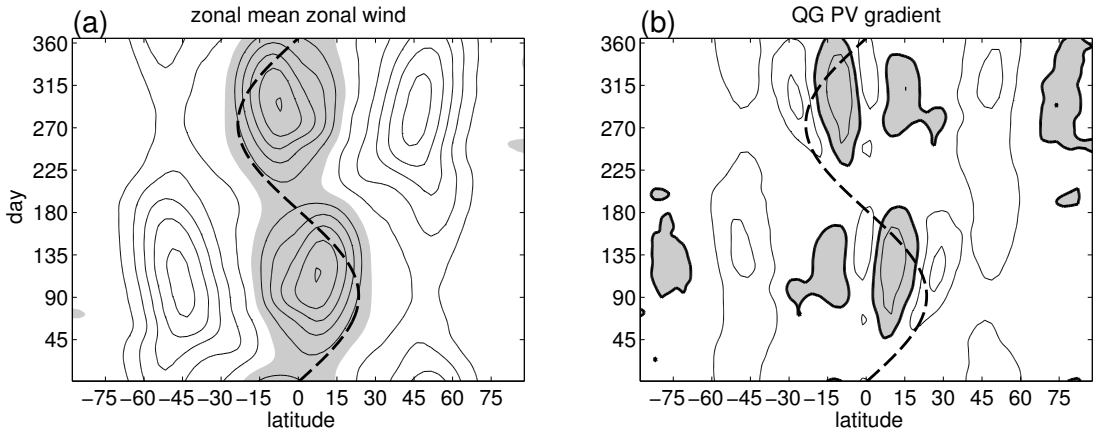


Figure 5.18: Seasonal fields from the 23.5° $\phi_{\max}$ atmosphere at 144 mb. (a) Zonal mean zonal wind. Contour intervals 10 m/s with shaded regions negative. (b) Gradient of quasi-geostrophic potential vorticity. Contour intervals 2Ω with shaded regions negative and the zero line bolded.

5.7 Conclusions

We have described and attempted to understand the dynamics of a dry dynamical core forced with a seasonally varying Newtonian cooling profile. We explored the momentum balance of the seasonally varying atmosphere and showed that eastward acceleration of the deep tropics by equatorial waves is key to counteracting the strong westward acceleration due to the solstitial Hadley cell. We found that a variety of dynamically active waves occur in the equatorial tropics — Kelvin waves, $n = 1$ equatorial Rossby waves, and easterly waves (equatorial Rossby waves advected by a mean easterly flow). The strong seasonality of the Hadley cell was shown to lead to a temperature minimum at the equator. This temperature minimum is in part balanced by the same equatorial waves that transport momentum to the deep tropics. Lastly, we looked at the seasonality of instability and found that barotropic instability occurred near the solstices when the tropical easterlies were at their strongest. This instability coincides with and likely explains the excitation of equatorial waves responsible for both eddy momentum and eddy heat transport towards the equator.

Mitchell et al. (2014) showed that in idealized planetary atmospheres, superrotation was the preferred state in atmospheres with weak seasonality and large thermal Rossby numbers (small planetary radii). This superrotation is due to increased tropical wave activity that is the result of a global barotropic instability (Wang and Mitchell, 2014). Mitchell et al. (2014) showed that this instability is strongest during the equinox. As a followup to Mitchell et al. (2014) we wanted to explore the tropical dynamics in a more Earth-like case (thermal Rossby number $R_{oT} \sim 10^{-2}$). We found that tropical eddies are actually preferred at the solstices, not the equinoxes, of the Earth-like case and that this eddy activity primarily manifests itself as $n = 1$ equatorial Rossby waves rather than the Kelvin waves of Mitchell and Vallis (2010), Potter et al. (2014), Pinto and Mitchell (2014), Mitchell et al. (2014), and Wang and Mitchell (2014). The work done in this chapter highlights interesting correspondences and differences between the highly seasonal, small thermal Rossby number atmospheres and weakly seasonal, large thermal Rossby number atmospheres and the transition between these two extremes will hopefully be explored in future work.

Chapter 6

Superrotation and tropical variability in a full-physics AGCM

6.1 Introduction

Recent work with full-physics atmospheric general circulation models (AGCMs) has found a connection between warmer climates, strong tropical eddies, and superrotation. Using a GFDL aquaplanet AGCM with AM1 physics, Lee (1999) found that the Madden-Julian oscillation provided a significant eddy momentum convergence near the equator, and when the model underwent moderate warming the MJO strengthened and the atmosphere began to weakly superrotate. Huang et al. (2001) studied gradual global warming runs in the Canadian Centre for Climate Modelling and Analysis coupled model and found that as CO_2 was increased equatorial upper atmosphere easterlies slowly gave way to weak westerlies. The authors speculated that increases in the model's MJO were partly responsible. Arnold (2014) showed that increased fixed sea surface temperatures in a super-parameterized version of NCAR's Community Atmosphere Model (CAM) 3.5 led to a strengthened MJO and moderate superrotation. In a more extreme case Caballero and Huber (2010) (from here on CH10) doubled CO_2 five times from preindustrial levels to almost 9000 ppm to simulate

extreme hothouse climates in the 3rd generation of the CAM model coupled to a slab ocean. The authors showed a monotonic relationship between surface temperatures and tropical upper troposphere eddy activity. Past a critical surface temperature/CO_2 concentration the atmosphere began to superrotate and at extremely hot equatorial surface temperatures ($\sim 47^\circ$ C) the entire atmospheric general circulation changed, with strong eddy activity concentrated over the equator rather than in midlatitudes and strong westerly winds ($\sim$ 33 m/s) lying over the equator. CH10 showed that a strong MJO-like tropical mode was responsible for the superrotation. It remains unclear, however, why the model's MJO was so strong in CH10's hothouse runs.

We have two goals in this chapter. First, we want to verify that the superrotation and extreme seasonality-induced tropical variability results of Chs. 2, 4, and 5 were not significantly impacted by the extremely simplified physics of the dry dynamical core with Held-Suarez physics. Our second goal is to investigate in more detail hothouse superrotation in the line of CH10 and attempt to provide an explanation for why superrotation is a preferred state of hothouse atmospheric models. The remainder of this chapter is organized as follows. In Section 6.2 we briefly describe the model. Section 6.3 looks at the moist model's control run zonal mean climatology and tropical eddy diagnostics. Section 6.4 looks at the tropical variability and momentum budget of the moist model with extreme seasonality. Section 6.5 investigates the differences in the small radius, large thermal Rossby number atmosphere when simulated in a moist model. Lastly, Section 6.6 attempts to replicate the hothouse results of Caballero and Huber (2010) and investigates the differences between the control and strongly superrotating model runs.

6.2 Model description

We use GFDL's finite volume cubed sphere model with AM2.1 physics coupled to a slab ocean (Delworth et al., 2006; Freidenreich, 2004; Adcroft et al., 2004). The model has C48

horizontal resolution with grid boxes approximately 200 km on a side. The model outputs fields onto cubed sphere faces which are then converted to a latitude-longitude grid with 2° resolution. We performed all of our integrations with both 32 and 47 pressure levels, and found that the warmer atmospheres require extra vertical resolution to properly resolve the tall circulation which reaches above 100 mb in the hottest cases. We therefore utilize the 47 level runs for analysis of the hottest atmospheres ($S_0 = 1550, 1575, 1600$, as described below) in section 6.6 and use the 32 level runs in all other integrations. Relative to the mid-troposphere the model has extra vertical resolution at the top and bottom of the domain. We have chosen to make the top three layers of the model sponge layers since the model has unrealistic eddy activity at the uppermost layers when only the uppermost layer is a sponge.

Carbon dioxide is set at 300 ppm. There is no diurnal cycle in solar forcing and the solar forcing is kept at permanent daily mean equinox except in the seasonally varying runs. The model uses a relaxed Arakawa-Schubert scheme (Moorthi and Suarez, 1992) to parameterize convective clouds. Cloud microphysics are parameterized following Rotstayn (1997) and Rotstayn et al. (2000) and falling precipitation is tracked following Jakob and Klein (2000). Lastly, all integrations discussed here have a globally uniform 20 meter slab ocean.

6.3 Control run

Due to details of the AM2.1 radiation calculations we induce hothouse warming by changing the solar constant rather than the CO_2 concentration as in CH10. Therefore we define our control to have a solar constant of $S_0 = 1400$ W/m^2 and refer to the control as the $S_0 = 1400$ W/m^2 atmosphere. Climatology is calculated from the last 4 years of a 16 year run. The control run zonal mean climatological values for mass streamfunction, zonal winds, temperature, and $[\overline{u'v'}]\cos\phi$ are shown in Fig. 6.1. Compared to the dry Held-Suarez dynamical core (Fig. 2.1) the control aquaplanet has a stronger Hadley cell, slightly cooler temperatures and a more pronounced upper troposphere cold point, and slightly stronger

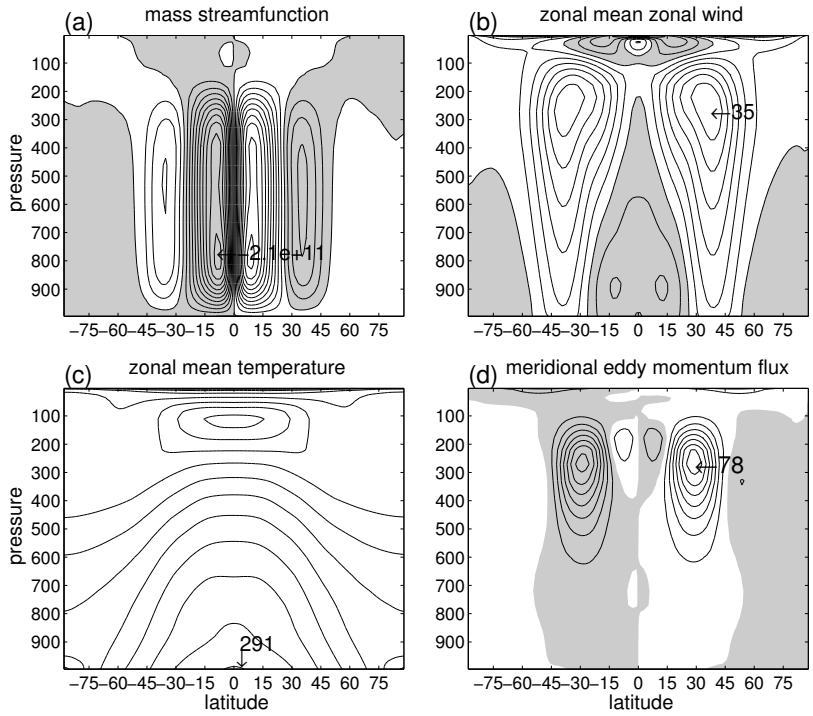


Figure 6.1: Time mean fields for the control aquaplanet atmosphere. (a) Zonal mean mass stream function, contour interval $2x10^{10}$ kg s^{-1}. (b) Zonal mean zonal winds, contour interval 5 m/s. (c) Zonal mean temperature, contour interval 10 K. (d) $[\overline{u'v'}]\cos\phi$, contour interval 10 m^2/s^2. Shaded areas negative valued. Largest values highlighted.

and equatorward jets. The biggest difference from the perspective of the zonal momentum balance, however, is the strong eddy activity seen between 400 and 100 mb equatorwards of 15°. This eddy momentum flux leads to a peak acceleration of 3.1 m/s/day centered at the equator. This is a fundamental departure from the dry dynamical core which has no distinct tropical eddy momentum flux convergence. The addition of new physics, with moisture likely being the key, allows for very different dynamics.

6.3.1 Spectral diagnostics

Details of the tropical variability can be seen in the spectral diagnostic plots in Fig. 6.2. The Wheeler-Kiladis diagram varies in some details compared to the dry model calculations in Ch. 2 and Ch. 4. The calculation is done at a higher pressure level to account for the deeper

tropopause in the aquaplanet simulations and zonal wind is used rather than geopotential height. We do not split the variability into meridionally symmetric and asymmetric modes but rather take the entire field and divide by a smoothed background variability to get Fig. 6.2a. As in the dry model there are large signals for Kelvin wave frequencies, though now they have varying equivalent depths between 12 and 40 m, rather than centering around the 40 m line. There is again a clear Rossby-Haurwitz signal on the westward side of the plot. However, unlike the dry model, there is an extremely strong signal near wavenumbers 1-3 and very low frequencies, approximately 0.03 day^{-1}. This variability seems to deviate from that of the Kelvin wave branch and is suggestive of the MJO's spectral signature (e.g. Wheeler and Kiladis, 1999).

The prominence of this low frequency, wavenumber-1 variability can also be seen in Fig. 6.2b which plots $\mathcal{S}$ in $\omega - k$ space. By far the strongest feature is an acceleration at low frequency and eastward wavenumber-1. There is additionally a much smaller signal at westward wavenumber-1 and low frequencies, perhaps corresponding to n = 1 equatorial Rossby waves that do not show up in Fig. 6.2a. Fig. 6.2b corresponds quite closely to the corresponding figure for the NCEP-II Reanalysis (2.13b). This again suggests that the low frequency, low eastward wavenumber variability in the aquaplanet model is the model's version of the MJO.

6.4 Seasonal atmospheres

As in the dry model, extreme seasonality drastically changes the zonal mean climatology. Fig. 6.3 shows the climatology for the moist atmosphere with an obliquity of 18° and a 365 day year. The Hadley cell has a complicated structure in the time mean since it is the superposition of seasonal Hadley cells. The equatorial easterlies are much stronger and the jets have moved poleward and weakened. Equatorial surface temperatures are colder while extratropical temperatures are increased relative to the control. There is a pronounced equa-

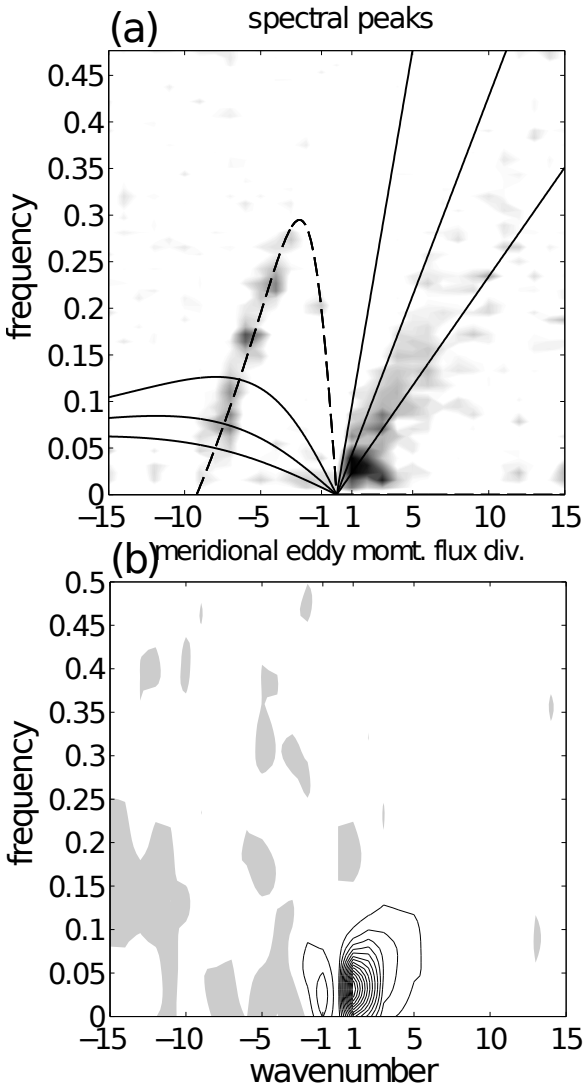


Figure 6.2: Tropical spectral diagnostics in the control $S_0 = 1400$ atmosphere at 178 mb. (a) Wheeler-Kiladis diagram for zonal wind. Solid lines are dispersion relations for ($k < 0$) $n = 1$ equatorial Rossby and ($k > 0$) Kelvin waves with equivalent depths $H = 12, 40, 200$ m. Dashed line is approximate dispersion relation for Rossby-Haurwitz wave with equivalent depth of 12 km and Doppler-shifting wind of 10 m/s. (b) $\mathcal{S}$ in $\omega - k$ space at the equator. Contour intervals arbitrary, shaded regions negative.

torial temperature minimum above 800mb. In the mean the extratropical eddy momentum flux is weaker than that of the control but the tropical eddy source is of roughly the same magnitude.

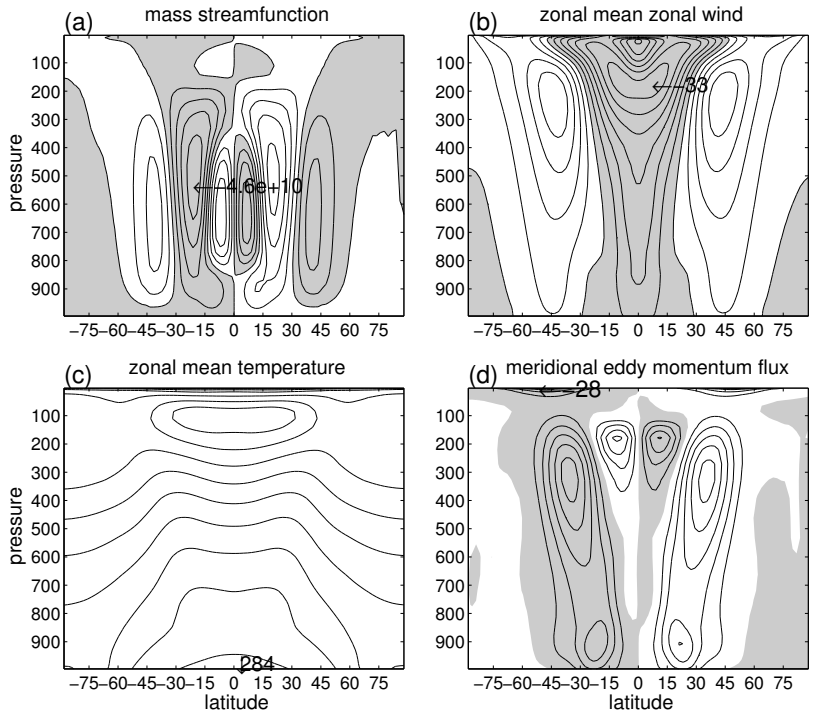


Figure 6.3: Time mean fields for the 18° obliquity atmosphere. (a) Zonal mean mass stream function, contour interval $1x10^{10}$ kg s^{-1}. (b) Zonal mean zonal winds, contour interval 5 m/s. (c) Zonal mean temperature, contour interval 10 K. (d) $[\overline{u'v'}]\cos\phi$, contour interval 5 m^2/s^2. Shaded areas negative valued. Largest values highlighted.

The seasonality of the free-troposphere momentum budget at 178 mb is shown in Fig. 6.4 (see Ch. 5, Eq. (1)). Fig. 6.4a shows the zonal mean zonal wind, with the latitude of peak insolation overlaid. Equatorial easterly winds peak slightly after the solstices and fall to nearly zero roughly 45 days after the equinox. The dominant balance is between the Coriolis acceleration and the mean flow meridional momentum advection in the winter hemisphere. The strongest tropical eddies occur in the summer hemisphere and, along with the mean flow meridional momentum advection, balance the strong deceleration by the equatorward branch of the upper Hadley cell. Both the eddy and mean flow vertical terms have very small

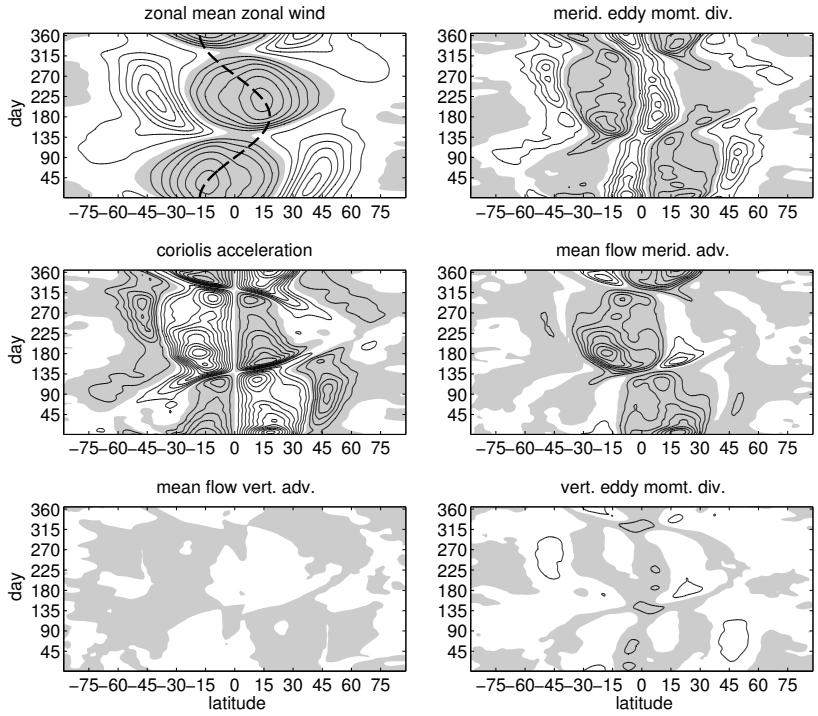


Figure 6.4: Smoothed seasonal cycle of (a) zonal mean zonal wind and (b)-(f) the five terms on the righthand side of the free troposphere momentum budget, Eq. 5.1 at 178 mb in the 18° obliquity atmosphere. Contour intervals 1 m/s/day, shaded regions negative.

contributions. There is a strong similarity between the moist and dry seasonal atmospheres (compare Fig. 6.4 to Fig. 5.7). The Coriolis acceleration and mean flow meridional advection are the dominant terms in both atmospheres. In both dry and moist atmospheres tropical eddies peak after the solstices in reaction to large summer hemisphere deceleration by the Coriolis force. Unlike the moist model, which has a year-round tropical eddy source, the dry model's tropical eddies disappear near the equinoxes.

$\mathcal{S}$ in $\omega - k$ space as a function of seasonality is shown in Fig. 6.5. As discussed above, the control atmosphere is dominated by the model's MJO-like variability. As the obliquity is increased, the eastward signal decreases and the westward signal — which is only hinted at in the control atmosphere — becomes dominant. This signal seems to be a wavenumber-1 equatorial Rossby wave that is slightly Doppler-shifted to higher frequencies in the obliquity 23.5° atmosphere. One of the prime differences in the general circulation of the dry and moist

atmospheres is highlighted in this figure. In the dry atmosphere, there is no equatorial eddy momentum convergence for equinoctial forcing. The dry atmosphere requires seasonality to generate dynamically active tropical eddies. However, the moist atmosphere with either equinoctial forcing or seasonally varying forcing has very strong tropical eddies.

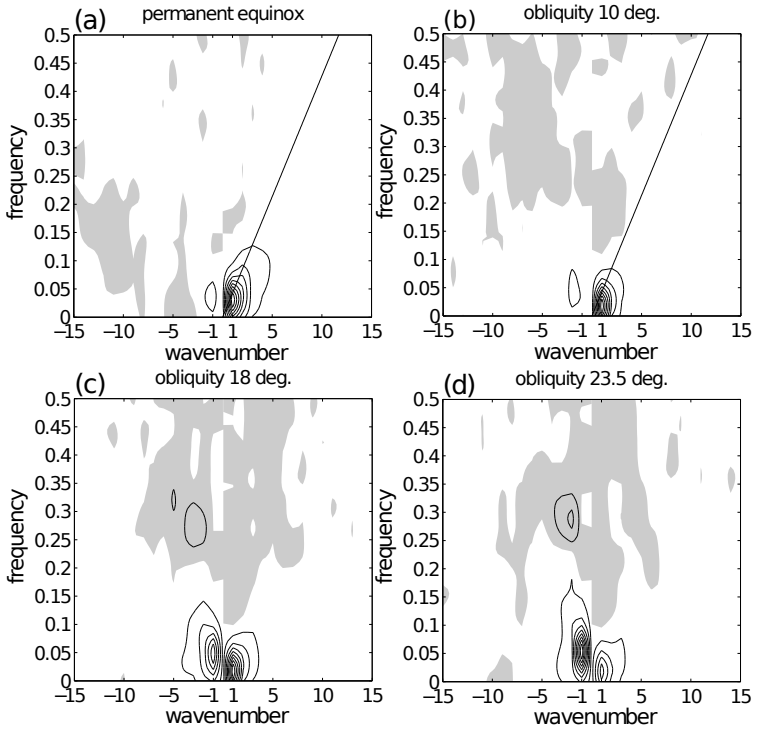


Figure 6.5: Meridional eddy momentum flux divergence decomposed into wavenumber-frequency space at the equator and a specific pressure level for the moist atmosphere with varying obliquities. (a) The control atmosphere at 178 mb with an acceleration of 3.1 m/s/day. (b) The 10° obliquity atmosphere at 221 mb and an acceleration of 3 m/s/day. (c) The 18° obliquity atmosphere at 178 mb and an acceleration of 2.3 m/s/day. The 23.5° obliquity atmosphere at 178 mb and an acceleration of 2 m/s/day. Contour intervals arbitrary, shaded regions negative. Solid lines overlaid show the dispersion relation for an equatorial Kelvin wave with equivalent depth of 40 m.

6.5 Small radius superrotation in a moist atmosphere

We replicate the $R_o = 1$, (planetary radius $a = 9e5$ m) run studied extensively in Ch. 2 using the moist model. Fig. 6.6 shows the $a = 9e5$ m atmosphere climatology and should

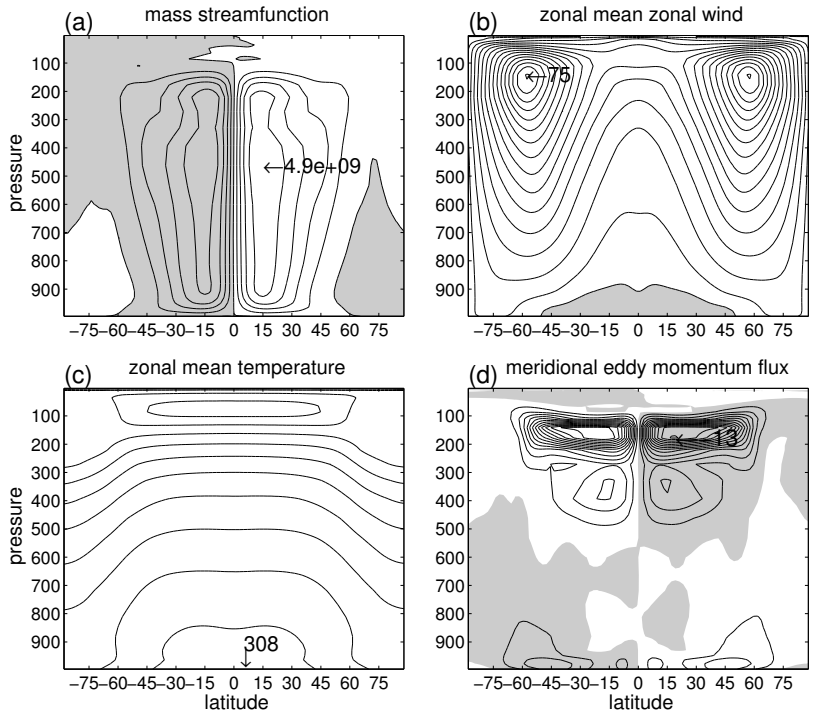


Figure 6.6: Time mean fields for the $a = 9e5$ m atmosphere. (a) Zonal mean mass stream function, contour interval $1x10^9$ kg s^{-1}. (b) Zonal mean zonal winds, contour interval 5 m/s. (c) Zonal mean temperature, contour interval 10 K. (d) $[\overline{u'v'}]\cos\phi$, contour interval 1 m^2/s^2. Shaded areas negative valued. Largest values highlighted.

be compared to Fig. 2.11, the dry model $a = 9e5$ m climatology. Like the dry model, the moist model's Hadley cell and hemispheric jets expand in latitude as the radius is decreased. Unlike the dry model the moist atmosphere's jets, Hadley cells, and eddy activity do not get pushed into the lower troposphere as the radius is decreased. Also entirely different from the dry model is the form of the eddy climatology. Rather than two distinct tropical and extratropical eddy regions as in the dry model, the moist model's eddy climatology is almost entirely dominated by the equatorial mode that drives superrotation. Despite these large differences, the greatest similarity between the two $a = 9e5$ m atmospheres is strong superrotation, with the moist atmosphere having 25 m/s westerly winds overlying the equator.

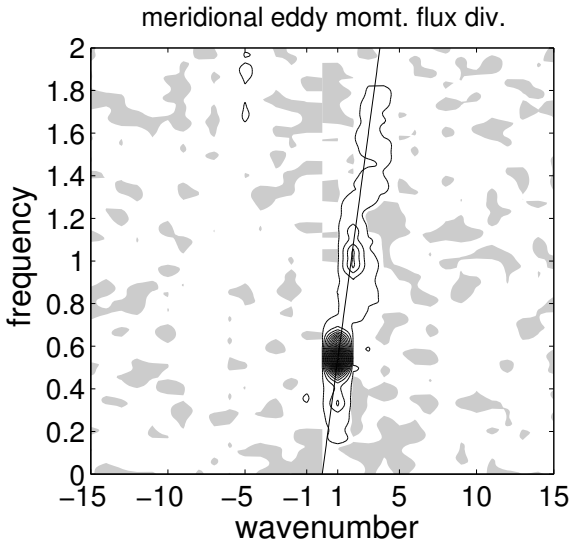


Figure 6.7: $\mathcal{S}$ for the $a = 9e5$ m atmosphere at 141 mb. Acceleration at this point 8.3 m/s/day. Contour intervals arbitrary, shaded regions negative. The solid lines shows the theoretical dispersion relation for a Kelvin wave with an equivalent depth of 125 m.

Fig. 6.7 shows $\mathcal{S}$ in $\omega - k$ space in the upper equatorial troposphere of the $a = 9e5$ m atmosphere. Overlaid is a dispersion line for Kelvin waves with equivalent depth 125 m. This dispersion line clearly follows the acceleration in the $\omega - k$ plane through wavenumber-1 and -2 Kelvin waves, with hints of higher wavenumbers also present. This is counter to the moist control run (Fig. 6.2b) which is dominated by the model's MJO and some slower Kelvin waves. It is also very similar to the equivalent figure for the dry model, which clearly showed wavenumbers 1-3 Kelvin waves falling along a single line of acceleration in $\omega - k$ space (Fig. 2.14b).

Similiarly, Fig. 6.8 shows the phase speed cospectra of $\mathcal{S}$ as a function of latitude. Just as in the dry model (Fig. 2.15), a bullseye of equatorial acceleration is clearly associated with extatropical deceleration (dashed line is of constant angular frequency). This again suggests a coupled tropical-extratropical mode, just like the dynamic which drove superrotation in the dry $a = 9e5$ m atmosphere.

The structure of the dominant eastward wavenumber-1 mode is shown in Fig. 6.9. This picture was created by filtering equatorial zonal winds at a single pressure level for eastward

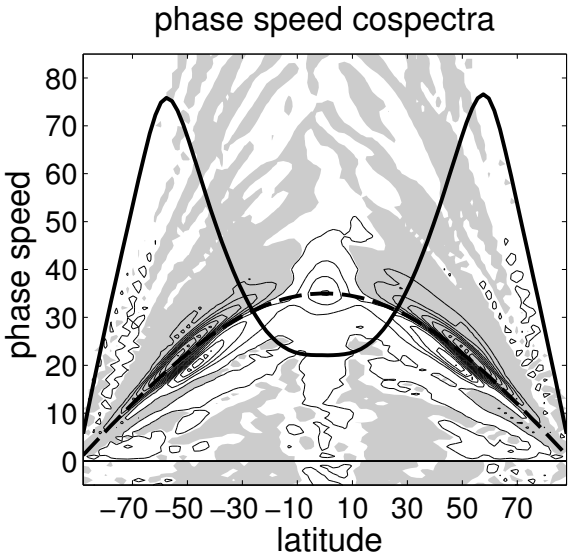


Figure 6.8: Contours of $\mathcal{S}$ as a function of phase speed and latitude at 141 mb for the $a = 9e5$ m atmosphere. Dark line shows the time mean zonal mean zonal wind at the same pressure level. Shaded values negative. Contour intervals arbitrary. The dashed line shows the angular frequency corresponding to the peak Kelvin wave speed of 35 m/s (corresponding to equivalent depth of 125 m) at the equator.

wavenumber-1 variability to create a time series that was regressed onto geopotential height, horizontal winds, and precipitation. Despite the moist control atmosphere's tropics being dominated by an MJO signal, this is clearly a Kelvin wave. The tropical geopotential height field has a maximum in the tropics, unlike the MJO which has, similar to the equatorial Rossby wave, a geopotential height maximum in the subtropics (e.g. Kiladis et al., 2005). The tropical winds are for the most part completely zonal. Easterly winds overlie negative height anomalies while westerly winds overlie positive anomalies, just as in a Kelvin wave. The precipitation is closely coupled to the wave, with positive precipitation anomalies associated with regions of upper level divergence and negative precipitation anomalies associated with regions of upper level convergence. The inability of the extratropical wind field to sync with the height field may be an issue with the model, which outputs height onto fixed levels rather than model levels. While aspects of the general circulation in the $a = 9e5$ m moist model

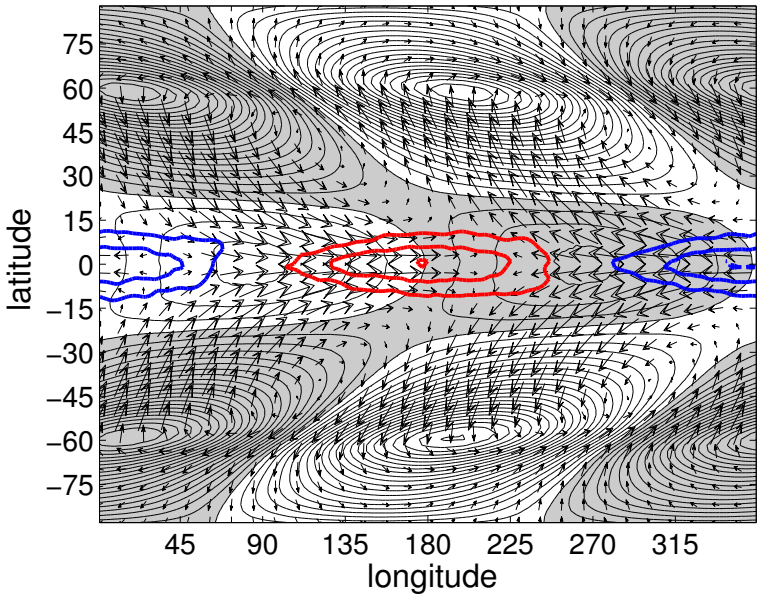


Figure 6.9: Wavenumber-1 and 0.34-0.75 1/day frequency filtered equatorial 141 mb zonal wind variability regressed onto global fields at 141 mb. Arrows show horizontal wind, maximum wind vector 7 m/s. Contours show geopotential height with contour interval 1 m, shaded regions negative. Shaded contours show precipitation at $\pm 3, 6$ and 9 mm/day.

are clearly different from that of the dry model, the transition to a strongly superrotating atmosphere dominated by Kelvin waves is entirely similar.

6.6 The transition to a hot, superrotating atmosphere

As mentioned above, we recreate the extreme hothouse runs of CH10 by increasing the model's solar constant S_0 rather than atmospheric CO_2. Similar to CH10's Fig. 1, we plot deep tropical temperature and 0-300 mb averaged zonal wind, standard deviation of zonal wind, and $\mathcal{S}$ as a function of S_0 in Fig. 6.10. Deep tropical surface temperatures T_{se} increase roughly linearly from the control, $T_{se} = 20\,^{\circ}\mathrm{C}$ to $S_0 = 1550$, with $T_{se} = 34\,^{\circ}\mathrm{C}$. Between $S_0 = 1550$ and $S_0 = 1600$ the T_{se} curve accelerates, with $T_{se} = 49\,^{\circ}\mathrm{C}$ for $S_0 = 1600$. This accelerated warming is accompanied by a dramatic increase in upper atmosphere zonal mean zonal winds. Between the control and $S_0 = 1550$ the upper atmosphere winds stay roughly constant at around 1-2 m/s. The winds gain speed after that, reaching 5 m/s for

$S_0 = 1575$ and 35 m/s at $S_0 = 1600$. The increase in wind speed co-occurs with an increase in upper atmosphere variability. The standard deviation of zonal wind increases from roughly 2 m/s between the control and $S_0 = 1550$ W/m^2 to nearly 7 m/s in the $S_0 = 1600$ W/m^2 atmosphere. $\mathcal{S}$ more than doubles between the control (0.9 m/s/day) and $S_0 = 1600$ W/m^2 (2.3 m/s/day) atmospheres.

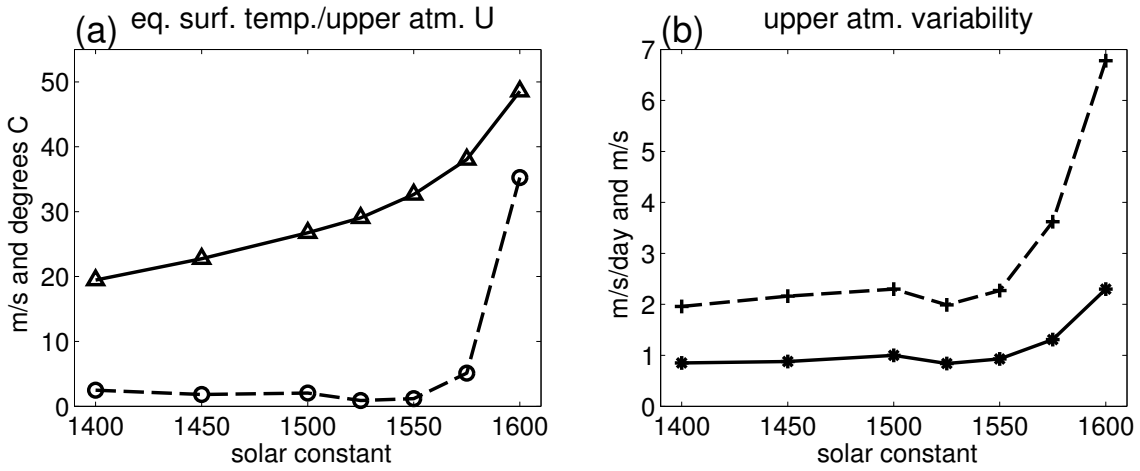


Figure 6.10: Temperature, zonal wind, and eddy fields in the parameter sweep of varying solar constant. (a) Equatorial surface temperature (solid, triangles) and 0-300 mb $5S - 5N$ latitude averaged zonal mean zonal wind (dashed circles). (b) Standard deviation of 0-300 mb and $5S-5N$ latitude zonal mean zonal wind (dashed, pluses) and 0-300 mb and $5S-5N$ latitude averaged $\mathcal{S}$ (solid, asterisks).

Changes in equatorial precipitation as a function of solar constant are shown in Fig. 6.11. Up to $S_0 = 1575$, the equatorial precipitation increases almost linearly from 7.5 mm/day to 16 mm/day at $S_0 = 1575$. Total precipitation then drops at $S_0 = 1600$ to 14 mm/day. Total precipitation is divided between the contributions from the convective cloud scheme (dashed, circles) and that from the stratiform cloud scheme (dashed, triangles). The rise in total precipitation up to $S_0 = 1550$ is due to increases in both convective and stratiform precipitation, though the convective component is dominant. After $S_0 = 1550$ convective precipitation decreases to 4 mm/day at $S_0 = 1600$. Stratiform precipitation increases from almost zero in the control to over 10 mm/day in the $S_0 = 1600$ atmosphere.

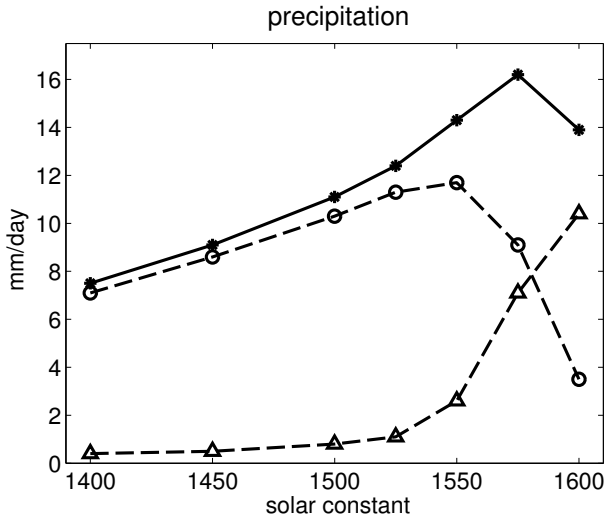


Figure 6.11: Total (solid, asterisks), convective (dashed, circles), and stratiform (dashed, triangles) precipitation averaged between $5S - 5N$ latitude as a function of solar constant.

The zonal wind, eddy, and precipitation summaries above show a marked transition from the $S_0 = 1550$ atmosphere to the $S_0 = 1600$ atmosphere. Climatologies for these two atmospheres are shown in Figs. 6.12 and 6.13. The effects of extreme warming are apparent in the $S_0 = 1550$ W/m^2 climatology, with a wider, taller, and somewhat weaker Hadley cell expanding past 30° and pushing well above 200 mb. The hemispheric jets are taller and much stronger, with the jet maximum increasing to 50 m/s from 35 m/s in the control. Both midlatitude eddies and tropical eddies are strengthened in the warmer atmosphere.

The strongly superrotating $S_0 = 1600$ W/m^2 atmosphere, seen in Fig. 6.13, is entirely different from the control and the $S_0 = 1550$ W/m^2 atmospheres. There is no longer a well-defined tropopause and the tropospheric circulation is pushed to the top of the domain. The Hadley cell stretches well above 100mb and is almost halved in strength. The Hadley circulation is no longer strongest in the lower atmosphere but peaks at 650 mb. The subtropical and eddy-driven jets are now well separated, with the barotropic eddy-driven jet sitting near 73° and the subtropical jet lying at 24° and peaking at 25 mb. The most dramatic difference, however, is the dominance of tropical eddies and the almost complete

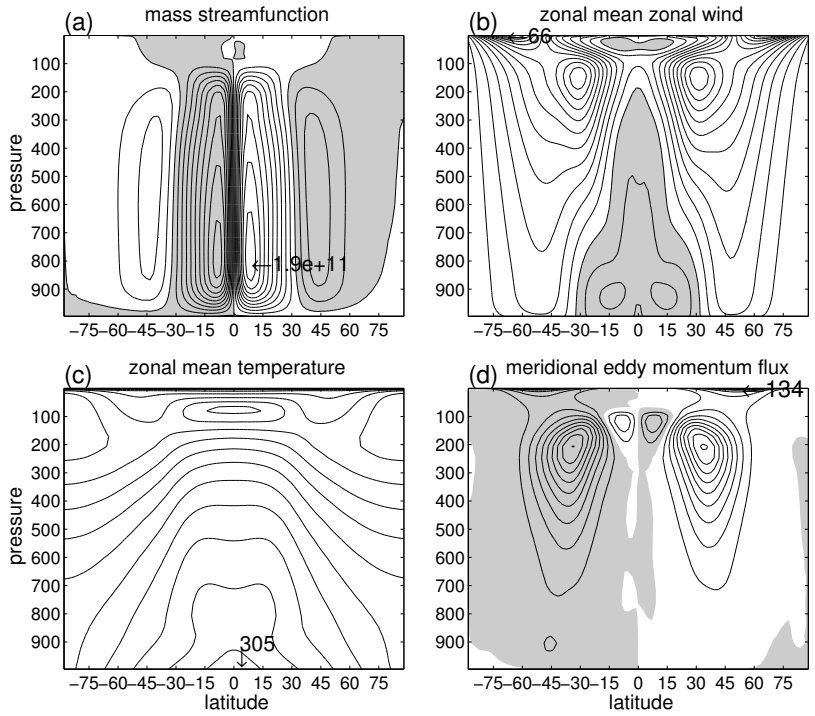


Figure 6.12: Time mean fields for the $S_0 = 1550$ W/m^2 aquaplanet atmosphere. (a) Zonal mean mass stream function, contour interval $2x10^{10}$ kg s^{-1}. (b) Zonal mean zonal winds, contour interval 5 m/s. (c) Zonal mean temperature, contour interval 10 K. (d) $[\overline{u'v'}]\cos\phi$, contour interval 10 m^2/s^2. Shaded areas negative valued. Largest values highlighted.

shutdown of extratropical variability. The superrotation and dominance of tropical eddies in Fig. 6.13 is very similar to the extreme hothouse climate simulation (equatorial surface temperature of 47 °C) of Fig. 2b in Caballero and Huber (2010). CH10 highlighted the large difference between their preindustrial control and extreme hothouse simulations. Similar to the simulations discussed here CH10 stated that the hothouse climate had a nearly entirely different general circulation from that of their pre-industrial control, with extratropical eddy activity almost entirely overshadowed by tropical eddies.

The relative humidity climatologies of the control and $S_0 = 1600$ W/m^2 atmospheres are shown in Fig. 6.14. The control atmosphere relative humidity is quite structured with the sharply defined tropopause dividing the somewhat moist upper troposphere from the dry stratosphere. In the control's tropics there is a large maximum in relative humidity between

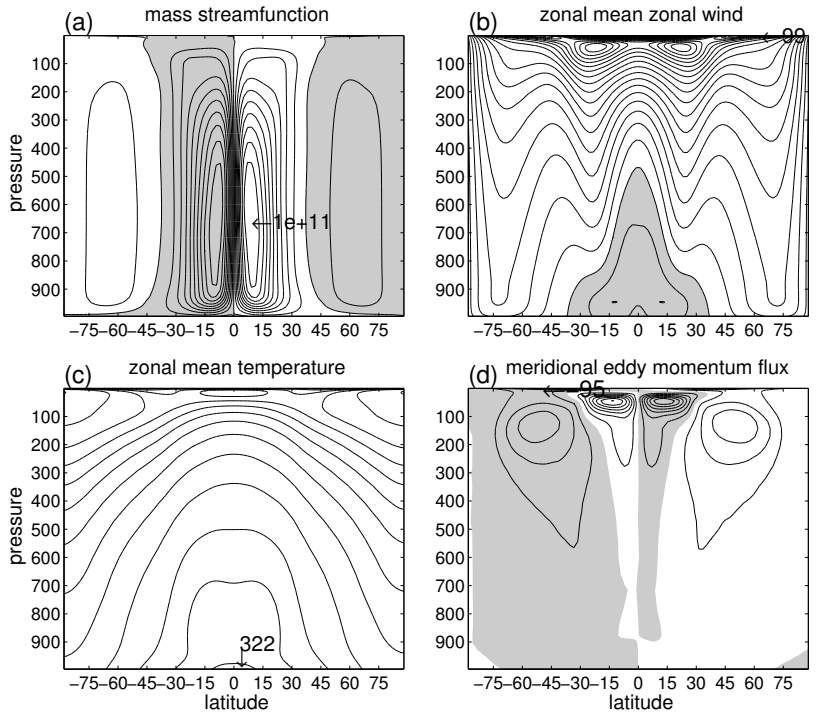


Figure 6.13: Time mean fields for the $S_0 = 1600$ W/m^2 aquaplanet atmosphere. (a) Zonal mean mass stream function, contour interval $2x10^{10}$ kg s^{-1}. (b) Zonal mean zonal winds, contour interval 5 m/s. (c) Zonal mean temperature, contour interval 10 K. (d) $[\overline{u'v'}]\cos\phi$, contour interval 10 m^2/s^2. Shaded areas negative valued. Largest values highlighted.

100 and 250 mb, where the Hadley cell outflows. The Hadley cell subsidence region, between 7.5° and 30° and 300 to 800 mb, has low relative humidities, dropping below 30%. The $S_0 = 1600$ W/m^2 atmosphere's relative humidity has a more complicated structure. There is high relative humidity throughout the entirety of the equatorial atmosphere. The narrow region of high relative humidity near 50% at the equator and 50 mb (the top of the Hadley cell), seemingly corresponds to the high altitude eddy activity in Fig. 6.13d, and we return to this point in Section 6.6.2.

6.6.1 Hothouse tropical variability

Fig. 6.15 shows the horizontal structure of the $S_0 = 1600$ W/m^2 hothouse atmosphere's dominant mode. The figure shows equatorial zonal wind at 44 mb filtered for wavenumber

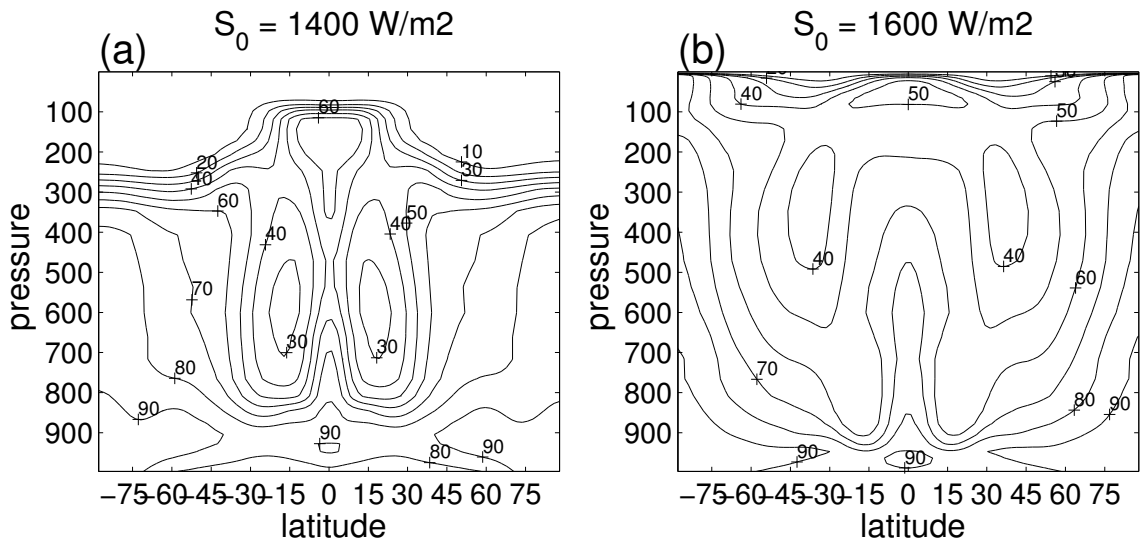


Figure 6.14: Relative humidity in the (a) $S_0 = 1400$ W/m^2 and (b) $S_0 = 1600$ W/m^2 atmospheres.

1 and frequencies between 0 and 0.22 1/day regressed onto geopotential height, horizontal wind, and total precipitation. The mode stretches to nearly 45°, dominating the bulk of the atmosphere. The mode is wavenumber one with a set each of cyclonic and anticyclonic gyres sitting off the equator. The wind anomaly peaks at the equator while the geopotential height anomaly peaks near 25°. The positive precipitation anomaly is associated with a region of divergence, and the negative anomaly with a region of convergence. The two-gyre structure closely coupled to precipitation suggests that this mode is the model's MJO (e.g. Zhang, 2005; Kiladis et al., 2009). The structure of the dominant tropical modes in the $S_0 = 1400$ W/m^2 through $S_0 = 1575$ W/m^2 atmospheres are very similar to Fig. 6.15, with a clear two-gyre structure associated with equatorial precipitation. The primary difference between the colder atmosphere MJO's is the meridional width: the colder atmospheres have narrower equatorial deformation radii (not shown).

A summary of the warmer atmospheres' tropical variability is shown in Fig. 6.16. The $S_0 = 1550$ W/m^2 atmosphere has $\mathcal{S}$ structure similar to the control, Fig. 6.2b. The dominant component is the model's MJO at wavenumber-1, with a significant contribution from

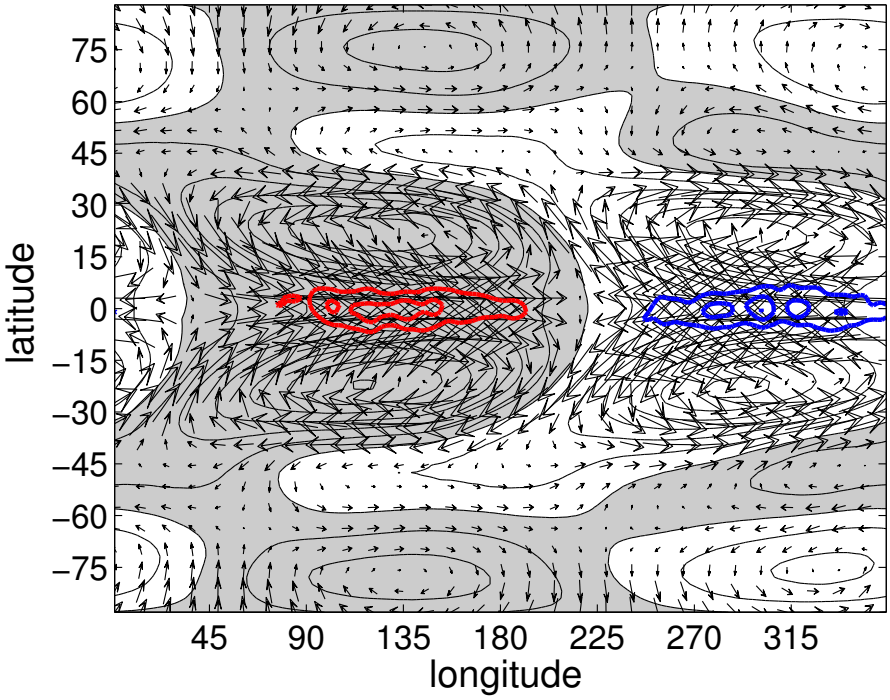


Figure 6.15: Wavenumber-1 and 0-0.22 1/day frequency filtered equatorial 44 mb zonal wind variability regressed onto global fields at 44 mb. Arrows show horizontal wind, maximum wind vector 7.7 m/s. Contours show geopotential height with contour interval 20 m, shaded regions negative. Shaded contours show precipitation at ± 5 and 10 mm/day.

higher wavenumber Kelvin waves. There is a small acceleration due to wavenumber 1 and 2 equatorial Rossby waves. As the heating continues the acceleration is entirely dominated by eastward eddies, with the higher wavenumber Kelvin waves almost entirely disappearing in the $S_0 = 1600$ W/m^2 atmosphere. There is a definite trend in the slope of the MJO/Kelvin wave signal: as the atmosphere warms, the Kelvin waves become faster (dispersion curve steepens). This is likely due to an increase in equivalent depth due to an increase in stratification and the increase in atmospheric scale height, though it may also be a result of stronger upper level winds Doppler-shifting the tropical modes eastward. While there are dramatic differences between the $S_0 = 1400$ W/m^2, $S_0 = 1550$ W/m^2, and $S_0 = 1600$ W/m^2 atmospheres, the primary difference – from the perspective of tropical variability – is simply a strengthening of the preexisting model MJO. The superrotation of the hothouse moist model has a fundamental distinction from that of the large R_o or Williams 2003 atmospheres

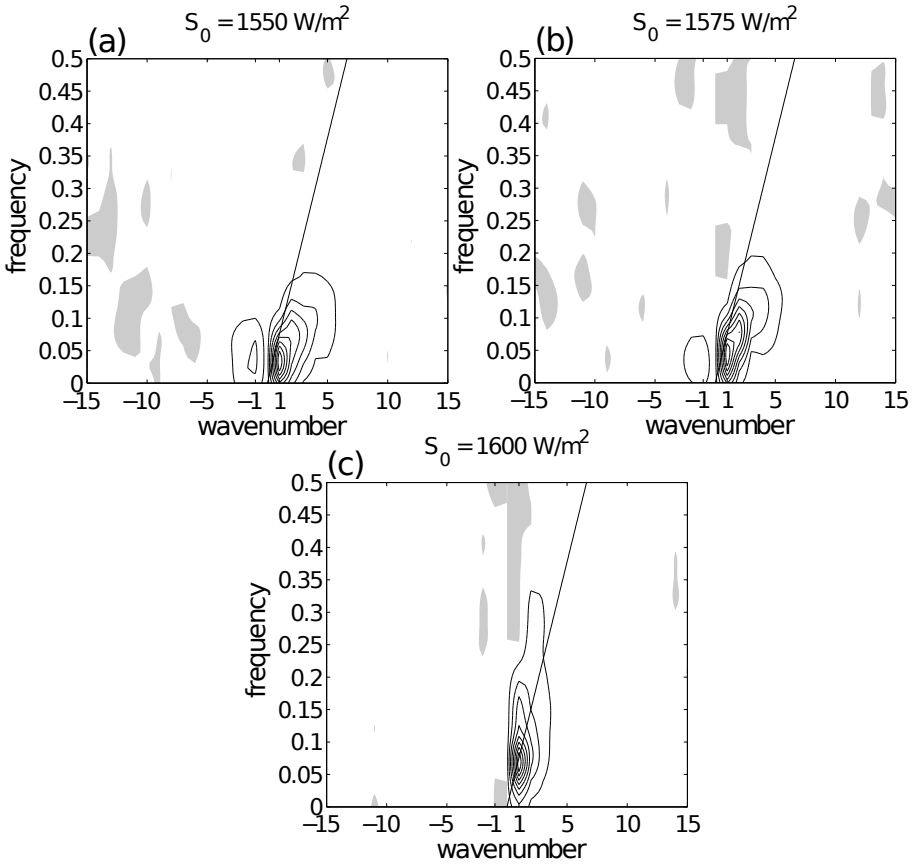


Figure 6.16: $\mathcal{S}$ for several hot atmospheres. (a) $S_0 = 1550$ W/m^2 at 118 mb, acceleration 4.4 m/s/day. (b) $S_0 = 1575$ W/m^2 at 98 mb, acceleration 5.7 m/s/day. (c) $S_0 = 1600$ W/m^2 at 44 mb, acceleration 7.5 m/s/day. Contour intervals arbitrary, shaded regions negative. The solid lines shows the theoretical dispersion relation for a Kelvin wave with an equivalent depth of 40 m.

discussed in Ch. 2. In the dry dynamical core entirely new dynamics emerged as the radius was decreased; in the control dry model there was negligible tropical variability while the small radius atmospheres had extremely strong global Kelvin-Rossby modes that directly led to superrotation. In the hothouse runs discussed here pre-existing dynamics – the MJO – need only be amplified to create superrotation.

6.6.2 Changes in model physics

We have shown that the superrotation in our hothouse simulations are due to an amplification of the model's MJO. In this section we attempt to understand why the MJO is amplified in the hothouse $S_0 = 1600$ W/m^2 atmosphere.

The precipitation as a function of solar constant in Fig. 6.11 shows a sharp drop off in precipitation generated by the convective cloud scheme between $S_0 = 1550$ W/m^2 and $S_0 = 1600$ W/m^2. This drop off is for the most part made up for by a large increase in precipitation generated by the stratiform cloud parameterization. The AGCM outputs several cloud parameterization-specific fields that give some insight into this switchover between convective and stratiform precipitation.

Fig. 6.17 shows vertical profiles of equatorial convective mass flux for various solar constants. The control atmosphere convective mass flux peaks near 900 mb at a magnitude of 0.025 kg/m^2/day and decreases to zero at 200 mb. At $S_0 = 1550$ W/m^2 the mass flux peaks near 950 mb at only 0.016 kg/m^2/day, but reaches 100 mb before disappearing and reaches higher values than the control above 400 mb. The $S_0 = 1600$ W/m^2 atmosphere continues the trend of weakening, with the convective mass flux peaking near 950 mb at roughly 0.007 kg/m^2/day and slowly decreasing to zero just above 100 mb. The trend is clear: as the atmosphere warms the model's convection scheme weakens dramatically.

As the atmosphere warms and the convection scheme weakens the stratiform scheme cloud scheme becomes dominant, as shown in Figs. 6.18 and 6.19. Fig. 6.18 plots the equatorial vertical profiles of the temperature change induced by the convection scheme (Fig. 6.18a) and the stratiform scheme (Fig. 6.18b). In the control atmosphere convection cools the surface while heating peaks near 850 mb at 5 K/day. The control convective heating is negligible above 200 mb. Despite having a weaker mass flux, the $S_0 = 1550$ W/m^2 atmosphere has much more convective heating, particularly in the mid to upper troposphere. Again, the $S_0 = 1600$ W/m^2 atmosphere's convection scheme has a smaller impact on the column,

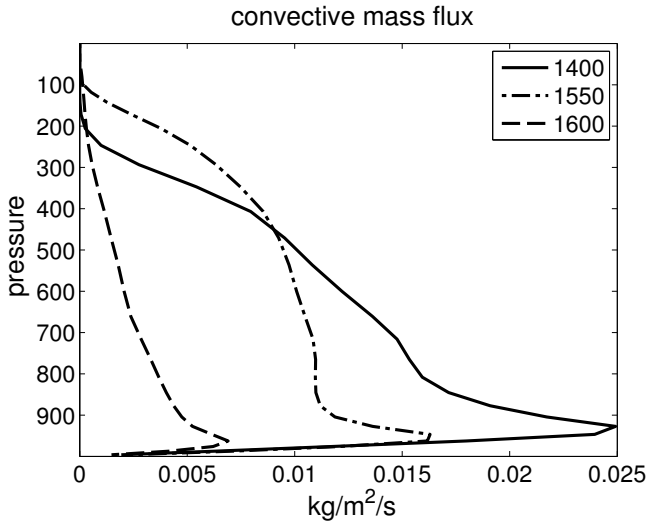


Figure 6.17: Vertical profiles of equatorial convective mass flux for the $S_0 = 1400$ W/m^2 (solid), $S_0 = 1550$ W/m^2 (dash-dotted), and $S_0 = 1600$ W/m^2 (dashed) atmospheres.

with heating peaking of 2.5 K/day near 975 mb. Despite being weaker, the $S_0 = 1600$ W/m^2 atmosphere's convective heating is nonzero up to 40 mb, significantly higher than the control. In the control atmosphere the stratiform scheme heating follows the canonical dipole stratiform column heating profile (Fig. 3c Houze Jr, 1997), with cooling ($\sim$ -1 K/day) in the lower half of the atmosphere and weak heating ($\sim$ 0.25 K/day) between 150-500 mb. Stratiform heating is somewhat stronger in the $S_0 = 1550$ W/m^2 atmosphere, with heating rates peaking at 2 K/day at 300 mb. The $S_0 = 1600$ W/m^2 atmosphere's stratiform heating profile is again entirely different, with heating peaking at 6.5 K/day between 100-300 mb. The cooling is now below 800 mb peaking at -2 K/day at the surface. In the $S_0 = 1600$ W/m^2 atmosphere stratiform heating has almost entirely replaced the convective heating. This stratiform heating is significantly higher than that of the convective heating in the control.

The changes in profiles of equatorial moistening also shows clear trends, Fig. 6.19. In the control and $S_0 = 1550$ W/m^2 atmospheres convection strongly dries below 900 mb, then more weakly dries the troposphere up to 100 mb. The $S_0 = 1600$ W/m^2 atmosphere's convection

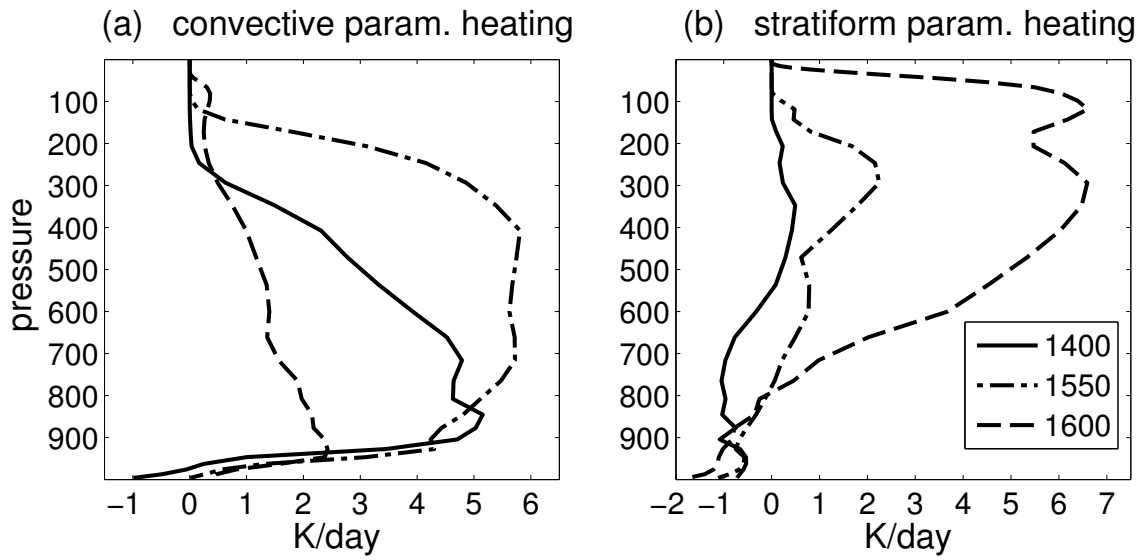


Figure 6.18: Vertical profiles of equatorial heating from (a) convective cloud parameterization and (b) stratiform cloud parameterization for the $S_0 = 1400$ W/m^2 (solid), $S_0 = 1550$ W/m^2 (dash-dotted), and $S_0 = 1600$ W/m^2 (dashed) atmospheres.

scheme dries the lowermost 200 mb but also moistens between 100 and 550 mb. In the control atmosphere the stratiform scheme weakly (~ 0.3 g/kg/day) moistens the atmosphere up to 550 mb. The $S_0 = 1550$ W/m^2 atmosphere moistens below 750 mb and dries above. In the $S_0 = 1600$ W/m^2 atmosphere changes in specific humidity by the stratiform scheme mirror that of the stratiform heating in Fig. 6.18b, with strong drying in the upper atmosphere corresponding to strong latent heating.

6.7 Discussion and conclusions

In this chapter we have looked at several problems involving tropical variability and superrotation using a full physics AGCM. In the first sections we showed that the results of previous chapters that used the idealized dry dynamical core with Held-Suarez physics still held when a model with moisture, radiation and boundary layer physics was used. The atmosphere with extreme seasonality had strong equatorial Rossby wave activity rather than MJO activity, very similar to the dry model. The $a = 9e5$ m moist atmosphere, while somewhat different

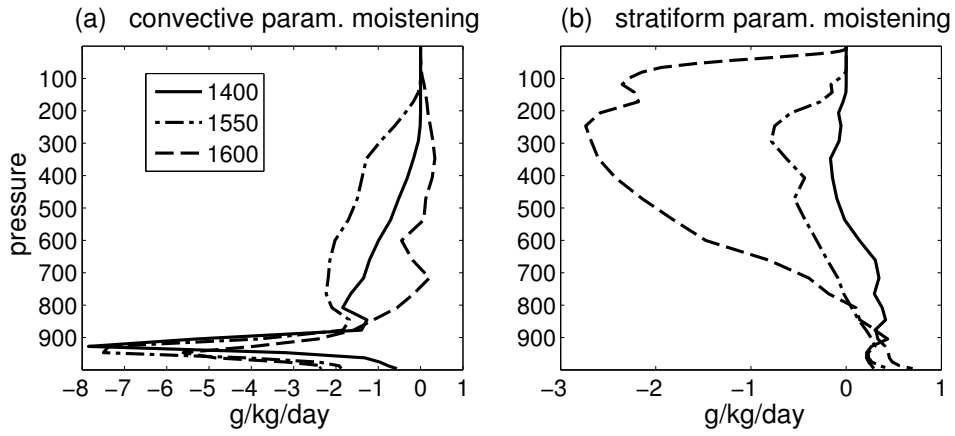


Figure 6.19: Vertical profiles of equatorial moistening from (a) convective cloud parameterization and (b) stratiform cloud parameterization for the $S_0 = 1400$ W/m^2 (solid), $S_0 = 1550$ W/m^2 (dash-dotted), and $S_0 = 1600$ W/m^2 (dashed) atmospheres.

from its dry counterpart, also strongly superrotated due to Kelvin waves fluxing momentum towards the equator. In the final section we looked at superrotation and tropical variability in extreme hothouse integrations of the model, and found that, similar to previous studies, very hot atmospheres have a tendency to superrotate. This transition to superrotation was the result of an intensification of the model's MJO, and we showed that this intensification was directly linked to a switchover from the convective cloud scheme to the stratiform cloud scheme in the deep tropics.

One interesting conclusion from this chapter is the fundamental difference between the superrotation in the $a = 9e5$ m and $S_0 = 1600$ W/m^2 atmospheres. The superrotation in the small radius atmosphere appears to be, just as in the dry model, due to a Kelvin wave that is strongly linked to the extratropics. The hothouse superrotation, on the other hand, is due to an amplification of the moist model's MJO, a dynamical mode that could not exist in a dry model.

Studies have shown that IPCC models including CM2.1, the coupled GFDL model that uses AM2.1 as its atmosphere, have difficulty simulating tropical intraseasonal variability (Lin et al., 2006). In addition to poorly simulating the Matsuno family of equatorial waves,

the models also do a poor job of simulating the MJO (see Lin et al. (2006) Fig. 6d). It is possible that part of the reason CM2.1 does a poor job simulating the MJO is its inability to correctly partition between convective and stratiform tropical precipitation. Dai (2006) showed that CM2.1's tropical convective fraction (the fraction of precipitation at a given grid point attributable to convection) was 95%, significantly higher than the convective fraction of 45-65% found in the Tropical Rainfall Measuring Mission (TRMM). Lin et al. (2004) showed that the latent heating that results from stratiform precipitation is an essential component of the MJO. Lin et al. (2004) argued that GCMs' inability to simulate sufficient stratiform precipitation on intraseasonal timescales was, in part, to blame for their inability to model the MJO. The authors showed that at the time of peak precipitation the MJO had a convective fraction of only 40% and that the resultant stratiform precipitation influenced heating profile was top heavy. Idealized tropical instability studies have shown that top heavy vertical heating profiles are most likely to generate tropical modes (e.g. Cho and Pendlebury, 1997; Mapes, 2000; Straub and Kiladis, 2003b; Kuang, 2008). In our AM2.1 model runs the convective fractions of the control and the $S_0 = 1600$ W/m^2 atmosphere were 95% and 25%, respectively. We therefore hypothesize that the transition from convective (with a heating profile maximal in the mid-troposphere) to stratiform (with heating profile maximal in the upper atmosphere) precipitation in the $S_0 = 1600$ W/m^2 atmosphere is directly responsible for super charging the model's MJO and, consequently, generating superrotation.

Our work suggests one of two differing conclusions. First, it is possible that the transition to the large-scale stratiform cloud scheme's dominance is physical, and the model is acting like a hothouse atmosphere would. Perhaps at high enough temperatures clouds and precipitation are better modeled using the stratiform scheme. It is difficult, however, to believe the transition in precipitation type is accurate when the mean state convective fraction is itself far from Earth-like. Another possibility is that the trend in heating profiles, with the maximum moving from the mid troposphere to the upper troposphere, is accurate despite any issues

with partitioning between precipitation types. Second, our results may suggest that climate models with conventional cloud schemes are not capable of modeling hothouse climates. It is possible that at such extreme temperatures the atmosphere is better modeled using next-generation cloud physics, such as superparameterization schemes (e.g. Arnold, 2014), and that the exotic results seen here and in CH10 are a modeling artifact.

Chapter 7

Conclusion

This thesis has centered around characterizing tropical variability, attempting to understand how tropical waves are triggered, and investigating the impacts of extratropical Rossby waves on the tropics in a variety of idealized atmospheric general circulation models.

In Chapter 2 we explored the parameter space of the Held-Suarez forced GFDL dry dynamical core to find superrotating atmospheric states. We varied four fundamental parameters of the dynamical core, the thermal Rossby number ($R_o = R\Delta_h/(2\Omega a)^2$), the Ekman number ($E = r/(2\Omega)$), the nondimensional radiative timescale ($\tau = 2\Omega\tau_r$), and the nondimensional vertical temperature gradient ($\mu = \Delta_v/\Delta_h$). While modifying τ and E can generate strong equatorial easterlies, superrotation is only found at large R_o. As R_o is increased the dynamical core's tropics become dominated by Kelvin waves. These Kelvin waves flux momentum equatorwards and are directly responsible for the large R_o superrotation.

We also found that Kelvin wave momentum transport is also vital to the superrotation in Williams (2003), where the storm tracks were made to collapse towards the equator. In the large R_o superrotation we determined that extratropical Rossby waves are a crucial component for the excitation of equatorial Kelvin waves. In Earth's atmosphere the Madden-Julian Oscillation dominates the tropical eddy momentum transport. However, we found

that near the outflow level of the Hadley cell Kelvin wave momentum transport is of equal importance to that of the MJO.

In Chapter 3 we studied the meridional propagation of extratropical Rossby waves using the linearized barotropic vorticity equation. We found that the WKB approximation is very good at approximating the Rossby wave's meridional propagation, but that it fails in several key instances. We found that significant Rossby wave energy can tunnel through evanescent regions ($\ell < 0$) and, at one extreme, a jump zonal wind profile is capable of transmitting the entirety of a wave despite the meridional wavenumber ℓ passing through zero. At the other end, we showed that relatively gentle zonal wind profiles where the WKB approximation is applicable can generate significant reflection.

Using our model we explored reflection and transmission of extratropical Rossby waves through the East Pacific Window. We found that the climatological boreal winter and boreal spring East Pacific winds are quite transparent to stationary waves, but that even minor changes in the zonal wind profiles can produce significant reflection.

In Chapter 4 we attempted to explain the large R_o superrotation explored in Chapter 2 using the key insight from Chapter 3 that Rossby waves retain significant wave energy while tunneling through evanescent regions. We laid out three necessary conditions for the excitation of equatorial Kelvin waves by extratropical Rossby waves: the matching of wavenumbers, the matching of frequencies, and a minimizing of evanescence between the region of Rossby wave generation and the tropical waveguide. Using output from the dynamical core we found an approximate dispersion relation for extratropical Rossby waves. Using the Rossby wave and the Kelvin wave dispersion relations we found matching conditions for where in wavenumber-frequency space the two waves have equal frequency and wavenumber. Lastly, we found conditions under which extratropical Rossby wave energy reaching the tropical waveguide was maximized. We argued that the large R_o and Williams 2003 atmospheres superrotate, in part, because Rossby wave evanescence is minimized.

Chapter 5 looked at tropical variability in a seasonally varying version of the dry dynamical core. It was shown that the seasonal mean flow decelerates the tropical atmosphere. This acceleration directly leads to tropical eddies that accelerate the mean flow. The eddies are a strong function of time-of-year: during more equinoctial conditions, Kelvin waves are prevalent but during solstitial conditions equatorial Rossby and easterly waves are dominant. The strongly seasonal atmosphere was also shown to have a mid-troposphere temperature minimum. The equatorial eddies responsible for eddy momentum transport were shown to transport heat equatorwards so as to balance equatorial cooling by the vertical component of the mean flow. We argued that the equatorial eddies were generated by barotropic instability that was the result of strong easterly shear generated by mean flow deceleration of the tropical zonal wind.

In Chapter 6 we investigated tropical variability in extreme global warming integrations of a full-physics aquaplanet atmospheric general circulation model. Similar to previous studies, we found that MJO-like tropical variability became preferred at hotter temperatures and that, with sufficient warming, the atmosphere superrotated. Unlike previous work we found that the warming-induced changes in the general circulation co-occurred with extreme changes in the model's physics parameterizations. Specifically, we showed that as the atmosphere warmed enough for sufficient superrotation the model's convective cloud scheme shut off and the 'large-scale' stratiform cloud scheme became dominant. Our results suggest that atmospheric models may not be capable of re-creating hothouse climates and that it is possible that present day climate models are fundamentally incapable of modeling extreme climates.

A second goal of Chapter 6 was to verify the results of Chs. 2, 4, and 5 to see if our results were significantly dependent on the use of a highly idealized dry dynamical core forced with Newtonian cooling. We showed that extreme seasonality in the moist model excited equatorial Rossby and easterly waves, similar to the dry model results of Ch. 5. We

also found that the small radius superrotation investigated in Chs. 2 and 4 was recreated in a small radius (large thermal Rossby number) run of the full-physics model. We found that a fundamental difference between the hothouse superrotation and the large thermal Rossby number superrotation is the type of equatorial mode that fluxes momentum equatorwards: Kelvin waves are responsible for the small radius superrotation in both the dry and moist models, while the model MJO (reliant on physics that do not exist in a dry model) drives superrotation in the hothouse.

Throughout the course of this thesis we have found that idealized atmospheric models have robust equatorial variability under the right forcings or planetary geometries. One take-away is that, like extratropical eddy or zonal mean tropical dynamics, interesting questions about tropical eddy dynamics can also be studied using idealized models. Studies have found that extratropical Rossby waves are a critical trigger of intraseasonal tropical variability in Earth's atmosphere (e.g. Liebmann and Hartmann, 1984; Lin et al., 2000; Straub and Kiladis, 2003a) and we have shown, along with more recent work such as Wang and Mitchell (2014), that idealized dry models have significant tropical-extratropical interaction leading to strong tropical wave activity. One unattained goal of this work was the study of extratropical initiation of equatorial waves in idealized models with Earth-like geometries. We hope that future work will build on this thesis to investigate, e.g., extratropical triggering of equatorial Kelvin waves in dry dynamical cores that may help to understand intreseasonal tropical variability without the (potentially) unnecessary complications of clouds, convection, and radiation.

One of the aims of this thesis was to clearly quantify the causes of superrotation in the large R_o, Williams 2003, and $S_0 = 1600$ W/m^2 atmospheres. To do this we started by identifying the tropical modes directly responsible for horizontal eddy momentum flux convergence $\mathcal{S}$ by looking at the structure of $\mathcal{S}$ in $\omega - k$ space. This diagnostic, directly analogous to the tropical wave diagnostics in the vein of Wheeler and Kiladis (1999), allowed for direct identification of modes responsible for tropical momentum fluxes. Once the modes were

identified we worked towards understanding how the modes might be excited. In the large R_o and Williams 2003 atmosphere we argued that the equatorial Kelvin waves were excited by extratropical Rossby waves. In the hothouse $S_0 = 1600$ W/m^2 atmosphere we argued that a possibly unphysical change in the model physics was responsible for the amplification of the MJO-like mode that drove superrotation. We hope that that this framework: (1) identification of the relevant tropical mode(s) using spectral diagnostics (2) physical explanation for the tropical mode's excitation, can help to provide a more comprehensive understanding of superrotation in atmospheric general circulation models.

Bibliography

Adames, Á. F., J. Patoux, and R. C. Foster, 2014: The contribution of extratropical waves to the MJO wind field. *J. Atm. Sci.*, **71 (1)**.

Adcroft, A., J.-M. Campin, C. Hill, and J. Marshall, 2004: Implementation of an atmosphere-ocean general circulation model on the expanded spherical cube. *Mon. Weather Rev.*, **132 (12)**, 2845–2863.

Arnold, N. P., 2014: Atmospheric superrotation in warm earth climates. URL `http://search.proquest.com/docview/1502868155?accountid=13314`, 145 pp.

Arnold, N. P., E. Tziperman, and B. Farrell, 2012: Abrupt transition to strong superrotation driven by equatorial wave resonance in an idealized GCM. *J. Atmos. Sci.*, **69**, 626–640.

Caballero, R. and M. Huber, 2010: Spontaneous transition to superrotation in warm climates simulated in CAM3. *Geophys. Res. Lett.*, **37**, 1–5.

Cho, H.-R. and D. Pendlebury, 1997: Wave cisk of equatorial waves and the vertical distribution of cumulus heating. *Journal of the atmospheric sciences*, **54 (20)**, 2429–2440.

Dai, A., 2006: Precipitation characteristics in eighteen coupled climate models. *Journal of Climate*, **19 (18)**, 4605–4630.

Delworth, T. L., et al., 2006: Gfdl's cm2 global coupled climate models. part i: Formulation and simulation characteristics. *Journal of Climate*, **19 (5)**, 643–674.

Edmon, H., Jr., B. Hoskins, and M. McIntyre, 1980: Eliassen-Palm cross sections for the troposphere. *J. Atm. Sci.*, **37 (12)**, 2600–2616.

Environmental Systems Science Center, Project Scientist G.J. Robinson, 2002-: Cloud Archive User Service (CLAUS). NCAS British Atmospheric Data Centre. Available from `http://badc.nerc.ac.uk/view/badc.nerc.ac.uk__ATOM__dataent_claus`, accessed July 2012.

Fels, S. B. and R. S. Lindzen, 1974: The interaction of thermally excited gravity waves with mean flows. *Geophys. Astro. Fluid*, **6 (2)**, 149–191.

Freidenreich, S. M. e. a., 2004: The new GFDL global atmosphere and land model AM2–LM2: Evaluation with prescribed SST simulations. *J. Climate*, **17**, 4641–4673.

Fyfe, J. and I. M. Held, 1990: The two-fifths and one-fifth rules for Rossby wave breaking in the WKB limit. *J. Atmos. Sci.*, **47**, 697–706.

Halevy, I. and R. Peltier, 1985: Barotropic instability and Rossby wave radiation. *J. Atmos. Sci.*, **42**, 1825–1837.

Hayashi, Y., 1982: Space-time spectral analysis and its application to atmospheric waves. *J. Meteor. Soc. Japan*, **60**, 156–171.

Hayashi, Y.-Y. and W. Young, 1987: Stable and unstable shear modes of rotating parallel flows in shallow water. *J. Fluid Mech.*, **184**, 477–504.

Held, I. M., 1985: Pseudomomentum and the orthogonality of modes in shear flows. *J. Atm. Sci.*, **42 (21)**, 2280–2288.

Held, I. M., 1999: Equatorial superrotation in earth-like atmospheric models. *Bernhard Haurwitz Memorial Lecture*, 1–24.

Held, I. M., 2000: The general circulation of the atmosphere. *WHOI GFD Lecture Notes*, 1–70.

Held, I. M. and A. H. Hou, 1980: Nonlinear axially symmetric circulations in a nearly inviscid atmosphere. *J. Atmos. Sci.*, **37**, 515–533.

Held, I. M. and M. J. Suarez, 1994: A proposal for the intercomparison of the dynamical cores of atmospheric general circulation models. *BAMS*, **75**, 1825–1830.

Hendon, H. H. and M. C. Wheeler, 2008: Some space-time spectral analyses of tropical convection and planetary-scale waves. *J. Atmos. Sci.*, **65**, 2936–2948.

Heng, K., K. Menou, and P. J. Phillipps, 2011: Atmospheric circulation of tidally locked exoplanets: a suite of benchmark tests for dynamical solvers. *Mon. Not. R. Astron. Soc.*, **413 (4)**, 2380–2402.

Hide, R., 1969: Dynamics of the atmospheres of the major planets with an appendix on the viscous boundary layer at the rigid bounding surface of an electrically-conducting rotating fluid in the presence of a magnetic field. *J. Atmos. Sci.*, **26**, 841–853.

Holton, J. R. and C. Mass, 1976: Stratospheric vacillation cycles. *J. Atmos. Sci.*, **33**, 2218–2225.

Hoskins, B. and D. Karoly, 1981: The steady linear response of a spherical atmosphere to thermal and orographic forcing. *J. Atmos. Sci.*, **38**, 1179–1196.

Hoskins, B. J. and T. Ambrizzi, 1993: Rossby wave propagation on a realistic longitudinally varying flow. *J. Atmos. Sci*, **50**, 1661–1671.

Hoskins, B. J. and G.-Y. Yang, 2000: The equatorial response to higher-latitude forcing. *J. Atmos. Sci.*, **57**, 1197–1213.

Houze Jr, R. A., 1997: Stratiform precipitation in regions of convection: A meteorological paradox? *Bulletin of the American Meteorological Society*, **78 (10)**, 2179–2196.

Huang, H.-P., K. M. Weickmann, and C. J. Hsu, 2001: Trend in atmospheric angular momentum in a transient climate change simulation with greenhouse gas and aerosol forcing. *J. Climate*, **14 (7)**, 1525–1534.

Iga, S.-I. and Y. Matsuda, 2005: Shear instability in a shallow water model with implications for the Venus atmosphere. *J. Atm. Sci*, **63**, 2514–2527.

Imamura, T., 2006: The meridional propagation of planetary-scale waves in vertical shear: Implication for the Venus atmosphere. *J. Atmos. Sci.*, **63**, 1623–1636.

Imamura, T., T. Horinouchi, and T. J. Dunkerton, 2004: The lateral transport of zonal momentum due to Kelvin waves in a meridional circulation. *J. Atmos. Sci.*, **61**, 1966–1975.

J. M. Wallace, 2012: ATM 545 Class Notes. Available from `http://www.atmos.washington.edu/academics/classes/2012Q2/545/`, accessed July 2011.

Jakob, C. and S. A. Klein, 2000: A parametrization of the effects of cloud and precipitation overlap for use in general-circulation models. *Q. J. Roy. Meteor. Soc.*, **126 (568)**, 2525–2544.

Joshi, M., R. Haberle, and R. Reynolds, 1997: Simulations of the atmospheres of synchronously rotating terrestrial planets orbiting M dwarfs: conditions for atmospheric collapse and the implications for habitability. *Icarus*, **129 (2)**, 450–465.

Karoly, D. J. and B. J. Hoskins, 1982: Three dimensional propagation of planetary waves. *J. Meteor. Soc. Japan*, **60**, 109–123.

Kasahara, A., 1980: Effect of zonal flows on the free oscillations of a barotropic atmosphere. *J. Atm. Sci*, **37**, 917–929.

Kay, I. and H. Moses, 1956: Reflectionless transmission through dielectrics and scattering potentials. *J. Appl. Phys.*, **27**, 1503–1508.

Kiladis, G. N., K. H. Straub, and P. T. Haertel, 2005: Zonal and vertical structure of the madden-julian oscillation. *Journal of the Atmospheric Sciences*, **62 (8)**, 2790–2809.

Kiladis, G. N., C. D. Thorncroft, and N. M. Hall, 2006: Three-dimensional structure and dynamics of African easterly waves. part I: Observations. *J. Atm. Sci.*, **63 (9)**.

Kiladis, G. N., M. C. Wheeler, P. T. Haertel, K. H. Straub, and P. E. Roundy, 2009: Convectively coupled equatorial waves. *Rev. Geophys.*, **47**.

Kraucunas, I. and D. L. Hartmann, 2005: Equatorial superrotation and the factors controlling the zonal-mean zonal winds in the tropical upper troposphere. *J. Atmos. Sci.*, **62**, 371–389.

Kuang, Z., 2008: A moisture-stratiform instability for convectively coupled waves. *Journal of the Atmospheric Sciences*, **65 (3)**, 834–854.

Lee, S., 1999: Why are the climatological zonal winds easterly in the equatorial upper troposphere? *J. Atmos. Sci.*, **56**, 1353–1363.

Lee, S. and I. M. Held, 1993: Baroclinic wave packets in models and observations. *J. Atm. Sci.*, **50 (10)**, 1413–1428.

Lian, Y. and A. P. Showman, 2010: Generation of equatorial jets by large-scale latent heating on the giant planets. *Icarus*, **207 (1)**, 373–393.

Liebmann, B. and D. L. Hartmann, 1984: An observational study of tropical-midlatitude interaction on intraseasonal time scales during winter. *J. Atm. Sci*, **41**, 3333–3350.

Lin, J., B. Mapes, M. Zhang, and M. Newman, 2004: Stratiform precipitation, vertical heating profiles, and the madden-julian oscillation. *Journal of the Atmospheric Sciences*, **61 (3)**, 296–309.

Lin, J.-L., et al., 2006: Tropical intraseasonal variability in 14 ipcc ar4 climate models. part i: Convective signals. *Journal of climate*, **19 (12)**, 2665–2690.

Lin, J. W.-B., J. D. Neelin, and N. Zeng, 2000: Maintenance of tropical intraseasonal variability: Impact of evaporation-wind feedback and midlatitude storms. *J. Atm. Sci*, **57**, 2793–2823.

Lindzen, R. and K. Tung, 1978: Wave overreflection and shear instability. *J. Atmos. Sci.*, **35**, 1626–1632.

Liu, J. and T. Schneider, 2011: Convective generation of equatorial superrotation in planetary atmospheres. *J. Atm. Sci.*, **68 (11)**, 2742–2756.

Magnusdottir, G. and C.-C. Wang, 2008: Intertropical convergence zones during the active season in daily data. *J. Atm. Sci.*, **65 (7)**.

Mapes, B. E., 2000: Convective inhibition, subgrid-scale triggering energy, and stratiform instability in a toy tropical wave model. *Journal of the Atmospheric Sciences*, **57 (10)**, 1515–1535.

Matsuno, T., 1966: Quasi-geostrophic motions in the equatorial area. *J. Meteor. Soc. Japan*, **44**, 25–43.

Merlis, T. M. and T. Schneider, 2010: Atmospheric dynamics of earth-like tidally locked aquaplanets. *J. Adv. Mod. Earth Sys.*, **2 (12)**.

Mitchell, J. L. and G. K. Vallis, 2010: The transition to superrotation in terrestrial atmospheres. *J. Geophys. Res.*, **115**, 1–17.

Mitchell, J. L., G. K. Vallis, and S. F. Potter, 2014: Effects of the seasonal cycle on superrotation in planetary atmospheres. *ApJ*, **787 (1)**, 23.

Moorthi, S. and M. J. Suarez, 1992: Relaxed arakawa-schubert. a parameterization of moist convection for general circulation models. *Mon. Weather Rev.*, **120 (6)**, 978–1002.

Pinto, J. R. D. and J. L. Mitchell, 2014: Atmospheric superrotation in an idealized GCM: Parameter dependence of the eddy response. *Icarus*, **238 (0)**, 93 – 109.

Potter, S. F., T. Spengler, and I. M. Held, 2013: Reflection of barotropic rossby waves in sheared flow and validity of the wkb approximation. *Journal of the Atmospheric Sciences*, **70 (7)**, 2170–2178.

Potter, S. F., G. K. Vallis, and J. L. Mitchell, 2014: Spontaneous superrotation and the role of Kelvin waves in an idealized dry GCM. *J. Atm. Sci.*, **71**, 596–614.

Pratt, R. W., 1977: Space-time kinetic energy spectra in mid-latitudes. *J. Atm. Sci.*, **34 (7)**, 1054–1057.

Randel, W. J. and I. M. Held, 1991: Phase speed spectra of transient eddy fluxes and critical layer absorption. *J. Atmos. Sci.*, **48**, 688–697.

Rauscher, E. and K. Menou, 2012: A general circulation model for gaseous exoplanets with double-gray radiative transfer. *ApJ*, **750 (2)**, 96.

Rotstayn, L. D., 1997: A physically based scheme for the treatment of stratiform clouds and precipitation in large-scale models. i: Description and evaluation of the microphysical processes. *Quarterly Journal of the Royal Meteorological Society*, **123 (541)**, 1227–1282.

Rotstayn, L. D., B. F. Ryan, and J. J. Katzfey, 2000: A scheme for calculation of the liquid fraction in mixed-phase stratiform clouds in large-scale models. *Monthly weather review*, **128 (4)**, 1070–1088.

Saravanan, R., 1993: Equatorial superrotation and maintenance of the general circulation in two-level models. *J. Atmos. Sci.*, **50**, 1211–1227.

Schneider, T., 2006: The general circulation of the atmosphere. *Annu. Rev. Earth Planet. Sci.*, **34**, 655–688.

Schneider, T. and S. Bordoni, 2008: Eddy-mediated regime transitions in the seasonal cycle of a Hadley circulation and implications for monsoon dynamics. *J. Atm. Sci.*, **65 (3)**.

Showman, A. P., J. J. Fortney, Y. Lian, M. S. Marley, R. S. Freedman, H. A. Knutson, and D. Charbonneau, 2009: Atmospheric circulation of hot Jupiters: Coupled radiative-dynamical general circulation model simulations of HD 189733b and HD 209458b. *ApJ*, **699 (1)**, 564.

Showman, A. P. and L. M. Polvani, 2010: The Matsuno-Gill model and equatorial superrotation. *Geo. Res. Lett.*, **37**, 1–5.

Showman, A. P. and L. M. Polvani, 2011: Equatorial superrotation on tidally locked exoplanets. *ApJ*, **738**, 1–24.

Sobel, A. H., J. Nilsson, and L. M. Polvani, 2001: The weak temperature gradient approximation and balanced tropical moisture waves. *J. Atm. Sci*, **58**, 3650–3665.

Straub, K. H. and G. N. Kiladis, 2003a: Extratropical forcing of convectively coupled Kelvin waves during austral winter. *J. Atm. Sci*, **60**, 526–543.

Straub, K. H. and G. N. Kiladis, 2003b: The observed structure of convectively coupled kelvin waves: Comparison with simple models of coupled wave instability. *Journal of the atmospheric sciences*, **60 (14)**, 1655–1668.

Suarez, M. J. and D. G. Duffy, 1992: Terrestrial superrotation: A bifurcation of the general circulation. *J. Atmos. Sci.*, **49**, 1541–1554.

Tulich, S. N., G. N. Kiladis, and A. Suzuki-Parker, 2011: Convectively coupled Kelvin and easterly waves in a regional climate simulation of the tropics. *Clim. Dynam.*, **36 (1-2)**, 185–203.

Vallis, G. K., 2006: *Atmospheric and Oceanic Fluid Dynamics*. Cambridge University Press, 745 pp.

Wang, P. and J. L. Mitchell, 2014: Planetary ageostrophic instability leads to superrotation. *Geo. Res. Let.*.

Webster, P. J. and J. R. Holton, 1982: Cross equatorial response to middle-latitude forcing in a zonally varying basic state. *J. Atmos. Sci*, **39**, 722–733.

Wheeler, M. and G. N. Kiladis, 1999: Convectively coupled equatorial waves: Analysis of clouds and temperature in the wavenumber-frequency domain. *J. Atmos. Sci.*, **56**, 374–399.

Williams, G., 2003: Barotropic instability and equatorial superrotation. *J. Atmos. Sci.*, **60**, 2136–2152.

Yeh, K. and C. Liu, 1972: *Theory of Ionospheric Waves*. Academic Press, 464 pp.

Zhang, C., 1993: Laterally forced equatorial perturbations in a linear model. part II: Mobile forcing. *J. Atm. Sci*, **50**, 807–821.

Zhang, C., 2005: Madden-Julian oscillation. *Rev. Geophys.*, **43**, 1–36.

Zhang, C. and P. J. Webster, 1992: Laterally forced equatorial perturbations in a linear model. part I: Stationary transient forcing. *J. Atm. Sci*, **49**, 585–607.

Zhu, X., 2006: Maintenance of equatorial superrotation in the atmospheres of venus and titan. *Planet Space Sci.*, **54 (8)**, 761–773.